4650R

SPACE SCIENCE AND ENGINEERING CENTER

UNIVERSITY of WISCONSIN – MADISON
1225 West Dayton Street
Madison, Wisconsin 53706-1695

20 May 1996

Joseph S. Murray
Grants Officer
NASA Langley Research Center
Code 126:J.S.Murray
Hampton, VA 23681-0001

THE SCHWERDTFEGER LIBRARY
1225 W. Dayton Street
Madison, WI 53706

Re: NAG1-1177 Final Report

Dear Mr. Murray:

Enclosed please find one copy of the Final Report entitled "Participation in the FIRE Phase II Program" for the period 1 September 1990 through 30 April 1995.

We apologize for the tardiness of this report. If you have any questions, please call Steve Ackerman at 608-263-3647.

Thank you for your cooperation.

Sincerely,

John P. Roberts
Assistant Director

Enc: (1)

cc: 144BW58
S. Ackerman
4650

k:\admin\4650rpt.doc

Executive Director (608) 262-0544 Human Resources (608) 263-2348 Fax (608) 262-5974
Business Services (608) 263-3037 General Information (608) 263-6750 Telex 265452 UOFWISC MDS

Final Technical Report for NASA grant NAG1-1177

Participation in the FIRE Phase II Program

The focus of this research was to employ observations of the High-resolution Interferometer Sounder (HIS) made during the second First ISCCP Regional Experiment (FIRE II) to improve our understanding of the radiative properties of cirrus. Studies were undertaken to investigate the coupling between the microphysical properties of cirrus clouds and their spectral variation within the infrared region and the capability to infer the macrophysical and microphysical properties of cirrus clouds using high spectral resolution measurements. The were two phases to this grant, Deployment and Field Observations Phase and the Data Analysis Phase.

DEPLOYMENT AND FIELD OBSERVATIONS PHASE

The deployment/field operations phase of FIRE II covered the period September 1, 1991 through August 31, 1992, and included activities necessary to get the High-resolution Interferometer Sounder (HIS) operational for an aircraft environment. This phase also included the active participation of HIS field scientists in the flight planning operations of FIRE II which took place in November and December 1991.

DATA ANALYSIS PHASE

Analysis of data collected during the field experiment was included in the second phase of the grant. Specific research objectives included: 1) to improve our understanding of the relationship between the microphysical and radiative properties of cirrus clouds; 2) to quantify the capabilities and limitations of various cirrus cloud satellite retrieval techniques; and 3) to improve our capabilities of describing cirrus cloud properties utilizing passive radiometric observations. The results of the research sponsored by this grant are found in the four publications included in this report. In addition to these referred papers there were 11 papers presented at conferences. These are listed below.

Publications in Refereed Journals

Smith, W. L., H. E. Revercomb, R. O. Knuteson, F. A. Best, R. Dedecker, H. B. Howell, and H. M. Woolf, 1995: Cirrus cloud properties derived from high-spectral

resolution infrared spectrometry during FIRE II, Part I: The High Resolution Interferometer Sounder (HIS) systems. *Jour. Atmos Sci.* **52**, 4238-4245.

Ackerman, S. A., W. L. Smith, A. D. Collard, X. L. Ma, H. E. Revercomb and R. O. Knuteson, 1995: Cirrus cloud properties derived from high-spectral resolution infrared spectrometry during FIRE II, Part II: Aircraft HIS results *Jour. Atmos Sci.* **52**, 4246-4263.

Collard, A. D., Ackerman, S. A., W. L. Smith, X. L. Ma, H. E. Revercomb, R. O. Knuteson, and S. C. Lee, 1995: Cirrus cloud properties derived from high-spectral resolution infrared spectrometry during FIRE II, Part II: Groundbased results. *Jour. Atmos Sci.* **52**, 4264-4275.

Soden, B. J., S. A. Ackerman, A. Ferrera and D. O'C Starr, 1994: Comparison of upper troposheric water vapor from GOES, Raman lidar and CLASS measurements during FIRE Cirrus-II. *J. Geo. Res.* **99**, 21005-21016.

Conference Proceedings and Presentations

Ackerman, S. A., A. Collard, and W. L. Smith, 1994: Cloud properties from ground-based and high-altitude FTIR observations. Conference on Passive Infrared remote Sensing of Clouds and the Atmosphere II. Rome, Italy. Sept. 26-30.

Ackerman, T. P., J. A. Valero, S. Kinne, P. Pilewskie, G. P. J. Valero, S. A. Ackerman and M. Shiobara, 1994: A comparison of cirrus cloud optical depths determined from ground-based passive radiation measurements during FIRE cirrus II. AMS Eighth Conference on Atmospheric Radiation. Jan. 23-27, Opryland, TN.

W. L. Smith, S. A. Ackerman, X. L. Ma, R. O. Knuteson, and H. E. Revercomb, 1994: Cloud properties from FTIR observations. AMS Eighth Conference on Atmospheric Radiation. Jan. 23-27, Opryland, TN.

Soden, B. J. and S. A. Ackerman, 1994: Comparison of GOES, Lidar and CLASS sonde observations of upper tropospheric relative humidity. AMS Eighth Conference on Atmospheric Radiation. Jan. 23-27, Opryland, TN

W. L. Smith, S. A. Ackerman R. O. Knuteson, X. L. Ma, and H. E. Revercomb, 1993: Cooperative Institute for Meteorological Satellite Studies, CIMSS FIRE research activities. FIRE II cirrus Science Team Meeting, Breckenridge, CO

Soden, B. J. and S. A. Ackerman, 1993: Analysis of the GOES 6.7 μm channel observations. FIRE II cirrus Science Team Meeting, Breckenridge, CO

Ackerman, S. A. Ackerman, W. L. Smith, X. L. Ma and R. O. Knuteson and H. E. Revercomb, 1993: Cirrus cloud retrievals from HIS observations. FIRE II cirrus Science Team Meeting, Breckenridge, CO

Smith, W. L., S. A. Ackerman, R. O. Knuteson, X. L. Ma and H. E. Revercomb, 1993: AERI observations during FIRE II. FIRE II cirrus Science Team Meeting, Breckenridge, CO

Ackerman, S. A., and R. O. Knuteson, 1993: Multiple scattering algorithm for use with line-by-line RTE models, SPIE's International Symposium on Optical Engineering and Photonics in Aerospace and Remote Sensing, Orlando FL, 12-16 April.

Smith, W. L., M. Xialin, and S. A. Ackerman; 1991: Remote sensing cloud properties from high-spectral resolution infrared observations. Presented at the IAMAP symposium on Aerosol-Cloud-Climate Interactions, Vienna, Aug, 1991.

Takano, Y., K. N. Liou, S. A. Ackerman and P. Minnis; 1991: Effects of small ice crystals on cirrus infrared radiative properties. Presented at the IAMAP symposium on Aerosol-Cloud-Climate Interactions, Vienna, Aug, 1991.

Comparison of upper tropospheric water vapor from GOES, Raman lidar, and cross-chain loran atmospheric sounding system measurements

B. J. Soden, S. A. Ackerman, D. O'C. Starr, S. H. Melfi and R. A. Ferrare

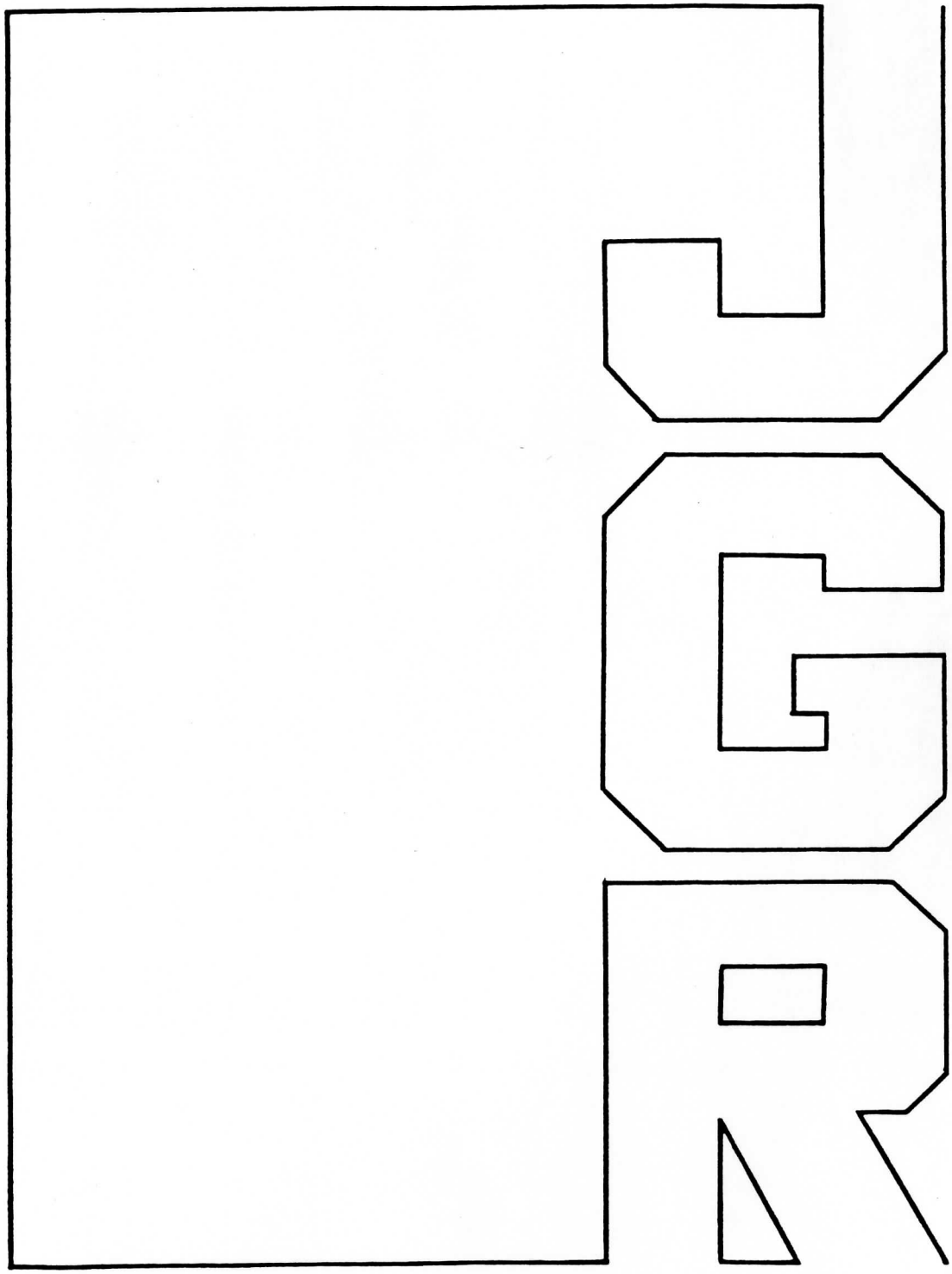

Journal of Geophysical Research, Vol. 99, No. D10, October 20, 1994

JOURNAL OF GEOPHYSICAL RESEARCH, VOL. 99, NO. D10, PAGES 21,005–21,016, OCTOBER 20, 1994

Comparison of upper tropospheric water vapor from GOES, Raman lidar, and cross-chain loran atmospheric sounding system measurements

B. J. Soden[1,2], S. A. Ackerman[3], D. O'C. Starr[4], S. H. Melfi[4], and R. A. Ferrare[5]

Abstract. Observations of upper tropospheric relative humidity obtained from Raman lidar and CLASS sonde instruments obtained during the FIRE Cirrus-II field program are compared with satellite measurements from the GOES 6.7-μm channel. The 6.7-μm channel is sensitive to water vapor integrated over a broad layer in the upper troposphere (roughly 500-200 mbar). Instantaneous measurements of the upper tropospheric relative humidity from GOES are shown to agree to within roughly 6% of the nearest lidar observations and 9% of the nearest CLASS observations. The CLASS data exhibit a slight yet systematic dry bias in upper tropospheric humidity, a result which is consistent with previous radiosonde intercomparisons. Temporal stratification of the CLASS data indicates that the magnitude of the bias is dependent upon the time of day, suggesting a solar heating effect in the radiosonde sensor. Using CLASS profiles, the impact of vertical variability in relative humidity upon the GOES upper tropospheric humidity measurements is also examined. The upper tropospheric humidity inferred from the GOES 6.7-μm channel is demonstrated to agree to within roughly 5% of the relative humidity vertically averaged over the depth of atmosphere to which the 6.7-μm channel is sensitive. The results of this study encourage the use of satellite measurements in the 6.7-μm channel to quantitatively describe the distribution and temporal evolution of the upper tropospheric humidity field.

1. Introduction

Clouds form in moist environments. The First ISCCP Regional Experiment (FIRE) Cirrus-II Implementation Plan (August, 1990) noted the need for mesoscale measurements of upper tropospheric water vapor content. These measurements are required for initializing and verifying numerical weather prediction models, for describing the environments in which cirrus clouds develop and dissipate, and for understanding the role of upper tropospheric water vapor on the radiative energy balance [*Starr and Melfi*, 1991]. The need for accurate upper tropospheric water vapor measurements has been further emphasized by systematic discrepancies noted between different radiosonde sensors [*Garand et al.*, 1992; *Schmidlin*, 1989] and by spurious trends in radiosonde measurements of relative humidity in the upper troposphere [*Elliot and Gaffen*, 1991]. FIRE Cirrus-II took place over Coffeyville Kansas from November 12 to December 7, 1991. During this time, a variety of instruments were deployed to measure the water vapor amounts in the upper troposphere including Raman lidar and Cross-chain Loran Atmospheric Sounding System (CLASS) sondes.

[1]Atmospheric and Oceanic Sciences Program, Princeton University, Princeton, New Jersey.

[2]Now at NOAA Geophysical Fluid Dynamics Laboratory, Princeton, New Jersey.

[3]Cooperative Institute for Meteorological Satellite Studies, University of Wisconsin, Madison.

[4]NASA Goddard Space Flight Center, Greenbelt, Maryland.

[5]Hughes STX Corporation, Lanham, Maryland.

Copyright 1994 by the American Geophysical Union.

Paper number 94JD01721.
0148-0227/94/94JD-01721$05.00

The formation, maintenance, and dissipation of cirrus clouds involve the time variations of the water budget of the upper troposphere. The GOES 6.7-μm radiance observations are sensitive to the upper tropospheric relative humidity in a broad layer extending from roughly 500 to 200 mbar (see Figure 1). High 6.7-μm brightness temperatures indicate a relatively dry upper troposphere and are associated with regions generally free of cirrus clouds. Brightness temperatures that are lower, implying higher relative humidity, may or may not have cirrus present. Animation of time sequences of 6.7-μm images was particularly useful in describing the upper tropospheric synoptic conditions for planning various FIRE Cirrus-II missions. The 6.7-μm observations have also been shown to be valuable for describing the climatology of upper tropospheric water vapor [*Van de Berg et al.*, 1991; *Soden and Bretherton*, 1993] and for comparison with general circulation model simulations to assess model performance [*Soden and Bretherton*, 1994]. A quantitative interpretation of the 6.7-μm measurement is required to successfully incorporate these satellite observations into a description of the upper tropospheric water vapor budget. Recently, *Soden and Bretherton* [1993] described a method of deriving an upper tropospheric relative humidity based upon observations from the GOES 6.7-μm channel. This method is summarized in the next section.

The Raman lidar and CLASS measurements obtained during the FIRE Cirrus-II experiment represent a unique opportunity to verify the GOES upper tropospheric relative humidity measurements by providing state-of-the-art measurements of upper tropospheric water vapor which are independent of the GOES observations. The lidar and CLASS measurements are also valuable for their high vertical resolution in the upper troposphere. This study combines the satellite and independent observations to (1) evaluate the reliability of GOES upper tropospheric humidity observations

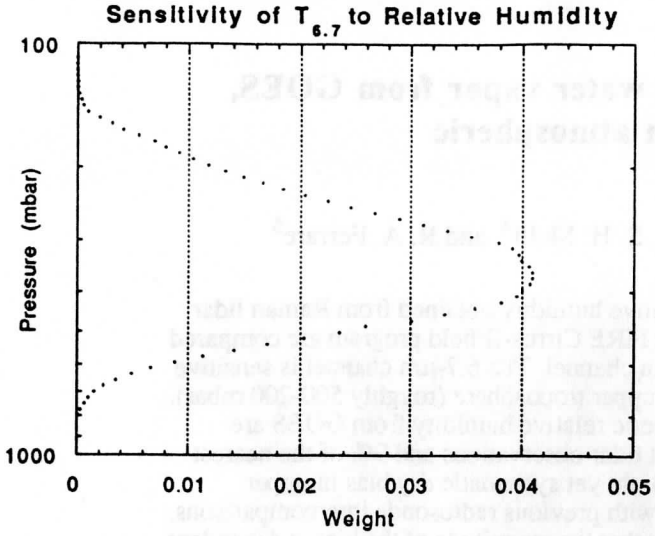

Figure 1. The vertical sensitivity of the 6.7-μm channel to variations in relative humidity. The sum of the weights to individual points is unity.

and (2) examine the impact of vertical variability in the moisture profile upon the GOES upper tropospheric humidity measurements. The next section summarizes the data and analysis procedure used. Section 3 compares the GOES upper tropospheric humidity measurements with simultaneous CLASS and Raman lidar observations. Section 4 examines the effect of vertical variability in relative humidity profile upon the derived product and section 5 summarizes our conclusions.

2. Data and Analysis Procedure

2.1. GOES

Several studies have employed satellite observations in the 6.3-μm water vapor absorption band to describe the distribution of water vapor in the upper troposphere [*Hayden et al.*, 1981; *Schmetz and Turpeinen*, 1988; *Wu et al.*, 1992; *Soden and Bretherton*, 1993]. This paper makes use of 6.7-μm spectral measurements made by the Visible Infrared Spin Scan Radiometer (VISSR) Atmospheric Sounder (VAS) on board GOES 7. The VAS instrument provides 6.7-μm radiances every 30 min with a nadir resolution of approximately 16 km. In-flight calibration of an earlier VAS instrument suggests random noise in individual observations of +/- 0.75 K with possible biases of up to 1.9 K due to calibration uncertainties [*Menzel et al.*, 1981].

Although satellite measurements in the 6.7-μm channel provide a valuable source of information on upper tropospheric water vapor, they have been sorely underutilized for climate studies. One reason for this stems from the difficulty of interpreting brightness temperatures in terms of a more familiar water vapor quantity. *Soden and Bretherton* [1993] addressed this issue by developing an interpretation tool, based upon a simplified model of radiative transfer, which provides a convenient means of interpreting 6.7-μm brightness temperature in terms of an upper tropospheric humidity index (UTH). The UTH corresponds roughly to a vertically averaged relative humidity in a layer from 500 to 200 mbar (or roughly 5.5-12.0 km). A more precise description of the vertical sensitivity of UTH is given in section 4. Using the Goody random band model and assuming strongly-absorbing pressure-broadened lines, *Soden and Bretherton* [1993] demonstrated that for an atmospheric profile corresponding to a constant lapse rate and relative humidity, the 6.7-μm brightness temperature ($T_{6.7}$) varied logarithmically with the ratio of UTH and cosine of the satellite-viewing zenith angle (θ).

$$\log\left(\frac{\mathrm{UTH}}{\cos\theta}\right) = a + bT_{6.7} \qquad (1)$$

The relationship between UTH and $T_{6.7}$ described by equation (1) was determined theoretically based upon a simplified treatment of the radiative transfer at 6.7-μm. In their study, Soden and Bretherton performed detailed calculations of $T_{6.7}$ using the Cooperative Institute for Meteorological Satellite Studies (CIMSS) transmittance model (which includes the GOES 7 spectral response function) and input profiles of temperature and moisture supplied by European Centre for Medium-Range Weather Forecasts (ECMWF) operational analyses for July 1987. The coefficients, a=31.5 and b=-0.115 K^{-1}, were then determined empirically by regressing the simulated $T_{6.7}$ against the corresponding vertically weighted average of the upper tropospheric relative humidity calculated directly from the same ECMWF profiles. In this way, a consistent set of coefficients were derived to relate observed (or simulated) $T_{6.7}$ to UTH. These coefficients were in good agreement with the values expected based upon the theoretical construct of the simplified model. Furthermore, comparison of the simulated $T_{6.7}$ with the corresponding value of UTH calculated directly from the same profiles revealed a relationship in very good agreement with that predicted by equation (1): rms error of roughly 1 K or 8% in terms of UTH. The good agreement and the similarity between the theoretically estimated and empirically determined coefficients support the validity of the simple relationship described by equation (1).

In essence, equation (1) represents a simplification derived from radiative transfer theory and then tuned slightly to ECMWF analyses for July 1987 and the GOES 7 spectral response function. Although these profiles correspond to only a single month of analyses, they do in fact represent a wide range of upper tropospheric conditions [*Soden and Bretherton*, 1994] and consequently the values of the coefficients are insensitive to seasonal variations in the data set used to derive them. This is demonstrated in the first three columns of Table 1 which compare coefficients obtained using ECMWF analyses from January, April, July, and October. The coefficients from all four months vary by less than 3%, indicating that there is little sensitivity to the

Table 1. Seasonal Regression Coefficients From ECMWF Analyses

	a	b	rms (CLASS/ Lidar)	Bias (CLASS/ Lidar)	Corr. (CLASS/ Lidar)
Jan.	31.2	-0.114	8.4/6.2	-6.1/3.0	0.90/0.93
April	32.0	-0.117	9.3/6.9	-6.7/3.3	0.90/0.93
July	31.5	-0.115	8.9/6.4	-6.5/3.2	0.90/0.93
Oct.	30.9	-0.112	9.9/7.3	-7.2/3.5	0.90/0.93

See text for details.

particular set of input profiles used. The GOES 7 satellite was used in both this study and the study by *Soden and Bretherton* [1993]; thus the sensitivity of the coefficients to slight differences in the spectral response function from one satellite to the next are not an issue here. However, we do note that the sensitivity of the coefficients to differing spectral response functions is typically smaller than the seasonal sensitivities shown in Table 1.

Using equation (1) in combination with the coefficients reported by *Soden and Bretherton* [1993] (a=31.5 and b=-0.115 K^{-1}), the UTH is derived over the FIRE Cirrus-II central site for the entire field phase at 1/2-hourly intervals. To compare the satellite observations with the radiosonde and lidar measurements, it is necessary to identify cloud contaminated 6.7-μm measurements. *Soden and Bretherton* [1993] describe a cloud clearance procedure for determining an average clear sky radiance over a region of roughly 2.5° latitude by 2.5° longitude. However, since the independent observations represent point measurements, it is here necessary to retain the highest spatial resolution possible in the satellite data. Consequently, cloud screening is performed by visual inspection of coincident 11-μm (IR window) imagery during the period of study. Since the focus of this report is to compare the GOES observations of upper tropospheric moisture with independent radiosonde and lidar measurements, the development of a cloud clearance algorithm for pixel resolution 6.7-μm data will be the subject of a separate study.

2.2. Raman Lidar

The FIRE Cirrus-II experiment was the first field deployment of a new NASA/GSFC (Goddard Space Flight Center) Raman water vapor lidar system. This lidar, described by *Whiteman et al.* [1992a] and *Ferrare et al.* [1992], incorporated many new features and was significantly improved over the previous system described by *Melfi and Whiteman* [1985], *Melfi et al.* [1989], *Whiteman et al.* [1992b], and *England et al.* [1992]. The characteristics of this new lidar, as operated during the FIRE Cirrus-II experiment, will be discussed here briefly. The system uses a XeF laser to transmit light pulses at 351 nm. A telescope collects the combined aerosol and molecular backscattered light at the laser wavelength as well as Raman scattered light from water vapor (403 nm), nitrogen (383 nm), and oxygen (372 nm) molecules. Beam splitters are used to separate the return signals into low- and high-sensitivity channels; these two channels are employed for each wavelength to measure signals from throughout the troposphere. Photomultiplier tubes detect the backscattered radiation in all channels and provide output signals to photon counters. In normal operation, data from more than 2300 shots are recorded as 1-min profiles with a range resolution of 75 m. The standard errors for these data are computed using Poisson statistics (i.e., the noise is inversely proportional to the square root of the total number of photon counts). In order to enhance the performance at high altitudes, 60 consecutive 1-min profiles were summed together to form hour averages which were used in the comparison. Figure 2 shows the absolute (Figure 2a) and relative (Figure 2b) errors in water vapor mixing ratio as a function of altitude for one-minute (solid line) and one-hour (dashed line) averaging time for typical Spectral Radiative Experiment (SPECTRE) data. The decrease in error for altitudes between 4.0 and 4.5 km corresponds to the

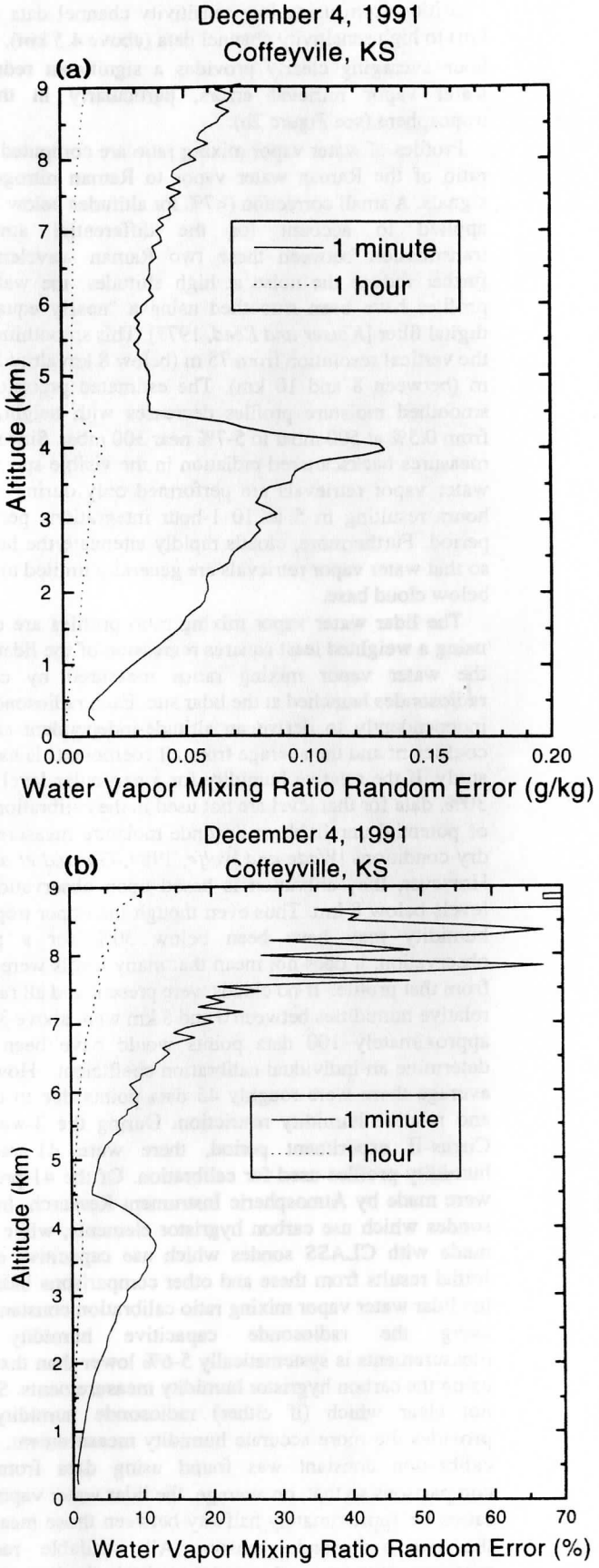

Figure 2. (a) Absolute and (b) relative errors in water vapor mixing ratio as a function of altitude for one-minute (solid line) and one-hour (dashed line) averaging times for typical SPECTRE data.

transition from using low sensitivity channel data (below 4 km) to high sensitivity channel data (above 4.5 km). The one-hour averaging clearly provides a significant reduction in water vapor retrieval errors, particularly in the upper troposphere (see Figure 2b).

Profiles of water vapor mixing ratio are computed from the ratio of the Raman water vapor to Raman nitrogen return signals. A small correction (<7% for altitudes below 12 km) is applied to account for the differential atmospheric transmission between these two Raman wavelengths. To further reduce the noise at high altitudes, the water vapor profiles have been smoothed using a "nearly equal ripple" digital filter [*Kaiser and Reed*, 1977]. This smoothing reduces the vertical resolution from 75 m (below 8 km altitude) to 300 m (between 8 and 10 km). The estimated precision of the smoothed moisture profiles decreases with height, ranging from 0.5% at 500 mbar to 5-7% near 300 mbar. Since the lidar measures backscattered radiation in the visible spectrum, the water vapor retrievals are performed only during nighttime hours resulting in 5 to 10 1-hour integrations per 24-hour period. Furthermore, clouds rapidly attenuate the laser beam so that water vapor retrievals are generally limited to altitudes below cloud base.

The lidar water vapor mixing ratio profiles are calibrated using a weighted least squares regression of the lidar ratios to the water vapor mixing ratios measured by coincident radiosondes launched at the lidar site. Each radiosonde is used independently to derive an altitude-independent calibration coefficient and the average from all coefficients is used in this study. If the relative humidity for a particular level is below 30%, data for that level are not used in the calibration because of potential unreliable radiosonde moisture measurements in dry conditions [*Wade and Wolfe*, 1989; *Garand et al.*, 1992]. However, the calibration is based upon observations at all levels below 8 km. Thus even though the upper tropospheric humidity may have been below 30% for a particular observation, it does not mean that many levels were not used from that profile. If no clouds were present and all radiosonde relative humidities between 0 and 8 km were above 30%, then approximately 100 data points would have been used to determine an individual calibration coefficient. However, on average there were roughly 45 data points due to the cloud and relative humidity restriction. During the 3-week FIRE Cirrus-II experiment period, there were 41 radiosonde humidity profiles used for calibration. Of the 41 profiles, 24 were made by Atmospheric Instrument Research, Inc. (AIR) sondes which use carbon hygristor elements, while 17 were made with CLASS sondes which use capacitive elements. Initial results from these and other comparisons indicate that the lidar water vapor mixing ratio calibration constant derived using the radiosonde capacitive humidity sensor measurements is systematically 5-6% lower than that derived using the carbon hygristor humidity measurements. Since it is not clear which (if either) radiosonde humidity sensor provides the more accurate humidity measurement, the lidar calibration constant was found using data from all 41 comparisons so that, on average, the lidar water vapor mixing ratios lie approximately halfway between those measured by the two radiosonde sensors. All available radiosonde measurements are used in order to obtain the best calibration possible. Since some CLASS sondes are used in the calibration, the lidar measurements are not completely independent of the CLASS measurements. However, both instruments are independent from the GOES data which is the focus of this investigation. Furthermore, the greater reliance of AIR sondes (60%) relative to CLASS sondes (40%) and inclusion of lower tropospheric levels for calibration enhance the independence of the lidar upper tropospheric measurements. If only AIR sondes were used, the lidar humidity measurements would have been roughly 2% higher than the values reported here. In addition, the lidar calibration coefficients are distributed uniformly with time, so that had only a portion of the field experiment been used to calibrate the lidar (enabling the remaining portion to be independent) the calibration would not have differed significantly from the actual value used.

Lidar data above 300 mbar (~ 9.5 km) are not used in the subsequent data analysis because of a problem which is believed to stem from signal-induced noise in the photomultiplier tubes used during this experiment. When present in the high-sensitivity water vapor channel, the noise can produce overestimates of relative humidity at high altitudes where the mixing ratios are small and thus the water vapor signals are weak. Subsequent measurements taken after the FIRE Cirrus-II experiment with different photomultiplier tubes show improved performance in high-altitude water vapor measurements.

2.3. CLASS

In situ measurements of atmospheric profiles of temperature and relative humidity over the FIRE Cirrus-II field site are provided by the Cross-Chain Loran Atmospheric Sounding System (CLASS). The CLASS consists of a model RS80 Vaisala radiosonde equipped with a capacitance moisture sensor and a Loran-C navigation system to determine the sonde trajectory. The temperature and humidity soundings consist of point measurements along the sonde trajectory. The data are smoothed using a 20-s time average yielding profiles with a vertical resolution of roughly 5 mbar. CLASS sondes were launched 5-7 times per day during FIRE Cirrus-II Intensive Observation Periods (IOPs) providing accurate temperature, moisture, and wind information in support of the experiment.

2.4. Comparison Procedure

The GOES observations provide measurements of the relative humidity vertically averaged over a range of pressure in the upper troposphere (roughly 500-200 mbar). The CLASS measurements, on the other hand, yield vertical profiles of temperature and moisture. Therefore to compare GOES UTH with the radiosonde measurements, a two-step "profile-to-satellite" procedure is used. In the first step, CLASS profiles of temperature and moisture are inserted into the CIMSS transmittance model to simulate a $T_{6.7}$ which would be observed by the satellite under those conditions. The second step transforms both the GOES observed $T_{6.7}$ and the CLASS simulated $T_{6.7}$ into UTH quantities using equation (1). Hence the observed and simulated $T_{6.7}$ are treated in a consistent manner. In this way, the use of the empirically derived regression coefficients does not cause spurious differences between the GOES and CLASS UTH because the same coefficients are applied to both the GOES and CLASS $T_{6.7}$. Essentially, it is $T_{6.7}$ which are being compared, only the comparison is being performed in UTH space rather than brightness temperature space to facilitate interpretation of the

results in terms of a more familiar water vapor quantity. This procedure is more accurate than comparing GOES UTH with an explicit vertical average of the relative humidity since it accounts for vertical variations in the moisture profile and the slight temperature dependence of the channel, as well as removing spurious differences between the two data sets which could arise from biases in the empirical coefficients. Hence it provides the accuracy of comparing observed with simulated brightness temperatures as well as an easily interpretable measure of upper tropospheric moisture. An identical procedure was used by *Soden and Bretherton* [1994] to compare GCM profiles of temperature and moisture with GOES observations of $T_{6.7}$.

A similar procedure is used to compare the lidar measurements. Since the lidar provides profiles of moisture only, temperature profiles are interpolated from the nearest radiosonde launches. As mentioned in section 2.2, lidar retrievals above 300 mbar are not used in this study. However moisture profiles up to 100 mbar are needed for the radiative transfer calculations. Therefore to complete the moisture profiles, the relative humidity in the 100 to 300 mbar layer is set equal to the mean relative humidity of the 350 to 300 mbar layer. The precise impact of this filling procedure is difficult to estimate. Inspection of CLASS profiles suggests that relative humidity decreases with height above 300 mbar. Hence, if CLASS profiles are used to estimate the error resulting from the filling procedure, a slight moist bias would be expected. Comparison of the UTH derived from filled CLASS profiles with those obtained from actual CLASS profiles indicates rms differences of approximately 6% with a bias of 3%. However, this bias estimate is strongly dependent upon the accuracy of the CLASS observations from 300 to 100 mbar. Radiosonde measurements in general are suspect at these altitudes due to the low temperatures and resultant small mixing ratios. Indeed, almost all CLASS humidity profiles decrease with height above 300 mbar which could be an indication of reduced sensitivity at high altitudes. Furthermore, water vapor climatologies from SAGE II for 20N-40N [*McCormick and Chiou*, 1994, figures 3 and 4 and table 2], indicate that the relative humidity in the upper troposphere is in fact very nearly constant. Between 300 and 200 mbar (9-11.5 km), typical humidity lapse rates ($dr\!h/dz$) vary from roughly +2%/km to -3%/km depending upon season. For the 200 to 100 mbar layer (11.5-16 km), typical humidity lapse rates are roughly -2.0%/km, although the $T_{6.7}$ is markedly less sensitive to this layer relative to the 300-200 mbar layer (see Figure 1). Using even the largest SAGE humidity lapse rates in place of the constant relative humidity assumption changes the lidar UTH by less than 2%.

3. Intercomparison of UTH Measurements

Time series plots comparing the GOES $T_{6.7}$ (Figures 3a to 3c) and UTH (Figures 3d to 3f) with CLASS and lidar measurements are shown for three different FIRE Cirrus-II IOPs: November 18-22 (Figures 3a and 3d), November 24-26 (Figures 3b and 3e), and December 4-7 (Figures 3c and 3f). These periods provide the densest temporal coverage of CLASS and lidar observations. The UTH for each GOES, CLASS, and lidar data point in Figures 3d to 3f is calculated from the corresponding $T_{6.7}$ in Figure 3a to 3c using equation (1). The GOES measurements are shown by the solid line. Lidar and CLASS observations are denoted by squares and circles, respectively. Observations for times in which the 6.7-μm radiances were contaminated by cloud cover are not shown. The presence of high-frequency variability in the GOES time series is believed to stem primarily from noise in the VAS 6.7-μm sensor [*Soden and Bretherton*, 1993], although natural variability in the UTH field also contributes. The 30-minute fluctuations in $T_{6.7}$ are typically on the order of 1K or roughly 5-10% in terms of UTH and are similar in magnitude to the random instrumental noise in the 6.7-μm channel of 0.75 K reported by *Menzel et al.* [1981] which is ~6% in terms of UTH. Despite the high-frequency variability in the GOES data, analysis of all three periods indicates generally good agreement with both the CLASS and lidar observations. The similarity in the time series of UTH is quite remarkable given the differing spatial characteristics between the GOES and radiosonde/lidar instruments. The extent of the agreement provides confidence in the quantitative use of 6.7-μm satellite measurements to describe the temporal evolution of the upper tropospheric water vapor field over the FIRE Cirrus-II site. The lidar retrievals in particular exhibit good agreement with the GOES data throughout the three IOPs.

Figure 4a shows a scatter plot of the UTH from GOES and lidar measurements. To reduce the impact of instrument noise, the GOES 30-min observations have been smoothed using a 1-2-1 time average centered on the GOES observation nearest the middle of the 1-hour lidar sounding. Temporal averaging is chosen rather than spatial averaging due to an apparent 60-min periodicity in the GOES $T_{6.7}$ noted by *Soden and Bretherton* [1993]. At low to moderate humidities the lidar retrievals tend to be roughly 5% higher than the GOES observations. At higher humidities the bias appears to decrease. The correlation between the GOES and lidar UTH is 0.93 which is significant at the 99% level for 65 degrees of freedom. The rms difference is 6.4%. Thus the GOES and lidar measurements of UTH are consistent to roughly within the estimated uncertainty in either the GOES or lidar retrievals. If the mean bias of 3.2% between the lidar and GOES UTH is removed, the rms difference is reduced to 5.6%. It is worth noting that if the actual lidar profiles rather than the filled profiles are used, both the correlation and bias increase. This suggests that there is a systematic moist bias in the lidar retrievals above 300 mbar but that the observed lidar profiles do correlate well with the presence of moist or dry conditions in the upper troposphere.

For the CLASS observations, the agreement is best during the November 18-22 IOP where differences with the GOES measurements are typically less than 5% UTH. Slightly larger differences resulting from an apparent dry bias in the CLASS relative to the GOES are evident in the subsequent IOPs, although the temporal trends between the GOES and CLASS are still very similar. Despite the systematically lower humidities in the CLASS measurements, the overall agreement between the GOES and CLASS UTH is still quite good as demonstrated in Figure 4b. This figure displays a scatter plot between the UTH derived from both GOES and CLASS measurements. The CLASS UTH are systematically lower than the GOES UTH. The bias increases with increasing UTH from roughly 5% for UTH ~ 15% to 10% for UTH ~ 60%. The correlation between the two observations is 0.90 which is significant at the 99% level for 64 degrees of freedom. The rms difference is 8.9%. When the mean bias of 6.5% is removed, the rms difference between the GOES and CLASS UTH reduces to 6.2%. Table 1 lists the sensitivity of

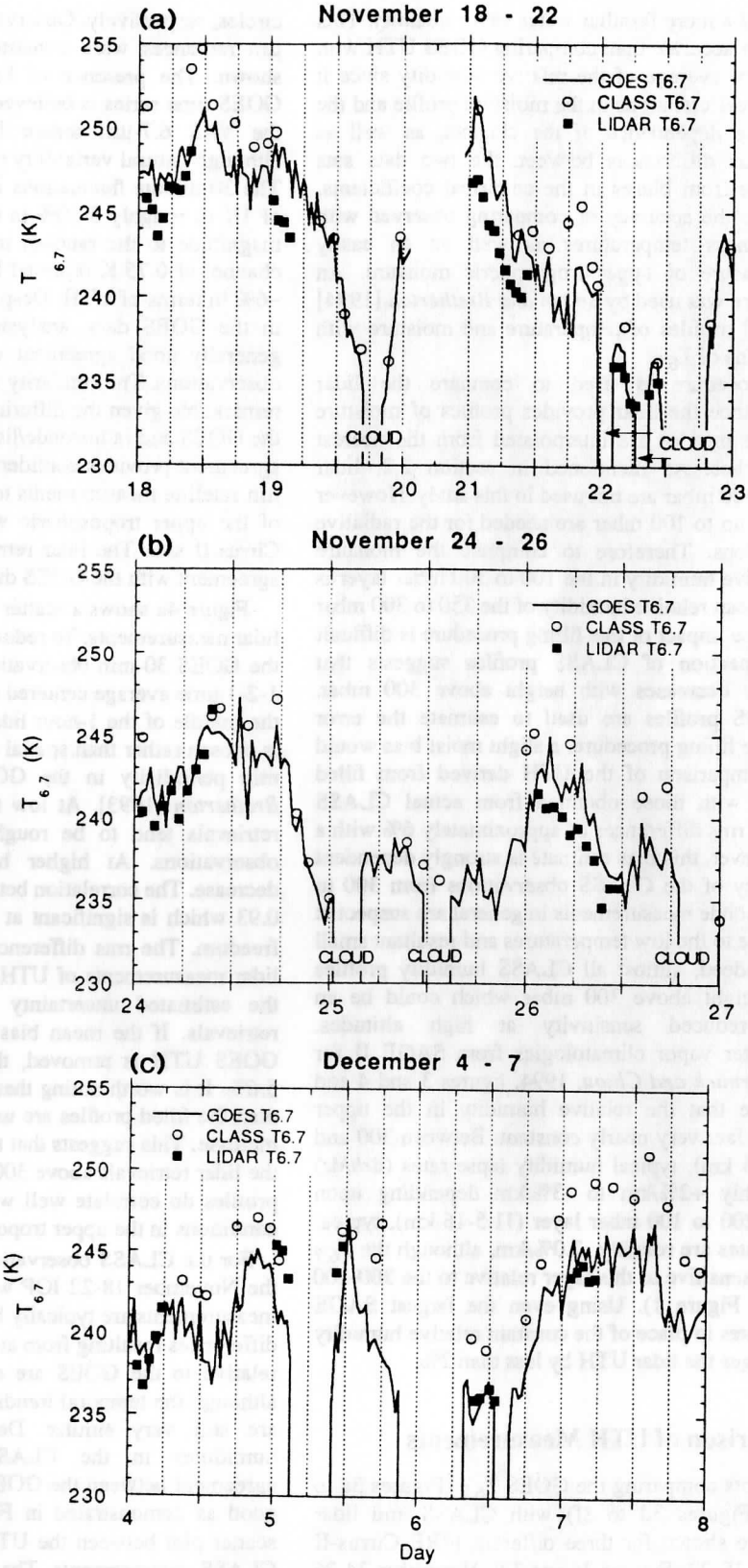

Figure 3. Time series plots of (a-c) $T_{6.7}$ and (d-f) upper tropospheric humidity index (UTH) from GOES (solid line), lidar (squares), and CLASS sondes (circles) for FIRE Cirrus-II Intensive Observation Periods: November 18-22 (Figures 3a and 3e), November 24-26 (Figures 3b and 3d), and December 4-6 (Figures 3c and 3f).

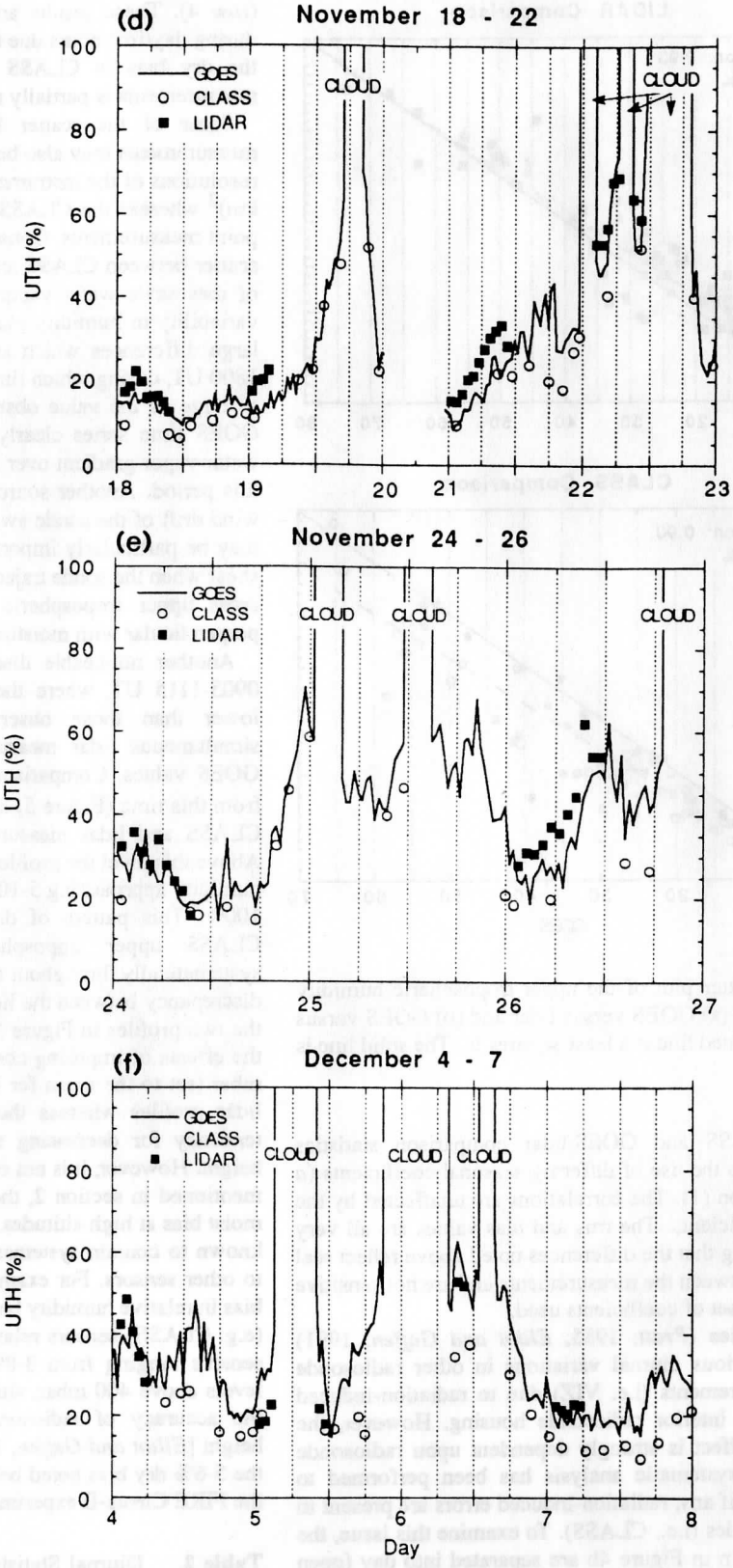

Figure 3. (continued)

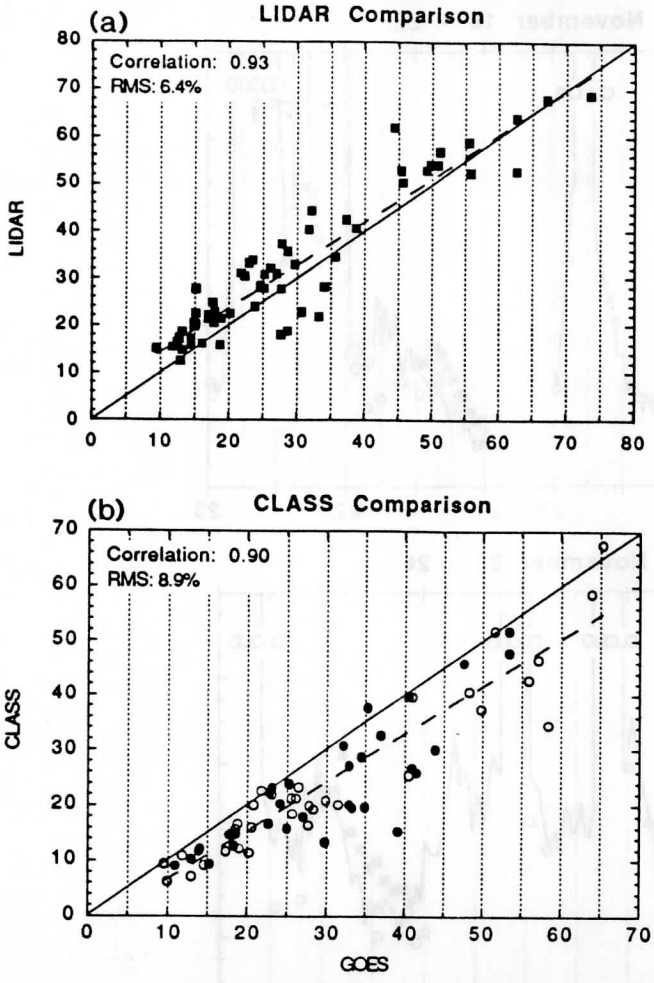

Figure 4. A scatter plot of the upper tropospheric humidity index (UTH) for (a) GOES versus lidar and (b) GOES versus CLASS. The dashed line is a least-squares fit. The solid line is a perfect fit.

the GOES/CLASS and GOES/lidar comparison statistics (bias and rms) to the use of differing seasonal coefficients (*a* and *b*) in equation (1). The correlations are unaffected by the changes in coefficients. The rms and bias values are all very similar, indicating that the differences noted above reflect real discrepancies between the measurements and are not sensitive to the particular set of coefficients used.

Previous studies (*Pratt*, 1985; *Elliot and Gaffen*, 1991) have noted spurious diurnal variations in other radiosonde humidity measurements (i.e. VIZ) due to radiation-induced warming of the interior radiosonde housing. However, the impact of this effect is strongly dependent upon radiosonde design and no systematic analysis has been performed to determine what, if any, radiation-induced errors are present in Vaisala radiosondes (i.e., CLASS). To examine this issue, the data points shown in Figure 4b are separated into day (open circles) and night (solid circles) categories. Table 2 lists statistics calculated separately for each category. The daytime measurements exhibit a larger bias, larger rms difference, and smaller correlation than the nighttime measurements. If the daytime measurements are further stratified into mid-day observations (+/- 2 hours of local noon), the disparity between GOES and CLASS measurements becomes noticeably larger (row 4). These results are consistent with increased errors during daytime hours due to radiative heating, suggesting that the dry bias in CLASS measurements relative to GOES measurements is partially attributable to this effect.

Some of the scatter between the GOES and CLASS measurements may also be attributable to the differing spatial resolutions of the instruments; the GOES pixel is roughly (16 km)^2 whereas the CLASS observations essentially represent point measurements. Consequently, one would expect greater scatter between CLASS and GOES observations in situations of mesoscale water vapor gradients. For example, subpixel variability in humidity may be responsible for the unusually large differences which are evident on December 5, 1700-1800 UT, during which time the CLASS UTH is roughly half as large as the value observed by GOES. Inspection of the GOES time series clearly indicates the passage of a large water vapor gradient over the FIRE Cirrus-II site just prior to this period. Another source of discrepancy could stem from wind drift of the sonde away from the central FIRE site. This may be particularly important in situations of strong vertical shear when the sonde trajectory at lower levels may cause it to cross upper tropospheric streamlines which are typically perpendicular with moisture gradients.

Another noticeable discrepancy occurs on December 6, 0905-1115 UT, where the CLASS UTHs are considerably lower than those observed by GOES. However, near simultaneous lidar measurements are very similar to the GOES values. Comparison of the relative humidity profiles from this time (Figure 5) shows good agreement between the CLASS and lidar measurements up to roughly 350 mbar. Above this level the profiles diverge, with the CLASS relative humidity approaching 5-10%, while the lidar values approach 100%. This pattern of discrepancy between the lidar and CLASS upper tropospheric humidity profiles appears systematically throughout the FIRE Cirrus-II experiment. The discrepancy between the lidar and CLASS values of UTH for the two profiles in Figure 5 is at least partially attributable to the effects of imposing constant relative humidity above 300 mbar (set to the mean for the 350 to 300 mbar layer) for the lidar profiles whereas the CLASS profiles show a strong tendency for decreasing relative humidity with increasing height. However, it is not obvious which is more accurate. As mentioned in section 2, the lidar retrievals have a suspected moist bias at high altitudes. The CLASS observations are also known to contain systematic biases at high altitudes relative to other sensors. For example, *Schmidlin* [1989] noted a dry bias in relative humidity between 500-400 mbar for capacitive (e.g. CLASS) sensors relative to carbon hygristor (e.g. VIZ) sensors ranging from 3-8%. No results were presented for levels above 400 mbar, although it is generally believed that the accuracy of radiosonde measurements degrades with height [*Elliot and Gaffen*, 1991]. This result agrees well with the 5-6% dry bias noted between CLASS and AIR sondes for the FIRE Cirrus-II experiment (section 2.2).

Table 2. Diurnal Statistics for CLASS Versus GOES Comparison

	Bias	rms	Correlation
Night	-5.8	7.8	0.94
Day	-6.6	8.6	0.86
Mid-day	-9.6	10.9	0.84

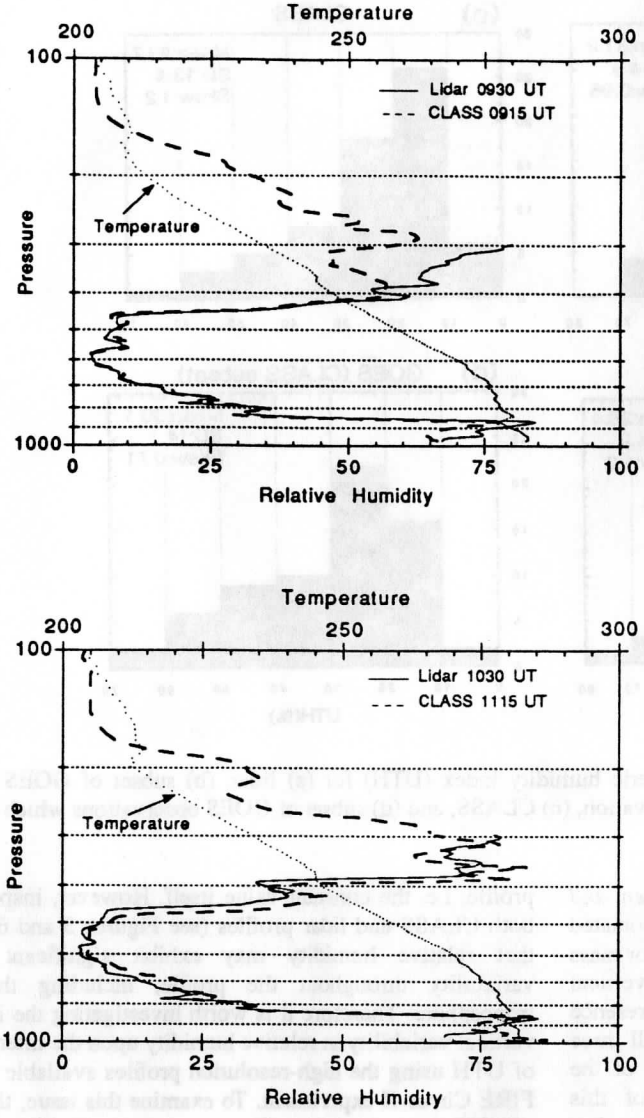

Figure 5. Profiles of relative humidity from lidar (solid) and CLASS sondes (dashed) for December 6, 1991, (top) nearest 0930 UT and (bottom) nearest 1115 UT. Lidar data above 300 mbar are not used in the comparisons with GOES.

Inspection of simultaneous lidar and CLASS profiles from periods when cirrus are present also supports the hypothesis of a dry bias in the CLASS measurements. Figure 6 compares profiles of CLASS relative humidity with the nearest corresponding 1-hour lidar retrieval for December 5 at 0530 and 0930 UT. In both of these profiles, the lidar detects cirrus with a base near 300 mbar and shows increasing relative humidity up to this level where saturation is reached, although the reliability of the humidity profile above cloud base is questionable due to increased cloud contamination. The CLASS relative humidities also increase near the cloud base; however, saturation is never reached. Peak relative humidities in the cloud layer are 50-65% with respect to water or roughly 75-90% with respect to ice. The undersaturation in the cloud layer suggests a dry bias in the CLASS measurements in approximate agreement with that noted by *Schmidlin* [1989], such a bias could explain the systematically lower CLASS UTH estimates relative to the GOES and lidar observations.

Figure 7 depicts histograms of UTH computed from the CLASS (lidar) measurements and from the corresponding subsets of GOES observations which most closely coincide with the CLASS (lidar) observation. Statistics for each distribution are written in the upper right-hand corner. The mean CLASS UTH is roughly 6% lower than the corresponding GOES value. In contrast, the mean lidar UTH is roughly 3% higher than the GOES value. The fact that the GOES measurements are higher than the CLASS observations yet slightly lower than the lidar observations is encouraging, suggesting that the impact of instrumental bias in the 6.7-μm channel upon the derived UTH is smaller than what we are able to resolve given the present uncertainties of the independent observations. Another interesting feature of the histograms is the noticeable positive skew in the distribution, i.e., skew toward larger values. This shape is

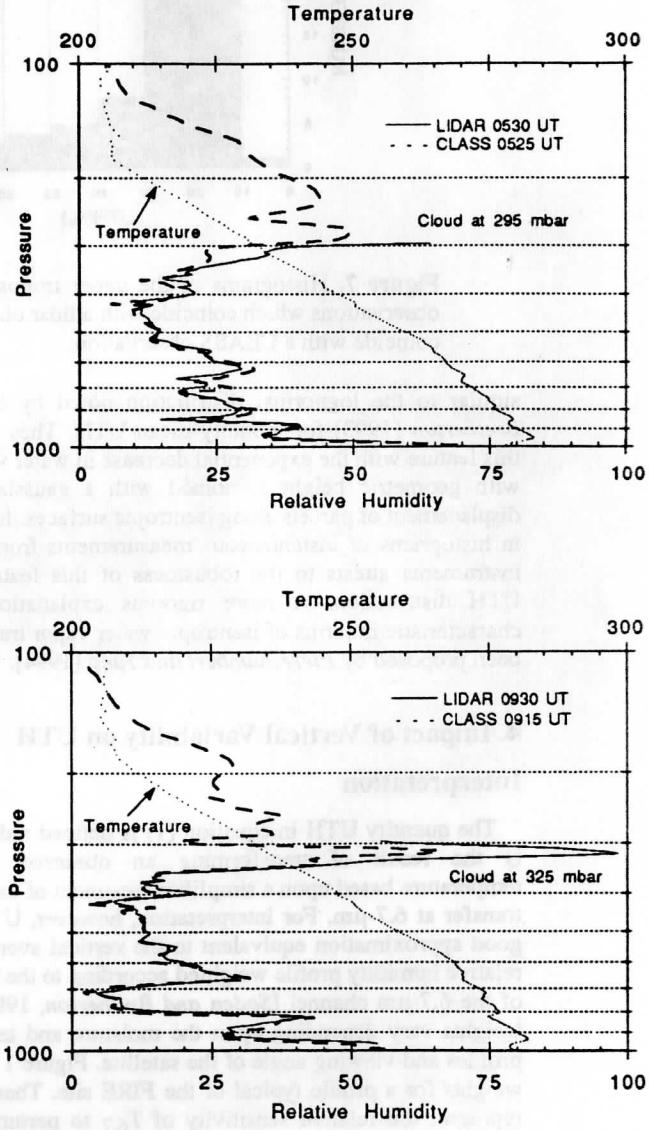

Figure 6. Profiles of relative humidity from lidar (solid) and CLASS sondes (dashed) for sondes launches at (top) 0530 UT and (bottom) 0930 UT. The lidar retrievals are the one-hour averages nearest the CLASS sonde launch. The cloud base pressure is printed in the upper right-hand corner of each profile. Lidar data above 300 mbar are not used in the comparisons with GOES.

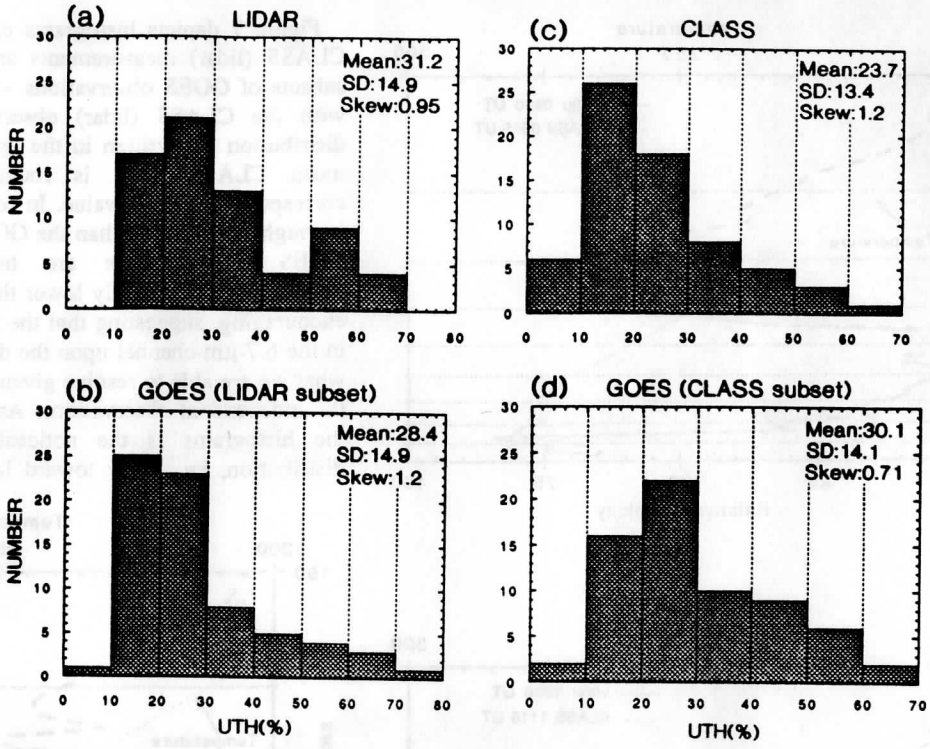

Figure 7. Histograms of the upper tropospheric humidity index (UTH) for (a) lidar, (b) subset of GOES observations which coincide with a lidar observation, (c) CLASS, and (d) subset of GOES observations which coincide with a CLASS observation.

similar to the lognormal distribution noted by *Soden and Bretherton* [1993] for monthly mean UTH. They associated this feature with the exponential decrease in water vapor mass with geometric height combined with a gaussian vertical displacement of parcels along isentropic surfaces. Its presence in histograms of instantaneous measurements from all three instruments attests to the robustness of this feature of the UTH distribution. A more rigorous explanation of this characteristic in terms of isentropic water vapor transport has been proposed by *Pierrehumbert and Yang* [1994].

4. Impact of Vertical Variability on UTH Interpretation

The quantity UTH in equation (1) is defined radiatively. It is the result of transforming an observed brightness temperature based upon a simplified treatment of the radiative transfer at 6.7-μm. For interpretation, however, UTH is to a good approximation equivalent to the vertical average of the relative humidity profile weighted according to the sensitivity of the 6.7-μm channel [*Soden and Bretherton*, 1993]. These weights vary depending upon the moisture and temperature profiles and viewing angle of the satellite. Figure 1 shows the weights for a profile typical of the FIRE site. These weights represent the relative sensitivity of $T_{6.7}$ to perturbations in relative humidity, in thin layers equally spaced in log pressure.

In deriving the expression for UTH in equation (1), Soden and Bretherton assumed a uniform relative humidity throughout the layer to which the 6.7-μm channel is sensitive (roughly 500-200 mbar). The derived UTH corresponds to a vertically-weighted average of this constant relative humidity profile, i.e. the constant value itself. However, inspection of both CLASS and lidar profiles (see Figures 5 and 6) reveals that relative humidity may exhibit significant vertical variability throughout the profile, including the upper troposphere. Therefore it is worth investigating the impact of vertical variability in relative humidity upon the interpretation of UTH using the high-resolution profiles available from the FIRE Cirrus-II experiment. To examine this issue, the values of UTH determined from $T_{6.7}$ calculated using CLASS sonde profiles of temperature and relative humidity are compared to a vertically-averaged relative humidity ($\overline{RH}^{wt}$) using the weights from Figure 1 applied to the corresponding relative humidity profile. The results are shown in Figure 8 as solid circles. The correlation between $\overline{RH}^{wt}$ and UTH is 0.95, and the rms difference is roughly 5% relative humidity. Hence the comparison using high resolution soundings provide further evidence that vertical variability in the humidity profile does not significantly affect the interpretation of UTH from GOES 6.7-μm observations. The requirement of weighting the relative humidity profile according to the sensitivity of the 6.7-μm channel can complicate the interpretation of UTH. Therefore a simpler comparison using the linearly averaged relative humidity between 200 and 500 mbar,

$$\overline{RH}^{lin} = (1/(z_{200} - z_{500})) \int_{z_{500}}^{z_{200}} rh\,dz \qquad (2)$$

is also shown in Figure 8 (open circles). The agreement between UTH and $\overline{RH}^{lin}$ is only slightly worse than with $\overline{RH}^{wt}$: r=0.94, rms=6%. We note, however, that these results are based upon a limited sample of observations from a single geographic location. Thus the vertical variability in these profiles may not be representative of that for all locations.

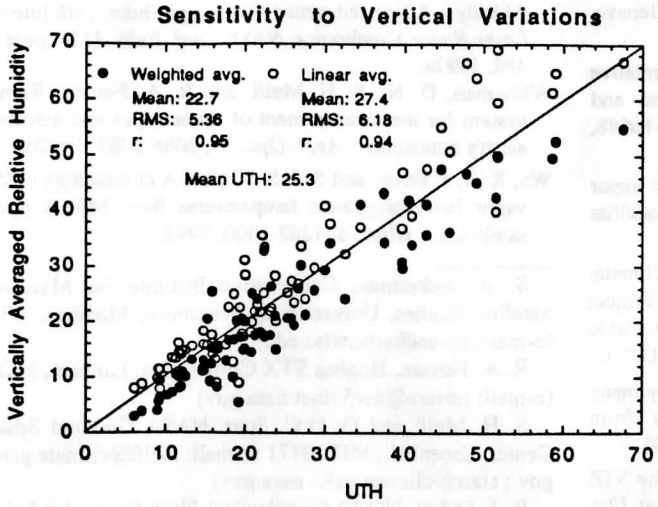

Figure 8. A scatter plot of the upper tropospheric humidity index (UTH) versus $\overline{RH}^{wt}$ (solid circles) and $\overline{RH}^{lin}$ (open circles) based upon calculations from CLASS profiles of temperature and relative humidity

Nevertheless, the results for this region suggest that, to a reasonable approximation, UTH may be interpreted simply as a linear average of the relative humidity profile through the appropriate depth of atmosphere. However, since the depth of atmosphere to which the 6.7-μm channel is sensitive shifts systematically with the temperature and moisture profile and the satellite viewing angle, the comparison of observed $T_{6.7}$ with relative humidity profiles should be accomplished by performing radiative transfer calculations using the temperature and moisture profiles as input. The resulting comparison of calculated and observed $T_{6.7}$ can then be interpreted by transforming both into UTH as was done in section 3.

5. Conclusions

Observations of upper tropospheric relative humidity from the GOES 6.7-μm channel were compared with Raman lidar and CLASS sonde measurements from the FIRE Cirrus-II field experiment. The GOES measurements exhibited very good agreement with both the lidar and CLASS sonde observations. A correlation of 0.93 and an rms difference of 6.4% UTH were noted between the GOES and lidar measurements. A correlation of 0.90 and an rms difference of 8.9% UTH were noted between the GOES and CLASS sonde measurements. The slightly larger differences between the GOES and CLASS measurements stem from a systematic underestimate in the upper tropospheric moisture relative to the GOES observations. This bias is consistent with that noted in a recent radiosonde intercomparison by *Schmidlin* [1989]. A temporal stratification of the CLASS data suggests that the magnitude of this bias is dependent upon time of day and may indicate a solar heating effect on the radiosonde sensor. The good overall agreement between GOES and independent observations of UTH combined with the greater spatial and temporal coverage afforded by satellites encourages the use of 6.7-μm measurements to accurately describe the distribution and temporal evolution of the upper tropospheric water vapor field.

The impact of vertical variability upon the interpretation of the derived UTH was also studied. Comparison of the UTH determined from CLASS profiles of temperature and relative humidity with the corresponding vertically averaged relative humidity indicates that vertical variability in the relative humidity profile does not significantly affect the interpretation of $T_{6.7}$ in terms of UTH. The results suggest that the inferred UTH is typically within about 5% of the relative humidity vertically averaged over the depth of atmosphere to which the 6.7-μm channel is sensitive (500-200 mbar).

Acknowledgements. We wish to thank personnel at GSFC (Dave Whiteman and Keith Evans) and at Sandia National Labs (John Goldsmith, Scott Bisson, and Marshall Lapp) who were responsible for the GSFC Raman lidar data acquisition. We also thank Hal Woolf for assistance with the CIMSS transmittance model, Don Wylie for archiving the GOES data, and Leo Donner, V. Ramaswamy, and two anonymous reviewers for their suggestions.

References

Elliot, W. P. and D. J. Gaffen, On the utility of radiosonde humidity archives for climate studies, *Bull. Am. Meteorol. Soc.*, *72*, 1507-1520, 1991

England, M.N., R.A. Ferrare, S.H. Melfi, and D.N. Whiteman, Atmospheric water vapor measurements: Comparison of microwave radiometry and lidar, *J. Geophys. Res.*, *97*, 899- 916, 1992.

Ferrare, R.A., S.H. Melfi, D.N. Whiteman, and K.D. Evans. Raman lidar measurements of Pinatubo aerosols over southeastern Kansas during November-December 1991, *Geophys. Res. Lett.*, *19*, 1599-1602, 1992.

Garand, L., C. Grassotti, J. Halle, and G. L. Klein, On differences in radiosonde humidity-reporting practices and their implications for numerical weather prediction and remote sensing, *Bull. Am. Meteorol. Soc.*, *73*, 1417-1423, 1992.

Hayden, C. M., W. L. Smith, and H. M. Woolf, Determination of moisture from NOAA polar orbiting satellite sounding radiances, *J. Appl. Meteorol.*, *20*, 450-466, 1981.

Kaiser, J. F. and W. A. Reed, Data smoothing using low-pass digital filters, *Rev. Sci. Instrum.*, *48*, 1447-1457, 1977.

McCormick, M. P. and E. W. Chiou, Climatology of water vapor in the upper troposphere and lower stratosphere determined from SAGE II observations, Paper presented at *5th Symposium on Global Change Studies*, Am. Meteorol. Soc., Nashville, TN, January 6-10, 1994.

Melfi, S.H. and D.N. Whiteman, Observation of lower atmospheric moisture structure and its evolution using a Raman lidar, *Bull. Amer. Meteorol. Soc.*, *66*, 1282-1292, 1985.

Melfi, S.H., D.N. Whiteman, and R. Ferrare, Observation of atmospheric fronts using Raman lidar moisture measurements, *J. Appl. Meteorol.*, *28*, 789-806, 1989.

Menzel, W. P., W. L. Smith, and L. D. Herman, Visible infrared spin-scan radiometer atmospheric sounder radiometric calibration: An in-flight evaluation from intercomparison with HIRS and radiosonde measurements, *Appl. Opt.*, *15*, 358-363, 1981.

Pierrehumbert, R. T. and H. Yang, Production of dry air by isentropic mixing, *J. Atmos. Sci.*, in press, 1994.

Pratt, R. W., Review of radiosonde humidity and temperature errors, *J. Atmos. and Oceanic Tech.*, *2*, 404-407, 1985.

Schmetz, J and O. M. Turpeinen, Estimation of upper tropospheric relative humidity file from METEOSAT water vapor image data, *J. Clim. Appl. Meteorol.*, *27*, 889-899, 1988.

Schmidlin, F. J., *WMO International radiosonde intercomparison,*

phase II, final report, 113 pp., World Meteorol. Organ., Geneva, Switzerland, 1989.

Soden, B. J. and F. P. Bretherton, Upper tropospheric relative humidity from the GOES 6.7-μm channel: Method and climatology for July 1987, *J. Geophys. Res.*, *98*, 16669-16688, 1993.

Soden, B. J. and F. P. Bretherton, Evaluation of the water vapor distribution in general circulation models using satellite observations, *J. Geophys. Res.*, *99*, 1187-1210, 1994.

Starr, D. O'C., and S. H. Melfi, The role of water vapor in climate: A strategic research plan for the GEWEX Water Vapor Project (GVaP). *NASA Conf. Publ. CP-3120*, 50 pp., 1991. (Available from International GEWEX Project Office, Washington, D.C.).

Van de Berg, L., A. Pyomjamsri, and J. Schmetz, Monthly mean upper tropospheric humidities in cloud free areas from METEOSAT observations, *Int. J. Clim.*, *11*, 819-826. 1991.

Wade, Charles G. and Daniel E. Wolfe, Performance of the VIZ carbon hygristor in a dry environment, paper presented at *12th Conference on Weather Analysis and Forecasting*, Am. Meteorol. Soc., Monterey, Calif., October 16-20, 1989.

Whiteman, D. N., S. H. Melfi, R. A. Ferrare, K. A. Evans, L. Ramos-Izquierdo, O.G. Staley, R. D. Di Silvestre, I. Gorin, K. R. Kirks, W. A. Mamakos, L. S. Wan, N. W. Walsh, R. L. Aldridge, Advanced raman water vapor lidar, *16th International Laser Radar Conference, NASA Conf. Publ. 3158, part 2*, 483 - 484, 1992a.

Whiteman, D. N., S. H. Melfi, and R. A. Ferrare, Raman lidar system for the measurement of water vapor and aerosols in the earth's atmosphere, *Appl. Opt.*, *31*, 3068-3082, 1992b.

Wu, X., J. J. Bates, and S. J. S. Khalsa, A climatology of the water vapor band brightness temperatures from NOAA operational satellites, *J. Clim.*, *6*, 1282-1300, 1992.

S. A. Ackerman, Cooperative Institute for Meteorological Satellite Studies, University of Wisconsin, Madison, WI 53706. (e-mail:stevea@ssec.wisc.edu)

R. A. Ferrare, Hughes STX Corporation, Lanham, MD 20706. (e-mail: ferrare@mv5.dnet.nasa.gov)

S. H. Melfi and D. O'C. Starr, NASA Goddard Space Flight Center, Greenbelt, MD 20771 (e-mail: melfi@climate.gsfc.nasa.gov : starr@climate.gsfc. nasa.gov)

B. J. Soden, NOAA/Geophysical Fluid Dynamics Laboratory, P.O. Box 308, Princeton University, Princeton, NJ 08540. (e-mail: bjs@gfdl.gov)

(Received November 15, 1993; revised May 4, 1994; accepted June 27, 1994.)

Reprinted from JOURNAL OF THE ATMOSPHERIC SCIENCES, Vol. 52, No. 23, 1 December 1995
American Meteorological Society

Cirrus Cloud Properties Derived from High Spectral Resolution Infrared Spectrometry during FIRE II. Part II: Aircraft HIS Results

S. A. ACKERMAN, W. L. SMITH, A. D. COLLARD, X. L. MA, H. E. REVERCOMB, AND R. O. KNUTESON

Cirrus Cloud Properties Derived from High Spectral Resolution Infrared Spectrometry during FIRE II. Part II: Aircraft HIS Results

S. A. ACKERMAN, W. L. SMITH, A. D. COLLARD, X. L. MA, H. E. REVERCOMB, AND R. O. KNUTESON

Cooperative Institute for Meteorological Satellite Studies, Space Science and Engineering Center, University of Wisconsin-Madison Madison, Wisconsin

(Manuscript received 19 July 1994, in final form 8 December 1994)

ABSTRACT

This paper presents analysis of cloud observations by the High-Resolution Interferometer Sounder made from the NASA ER-2 aircraft during FIRE II. Clear and cloudy sky radiance spectra are presented in terms of differences between observations and radiative transfer model simulations.

Doubling/adding radiative transfer model simulations demonstrate that the magnitude of the brightness temperature differences (ΔBT) is a function of the cloud particle size distribution and the cloud ice water path. For effective radii greater than approximately 30 μm (size parameter of 18) there is little spectral variation in the brightness temperature (BT). An analysis of brightness temperature differences indicates that cirrus clouds over the FIRE II central site possessed a small-particle mode. The cases analyzed had similar appearances in a plot of ΔBT between 11 and 12 μm ($BT_{11} - BT_{12}$) versus the observed ΔBT between 8 and 11 μm ($BT_8 - BT_{11}$), suggesting similarity in the microphysical properties of nongray cirrus. Brightness temperature differences between cirrus cloud over the central site and the Gulf of Mexico are presented to illustrate differences in the cirrus microphysical properties at the two different locations.

Cloud effective emissivities and effective radiative temperatures were derived for observations over the FIRE central site using complementary lidar and radiosonde data. Small variations in these effective properties were seen on 5 December and 22 November. Although they had similar effective temperatures, the emissivities were very different. Very few clouds were observed to have an emissivity near unity.

1. Introduction

The First International Satellite Cloud Climatology Project (ISCCP) Regional Experiment (FIRE) is a multidisciplinary research program designed to study the roles clouds play in the global climate and to improve cloud monitoring techniques from satellite platforms (Cox et al. 1987). In November and December of 1991 the second cirrus field phase of FIRE (FIRE II) took place over the midwestern United States, with the central ground site located in Coffeyville, Kansas. In support of this experiment the High Resolution Interferometer Sounder (HIS) was flown on board the NASA ER-2, stationed in Houston, Texas. The HIS is a Michelson interferometer with a spectral resolving power ($\lambda/\Delta\lambda$) of approximately 3000 covering the spectral range from 3.5 to 17 μm.

The research objectives of FIRE Phase II include quantifying the capabilities and limitations of various cirrus cloud satellite retrieval techniques, improving our capabilities of describing cirrus cloud properties utilizing passive radiometric observations, and improving our understanding of the relationship between the microphysical and radiative properties of cirrus clouds. This paper addresses these issues using the HIS observations for five FIRE II days. The impact clouds have on the spectral distribution of infrared radiation is discussed. Potential uses of various channels for passive remote sensing of clouds is demonstrated. The coupling between the cloud microphysical and radiative properties using radiative transfer modeling is investigated, and results of cloud detection techniques and cloud radiative property retrievals are presented.

2. Instrument description

This section gives a brief discussion of the HIS instrument. A more detailed description of the HIS instrument is given in Part I of this series (Smith et al. 1995) and by Revercomb et al. (1988). This paper uses the HIS spectra at an apodized resolution of approximately 0.5 cm^{-1} from 600 to 1080 cm^{-1} (16.7–9.3 μm) and 1.0 cm^{-1} resolution from 1080 to 1800 cm^{-1} (9.3–5.6 μm) and 2000–2800 cm^{-1} (5.0–3.6 μm). Detection in each of the three spectral bands is performed using liquid helium cooled arsenic doped silicon detectors contained in a single detector/dewar assembly. Three detector/filter systems are used to optimize the signal to noise ratio of the observations

Corresponding author address: Dr. William L. Smith, CIMSS, Space Science and Engineering Center, University of Wisconsin-Madison, 1225 W. Dayton St., Madison, WI 53706.

© 1995 American Meteorological Society

through the broad spectral region measured. The instrument includes its own dual-drive recording system, which enables up to 9 h of data to be collected. Onboard high emissivity, temperature controlled reference blackbodies are used for an absolute calibration. A calibration cycle of HIS interferograms consists of 4 cold blackbody views, 4 hot blackbody views, and 12 earth views. The blackbody views are used for the calibration of the earth views. The HIS has a noise equivalent temperature and reproducibility of about 0.25 K over much of the spectrum. At the typical flying altitude of the ER-2, approximately 19 km, the ground resolution of the HIS nadir observation is approximately 2 km.

3. Data overview

This paper concerns observations made from the ER-2 aircraft on five days of FIRE II, 22, 24, and 26 November and 4–5 December. The flight paths of the ER-2 aircraft on these days are shown in Fig. 1. Each aircraft flight track overlays a *GOES-7* infrared (IR) image at approximately 1900 UTC. Two flights were over the Gulf of Mexico, 24 November and 4 December, while the others where focused on the Kansas surface central site located at Coffeyville. The ER-2 was stationed in Houston, Texas, during the experiment. In the analysis that follows all the HIS-measured spectra are for horizontal flight legs of the ER-2.

Figures 2–4 are summaries of the HIS observations made on these FIRE II days. Each period is represented by the mean radiance [mW m^{-2} $(cm^{-1})^{-1}$ sr^{-1}] and plus and minus one standard deviation as a function of wavenumber, (cm^{-1}) (wavelength intervals, μm are given on the top abscissa). The maximum and minimum spectral radiances, which represent the maximum or minimum radiance observed at the particular wavenumber, are also shown. Band I (600–1080 cm^{-1}) observations are shown in Fig. 2, while Figs. 3 and 4 depict the variations observed in band II (1080–1800 cm^{-1}) and band III (2000–2800 cm^{-1}), respectively. Largest variations in terms of the standard deviation in the window region 1250–830 cm^{-1} (8–12 μm) were observed on 22 November and were approximately $\pm$25 mW m^{-2} $(cm^{-1})^{-1}$ sr^{-1}. This is expected because, as seen in the satellite image, the aircraft overflew relatively clear regions until reaching the middle of Oklahoma after which it was over clouds. Many of these clouds were optically thick, as seen in the plot of the minimum radiance in all three bands for this day. Standard deviations in the window region on 4–5 December were approximately $\pm$10 mW m^{-2} $(cm^{-1})^{-1}$ sr^{-1} and on 24 and 26 November they were $\pm$20 mW m^{-2} $(cm^{-1})^{-1}$ sr^{-1}. High optically thick cirrus clouds were also overflown on 24 and 26 November, as seen in the minimum radiances. The Gulf flight mission on 24 November was an overflight of high clouds (see Fig. 1). Stratus were also observed beneath regions of this cloud system by the Cloud and Aerosol Lidar System (CALS), provided by Dr. J. Spinhirne (Spinhirne et al. 1995). Section 6b compares measurements of the IR properties of this subtropical cloud with observations of cirrus over the central site. Cirrus on 22 and 26 November were associated with midlatitude cyclonic systems. Maximum radiances were observed on 4 December when the ER-2 overflew the warm Gulf region. No cirrus were observed on this experiment day, as can be inferred in the warm minimum radiances in the 1300–1800 cm^{-1} band (5.6–7.7 μm) and in the relatively high minimum radiances of band III. Low-level clouds were also observed on 26 November. Maximum observed radiances tend to show an increase around 2600 cm^{-1} (less than 3.8 μm), which is associated with solar reflection. Wavenumbers larger than approximately 2700 cm^{-1} (less than 3.7 μm) display a "spikiness" in the maximum radiance due to an increase in instrument noise, which may be reduced by averaging adjacent spectra.

4. Observed clear minus cloudy radiances

The radiative effects of clouds on the radiation budget of the earth–atmosphere system has been investigated by various authors (Charlock and Ramanathan 1985; Ramanathan et al. 1989; Harrison et al. 1990). The difference between a clear-sky and a cloudy-sky radiative energy budget has been termed "cloud radiative forcing." This cloud forcing was defined in terms of the solar and longwave spectrum as

$$\mathrm{SWCF} = \mathrm{SW}_{\mathrm{clr}} - \mathrm{SW}_{\mathrm{obs}} \quad (1)$$

$$\mathrm{LWCF} = \mathrm{LW}_{\mathrm{clr}} - \mathrm{LW}_{\mathrm{obs}}, \quad (2)$$

where the subscript clr denotes clear-sky radiance and obs an observed (cloud and/or clear sky) radiance. Observations from the Earth Radiation Budget Experiment (ERBE) have recently provided estimates of the shortwave (SW) and longwave (LW) broadband cloud radiative forcing (Ramanathan et al. 1989; Harrison et al. 1990; Li and Leighton 1991; Stephens and Greenwald 1991). Such studies are not only useful in understanding the role of clouds on modifying the radiation budget but, when compared to output from general circulation models (GCMs), are useful in indicating areas where the GCM needs improvement. Observations from ERBE have suggested that on a global mean the shortwave cloud forcing dominates the longwave cloud forcing so that clouds tend to cool the planet (negative cloud forcing). How this cloud forcing varies with cloud type and how clouds modify the clear-sky spectral distribution of radiative energy is not well quantified. The importance of temperature, humidity, and cloud structure on assessing the radiative impacts of clouds was recently demonstrated by Hartmann and Doelling (1991), using broadband ERBE data, and Ackerman et al. (1992), using combined observations of AVHRR, HIRS/2, and ERBE data. Cloud forcing

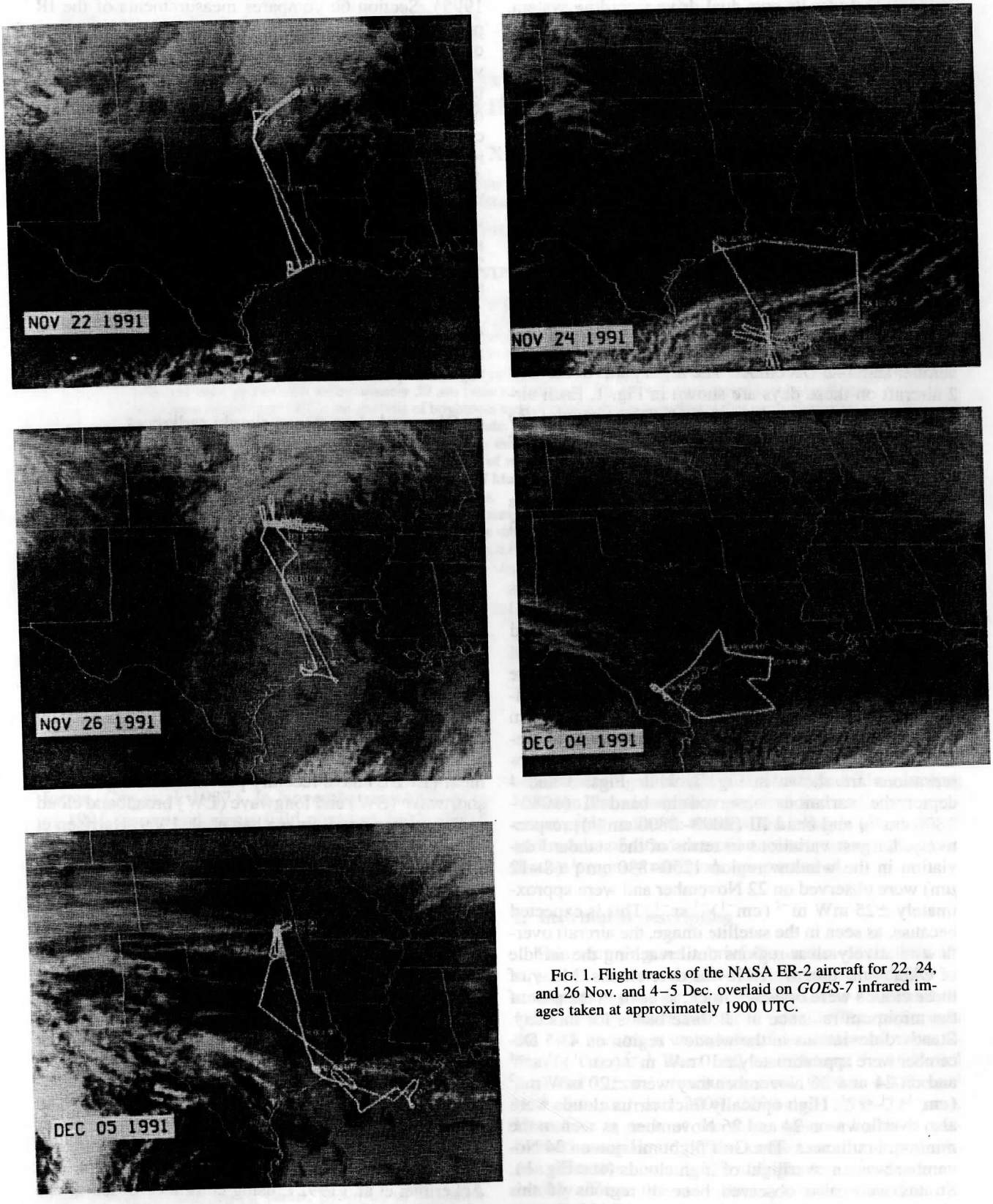

FIG. 1. Flight tracks of the NASA ER-2 aircraft for 22, 24, and 26 Nov. and 4–5 Dec. overlaid on *GOES-7* infrared images taken at approximately 1900 UTC.

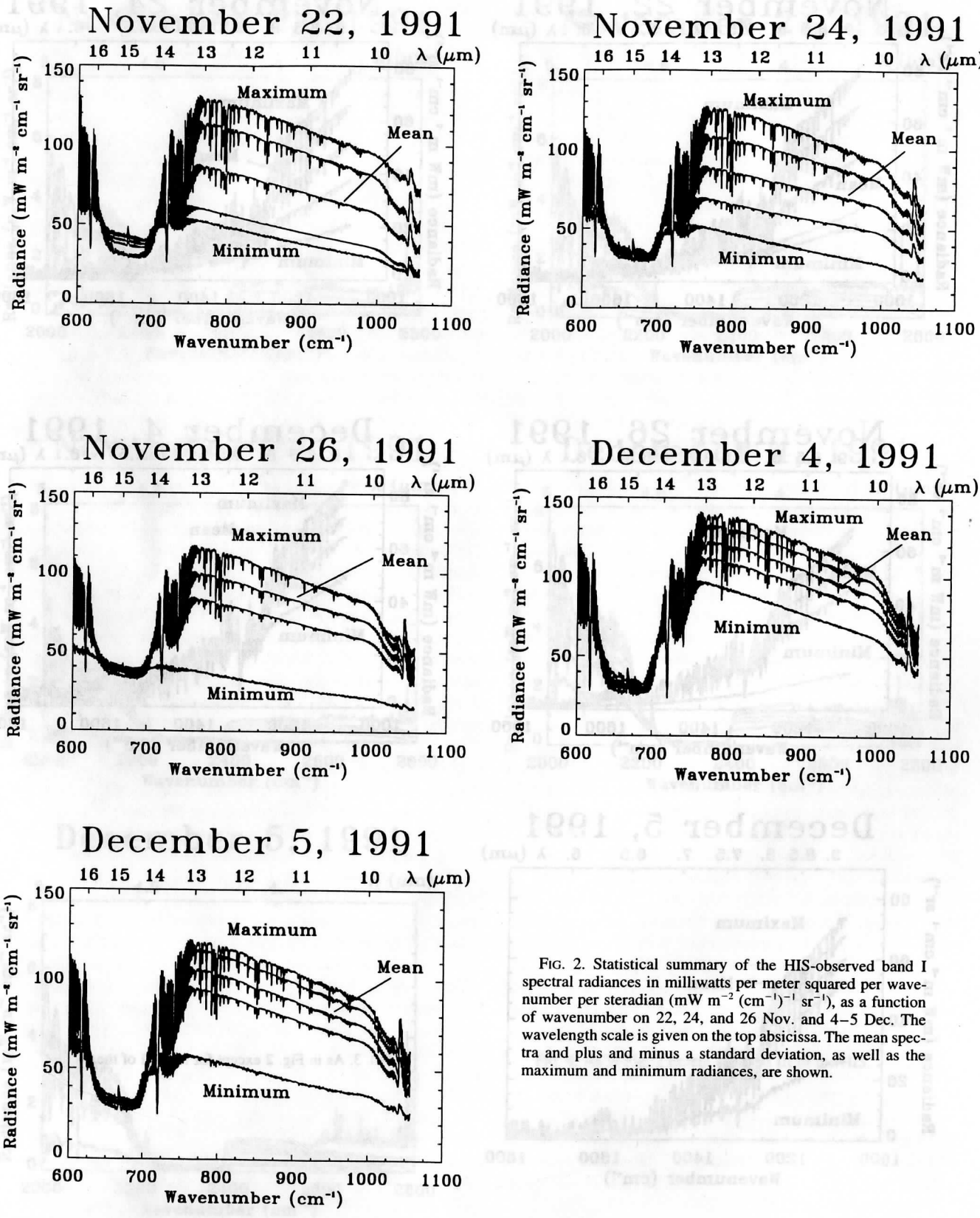

FIG. 2. Statistical summary of the HIS-observed band I spectral radiances in milliwatts per meter squared per wavenumber per steradian (mW m^{-2} $(cm^{-1})^{-1}$ sr^{-1}), as a function of wavenumber on 22, 24, and 26 Nov. and 4–5 Dec. The wavelength scale is given on the top absicissa. The mean spectra and plus and minus a standard deviation, as well as the maximum and minimum radiances, are shown.

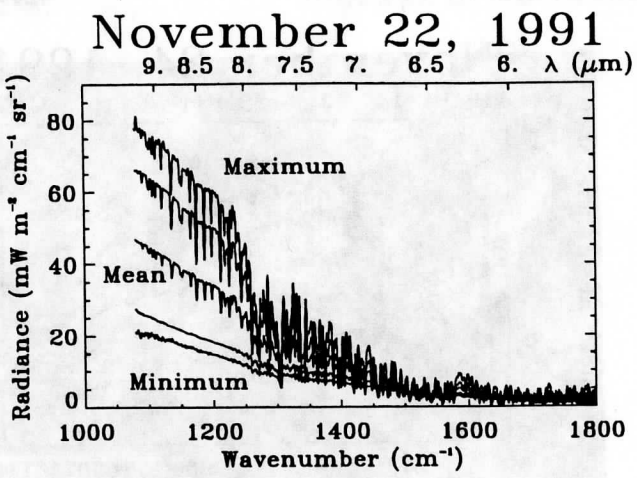

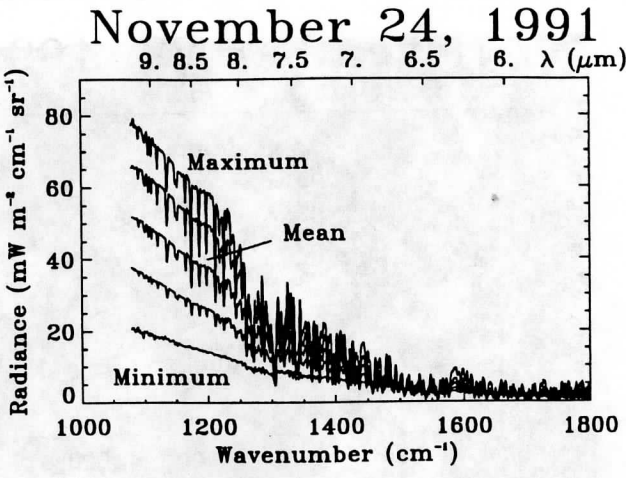

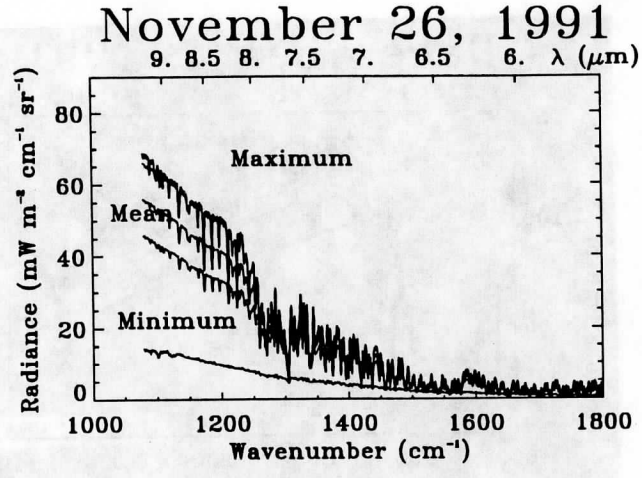

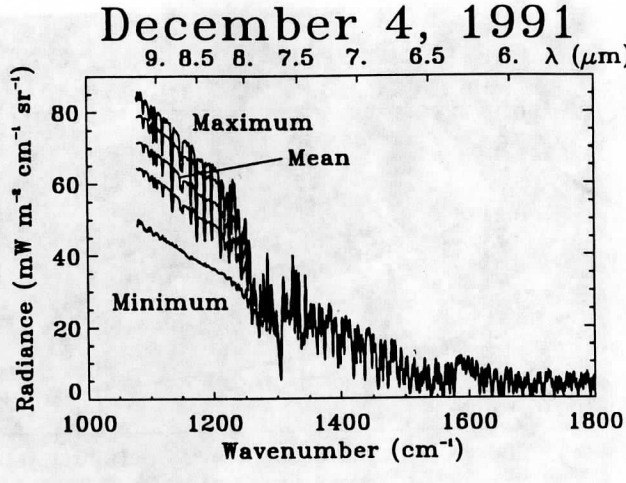

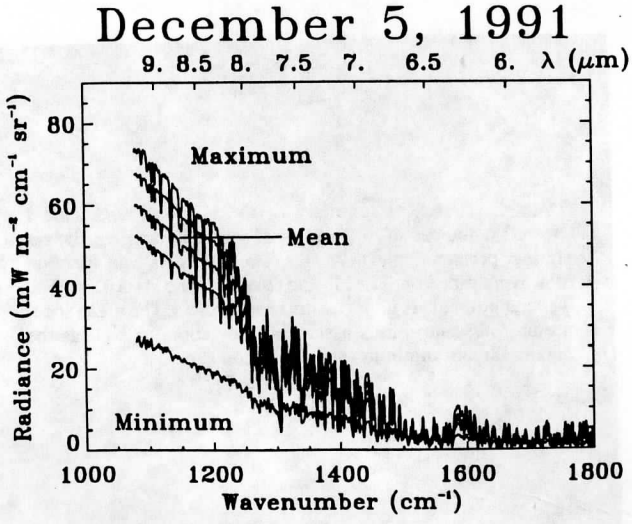

FIG. 3. As in Fig. 2 except for band II of the HIS.

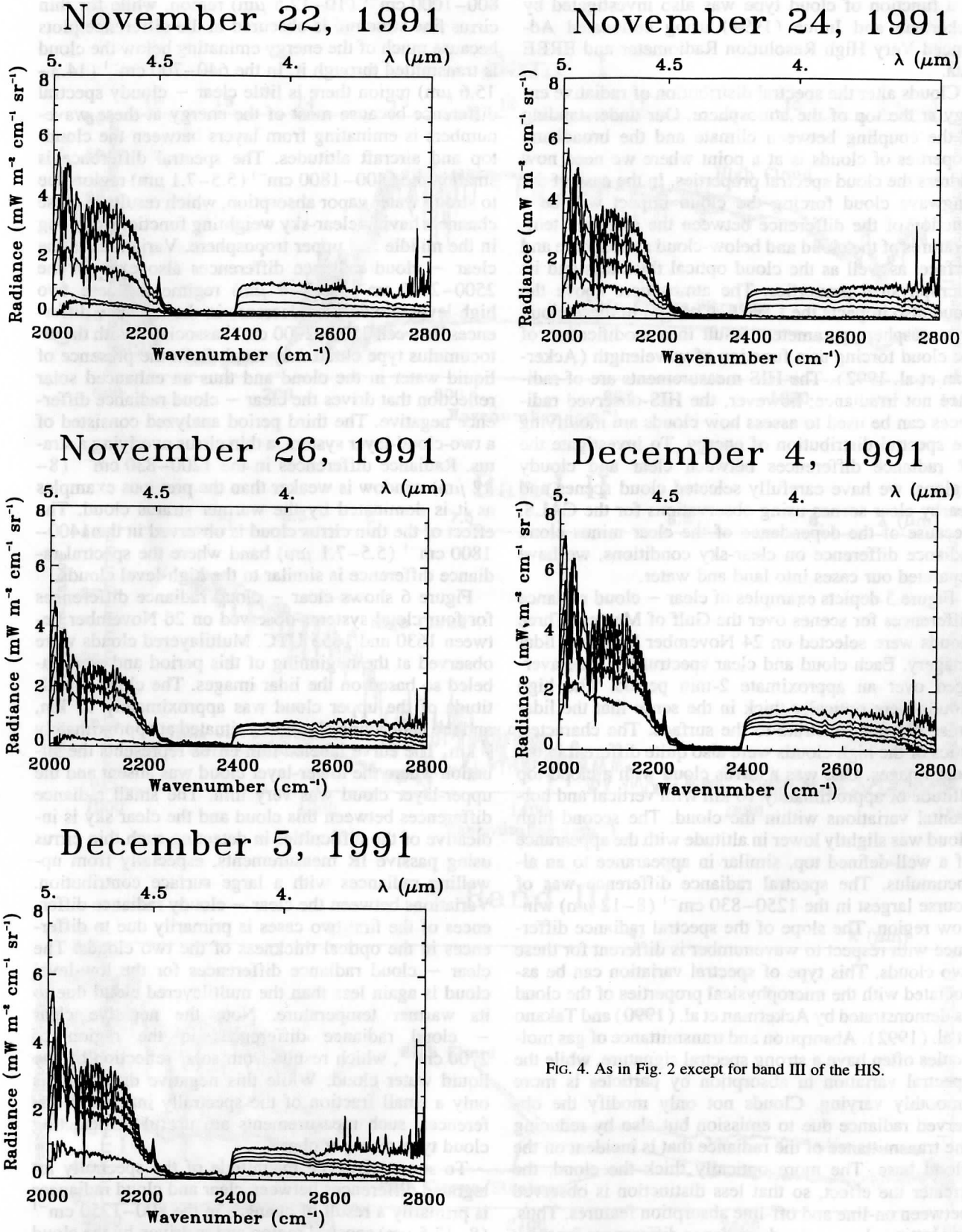

FIG. 4. As in Fig. 2 except for band III of the HIS.

as a function of cloud type was also investigated by Ackerman and Inoue (1994) using collocated Advanced Very High Resolution Radiometer and ERBE data.

Clouds alter the spectral distribution of radiative energy at the top of the atmosphere. Our understanding of the coupling between climate and the broadband properties of clouds is at a point where we need now address the cloud spectral properties. In the case of the longwave cloud forcing the cloud impact will be a function of the difference between the effective temperatures of the cloud and below-cloud atmosphere and surface, as well as the cloud optical thickness and its microphysical properties. The atmosphere above the cloud also impacts the LWCF. Changes in these cloud or atmosphere parameters result in a modification of the cloud forcing as a function of wavelength (Ackerman et al. 1992). The HIS measurements are of radiance not irradiance; however, the HIS-observed radiances can be used to assess how clouds are modifying the spectral distribution of energy. To investigate the IR radiance differences between clear and cloudy regions, we have carefully selected cloud scenes and nearby clear scenes using observations for the CALS. Because of the dependence of the clear minus cloud radiance difference on clear-sky conditions, we have separated our cases into land and water.

Figure 5 depicts examples of clear − cloud radiance differences for scenes over the Gulf of Mexico. Three clouds were selected on 24 November based on lidar imagery. Each cloud and clear spectrum is time averaged over an approximate 2-min period. The high clouds were optically thick in the sense that the lidar pulse did not penetrate to the surface. The characteristics of the high clouds were also quite different in the lidar images. One was a cirrus cloud with a cloud-top altitude of approximately 10 km with vertical and horizontal variations within the cloud. The second high cloud was slightly lower in altitude with the appearance of a well-defined top, similar in appearance to an altocumulus. The spectral radiance difference was of course largest in the 1250–830 cm^{-1} (8–12 μm) window region. The slope of the spectral radiance difference with respect to wavenumber is different for these two clouds. This type of spectral variation can be associated with the microphysical properties of the cloud as demonstrated by Ackerman et al. (1990) and Takano et al. (1992). Absorption and transmittance of gas molecules often have a strong spectral signature, while the spectral variation in absorption by particles is more smoothly varying. Clouds not only modify the observed radiance due to emission but also by reducing the transmittance of the radiance that is incident on the cloud base. The more optically thick the cloud, the greater the effect, so that less distinction is observed between on-line and off-line absorption features. Thus, in plotting clear − cloudy radiance differences for thick cirrus clouds one observes spectral structure in the 800–1000 cm^{-1} (10–12.5 μm) region, while for thin cirrus line structure is obscured in the difference plots because much of the energy eminating below the cloud is transmitted through it. In the 640–700 cm^{-1} (14.3–15.6 μm) region there is little clear − cloudy spectral difference because most of the energy at these wavenumbers is eminating from layers between the cloud-top and aircraft altitudes. The spectral difference is small in the 1400–1800 cm^{-1} (5.5–7.1 μm) region due to strong water vapor absorption, which results in these channels having clear-sky weighting functions peaking in the middle and upper troposphere. Variations in the clear − cloud radiance differences also exist in the 2500–2700 cm^{-1} (3.7–4 μm) regime in these two high-level clouds. The decrease in the radiance differences between 2500–2700 cm^{-1} associated with the altocumulus type cloud may result from the presence of liquid water in the cloud and thus an enhanced solar reflection that drives the clear − cloud radiance difference negative. The third period analyzed consisted of a two-cloud-layer system, a thin cirrus overlying a stratus. Radiance differences in the 1200–830 cm^{-1} (8–12 μm) window is weaker than the previous examples as it is dominated by the warmer stratus cloud. The effect of the thin cirrus cloud is observed in the 1400–1800 cm^{-1} (5.5–7.1 μm) band where the spectral radiance difference is similar to the high-level clouds.

Figure 6 shows clear − cloud radiance differences for four cloud systems observed on 26 November between 1630 and 1655 UTC. Multilayered clouds were observed at the beginning of this period and were labeled so based on the lidar images. The cloud-top altitude of the upper cloud was approximately 11 km, and the underlying cloud was situated at approximately 7 km. The curve labeled thin cirrus represents the situation where the lower-layer cloud was absent and the upper-layer cloud was very thin. The small radiance differences between this cloud and the clear sky is indicative of the difficulties in detecting such thin cirrus using passive IR measurements, especially from upwelling radiances with a large surface contribution. Variations between the clear − cloudy radiance differences of the first two cases is primarily due to differences in the optical thickness of the two clouds. The clear − cloud radiance differences for the low-level cloud is again less than the multilayered cloud due to its warmer temperature. Note the negative clear − cloud radiance differences in the region of 2700 cm^{-1}, which results from solar reflection by the liquid water cloud. While this negative difference is only a small fraction of the spectrally integrated differences, such measurements are useful in detecting cloud type or water phase.

To summarize, the magnitude of the spectrally integrated differences between clear and cloud radiances is primarily a result of changes in the 800–1250 cm^{-1} (8–12.5 μm) spectral region and is driven by the cloud optical thickness and the difference between the cloud

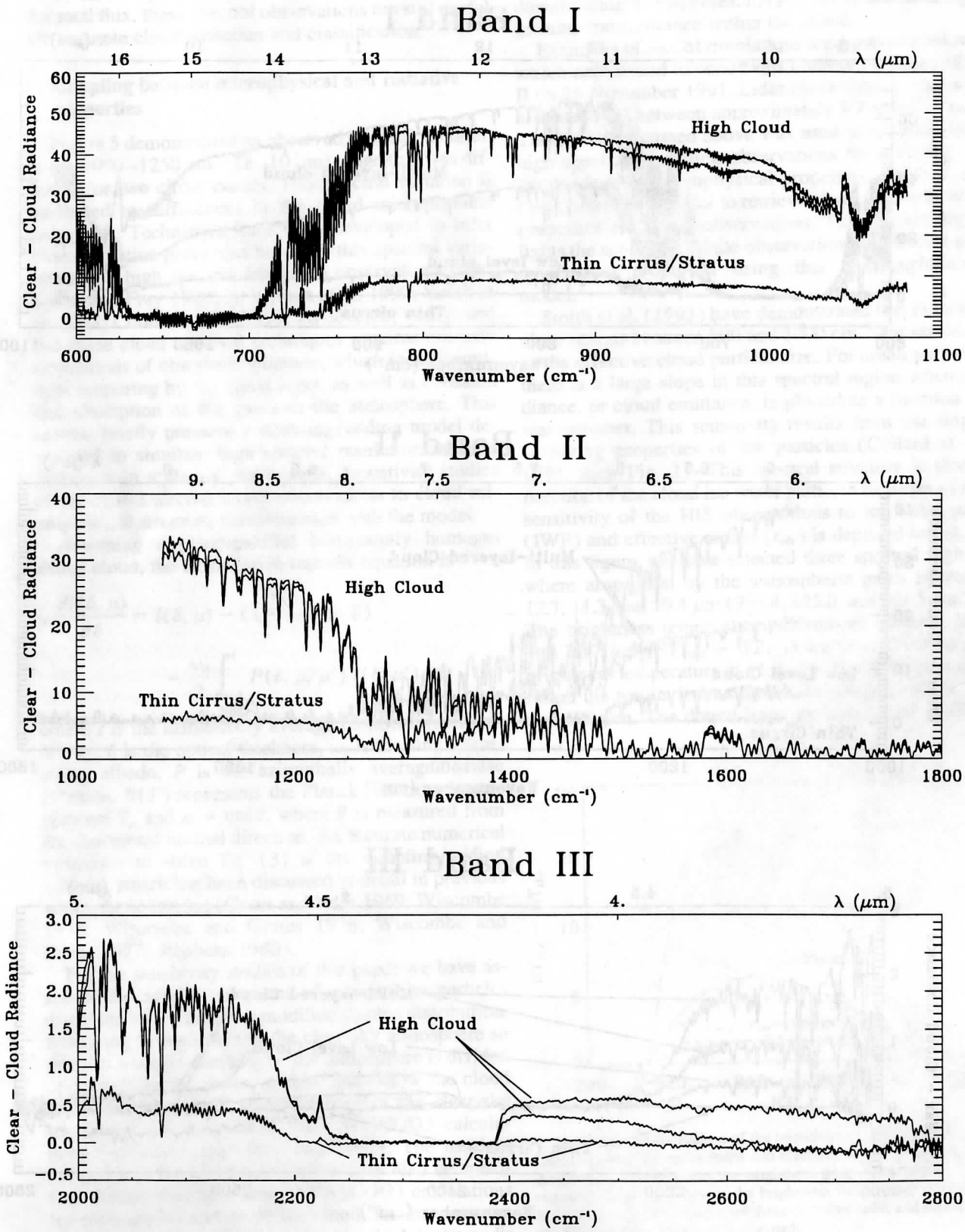

FIG. 5. Clear minus cloud radiances [mW m^{-2} $(cm^{-1})^{-1}$ sr^{-1}] observed for clouds observed on 24 Nov.

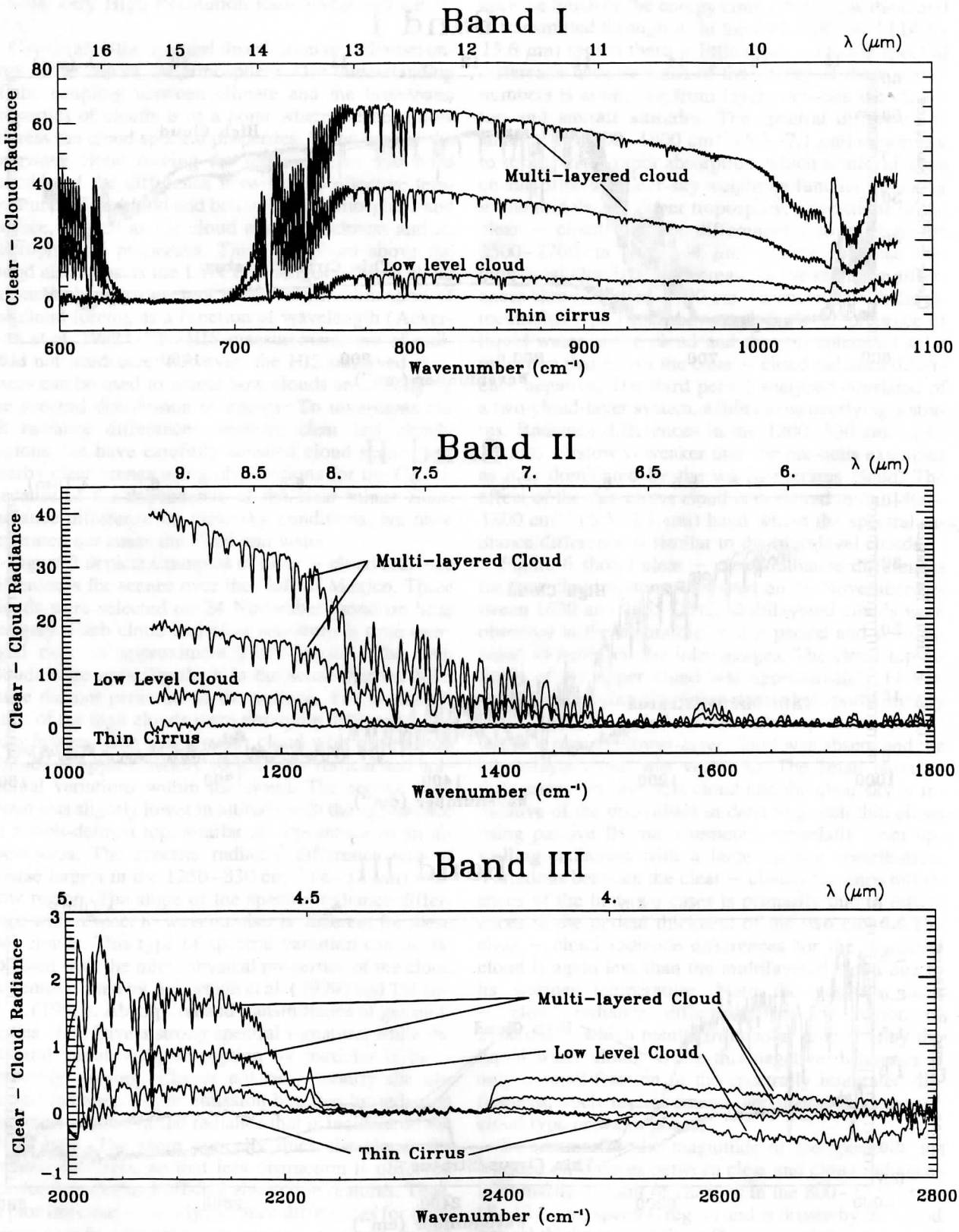

FIG. 6. Clear minus cloud radiances [mW m^{-2} $(cm^{-1})^{-1}$ sr^{-1}] observed for clouds observed on 26 Nov.

and the surface temperature. It is important to note that, while certain spectral regions contribute little energy to the total flux, these spectral observations are still useful for accurate cloud detection and classification.

5. Coupling between microphysical and radiative properties

Figure 5 demonstrated an observed spectral variation in the 1000–1250 cm^{-1} (8–10 μm) range that was different for two cirrus clouds. This spectral variation is attributed to differences in the cloud microphysical properties. Techniques have been developed to infer cloud radiative properties based on this spectral variation using high spectral resolution observations (e.g., Smith and Frey 1990; Ackerman et al. 1990; Smith et al. 1993; Collard et al. 1995). To develop, verify, and test these cloud retrieval techniques requires accurate simulations of observed radiances, which include multiple scattering by the cloud layer, as well as emission and absorption of the gases in the atmosphere. This section briefly presents a doubling/adding model developed to simulate high spectral resolution infrared radiances in a cloudy atmosphere. Sensitivity studies of HIS ER-2 aircraft-based observations to cloud microphysical structure are conducted with the model.

Assuming a plane-parallel horizontally homogeneous cloud, the IR radiative transfer equation is

$$\mu \frac{dI(\delta, \mu)}{d\delta} = I(\delta, \mu) - (1 - \omega_0) B(T) - \frac{\omega_0}{2} \int_{-1}^{1} P(\delta, \mu, \mu') I(\delta, \mu') d\mu, \quad (3)$$

where I is the azimuthally average monochromatic intensity, δ is the optical thickness, ω_0 is the single scattering albedo, P is the azimuthally averaged phase function, $B(T)$ represents the Planck function at temperature T, and $\mu = \cos\theta$, where θ is measured from the downward normal direction. An accurate numerical technique to solve Eq. (3) is the doubling/adding method, which has been discussed in detail in previous atmospheric studies (Grant and Hunt 1969; Wiscombe 1976; Wiscombe and Grams 1976; Wiscombe and Evans 1977; Stephens 1980).

For the sensitivity studies of this paper we have assumed the cloud is composed of spherical ice particles distributed according to a modified gamma distribution. Scattering is negligible in the clear-sky atmosphere so that, for a single cloud layer, the atmosphere is divided into three layers: above, within, and below the cloud layer. Radiances and transmittances in the clear-sky conditions are determined from FASCOD3 calculations (Anderson and Chetwynd 1992). The incident radiances at the cloud boundaries must also be specified. Rather than run separate FASCOD3 calculations for each angle incident on the cloud, for the purposes of this paper, FASCOD3 is used to calculate the nadir and zenith angle radiances, and the radiation field is then assumed to be isotropic for the uplooking and downlooking hemispheres. FASCOD3 is used to assign gaseous transmittance within the cloud.

Examples of model simulations are presented below, which correspond to conditions observed during FIRE II on 26 November 1991. Lidar observations indicated a cirrus cloud between approximately 8.7 and 10.5 km. The model discussed above was used to simulate HIS high spectral resolution observations for a variety of assumed cloud microphysical properties. Smith et al. (1993) used this model to retrieve cloud microphysical properties from HIS observations. This section highlights the sensitivity of the observations to different microphysical properties using this doubling/adding model.

Smith et al. (1993) have demonstrated that radiance observations between 800 and 1000 cm^{-1} are sensitive to the effective cloud particle size. For small particles there is a large slope in this spectral region when radiance, or cloud emittance, is plotted as a function of wavenumber. This sensitivity results from the single scattering properties of the particles (Collard et al. 1994, their Fig. 2). This spectral structure is also a function of the cloud ice water path. An example of the sensitivity of the HIS observations to ice water path (IWP) and effective radius (r_{eff}) is depicted in Fig. 7. In this figure we have selected three spectral regions where absorption by the atmospheric gases is weak: 12.7, 11.3, and 10.4 μm (787.4, 885.0, and 961.5 cm^{-1}). The brightness temperature differences between 10.4 and 12.7 μm ($BT_{10.4} - BT_{12.7}$) are plotted versus the brightness temperature at 11.3 μm. The solid lines represent the results from simulations using r_{eff} of 10, 25, and 100 μm. The dotted lines are lines of equal IWP.

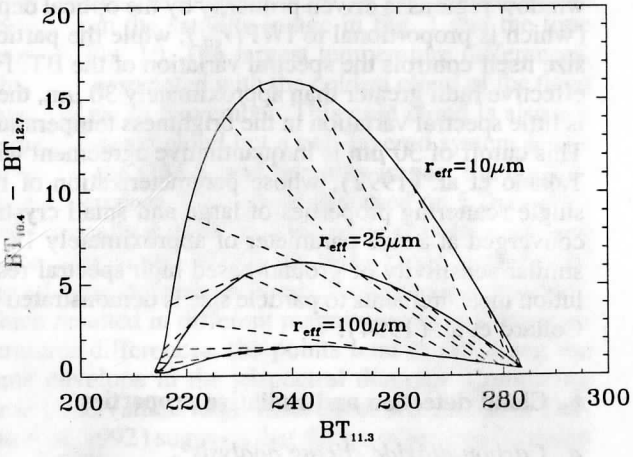

FIG. 7. Model simulations of the sensitivity of HIS observations to different cloud ice water paths and effective radii. The sensitivity is displayed as a function of the brightness temperature difference between 10.4 and 12.7 μm vs the brightness temperature at 11.3 μm. Solid lines represent results for three effective radii, and dotted lines are lines of equal cloud ice water path.

For clear regions, $BT_{10.4} - BT_{12.7}$ is nearly zero, and $BT_{11.3} = 283$ K. For cloud, regardless of particle size, as the IWP gets very large, $BT_{10.4} - BT_{12.7} \approx 0$ K, and $BT_{11.3} \approx 214$ K. For large particles, $r_{eff} = 100$ μm, $BT_{10.4} - BT_{12.7}$ is small, regardless of the IWP. This large particle difference is a result of the combination of the radiances from the cloud and surface and the fact that the Planck radiance is a nonlinear function of temperature. Large brightness temperature differences (e.g., greater than 5 K) can be generated only if the particles are small and the IWP moderate. The maximum $BT_{10.4} - BT_{12.7}$ occurs at an optical depth of approximately 1.

The spectral region most sensitive to the particle size distribution ($\Delta BT > 5$ K) is the 950–1050 cm^{-1} (9.5–10.5 μm) region. The sensitivity of ΔBT to particle size was exploited by Ackerman et al. (1990) and Smith et al. (1993) using FIRE I results. The ΔBT is also a function of particle shape as demonstrated by Ackerman and Smith (1990) for observations at approximately 8, 11, and 12 μm. Takano et al. (1992) undertook a more detailed sensitivity study of the effects of small ice crystals and their shape on cirrus cloud properties at 8.35, 11.16, and 12.6 μm. They independently verified that the presence of small ice crystals can produce significant ΔBT between these three wavelengths. They also demonstrated that a nonspherical model (spheroid and hexagons) for ice crystal single scattering properties gave a better representation of the HIS observations than the ice sphere model. The theoretical simulation of Ackerman and Smith (1990) and Takano et al. (1992) indicate that particle habit influences the slope of the brightness temperature difference between 11 and 12 μm ($BT_{11} - BT_{12}$) versus the difference between 8 and 11 μm ($BT_8 - BT_{11}$).

The magnitude of the brightness temperature in the window regions is driven primarily by the optical depth (which is proportional to IWP/r_{eff}), while the particle size itself controls the spectral variation of the BT. For effective radii greater than approximately 30 μm, there is little spectral variation in the brightness temperature. This cutoff of 30 μm is in quantitative agreement with Takano et al. (1992), whose parameterization of the single scattering properties of large and small crystals converged at a size parameter of approximately 18. A similar sensitivity of ground-based high spectral resolution measurements to particle size is demonstrated by Collard et al. (1994).

6. Cloud detection and radiative properties

a. Carbon dioxide slicing analysis

The CO_2 slicing method (Smith et al. 1974, Smith and Platt 1978; Menzel et al. 1983) is an accurate technique for inferring cloud altitude. The high spectral resolution of the HIS in the 700–900 cm^{-1} (11.1–14.3 μm) region is ideal for CO_2 applications. Smith and Frey (1990) used the CO_2 slicing technique to determine cloud-top pressures from HIS data. The improved spectral resolution of the HIS over the narrow bandpass filters of present-day satellite instruments results in greatly increased accuracy in derived cloud pressure altitude.

The CO_2 slicing method derives an effective cloud pressure from

$$\frac{I_1(\nu) - I_2(\nu)}{I_1(\nu_0) - I_2(\nu_0)} = \frac{\int_{p_c}^{p_s} \tau(\nu, p) \frac{\partial B(\nu, T(p))}{\partial \ln p} dp}{\int_{p_c}^{p_s} \tau(\nu_0, p) \frac{\partial B(\nu_0, T(p))}{\partial \ln p} dp} = C(p_c), \quad (4)$$

where I is an observed spectral radiance at wavenumber ν and subscripts 1 and 2 refer to different fields of view and, in practice, a cloudy scene and a clear-sky scene is chosen. The subscript 0 refers to a reference wavenumber; B is the Planck radiance corresponding to the temperature T, p is pressure, p_s is the surface pressure, and τ is the atmospheric transmittance between the instrument and the pressure p; p_c is the cloud-top pressure determined by minimizing the difference between the left-hand side and the right-hand side of the equation. In deriving this relation, it is approximated that the cloud radiates as a greybody in this spectral region and that the cloud is infinitesimally thin.

Figure 8 shows examples of the retrieved cloud pressure altitude using the CO_2 slicing method for the period 1901–1911 UTC 5 December. The two lines are the retrieved cloud altitude and the IR window equivalent blackbody temperature. Dotted lines indicate the HIS in its calibration mode or, in the case of cloud pressure altitude, no cloud height retrieval (e.g., clear sky). The HIS time series overlays the CALS lidar image. While the CO_2 slicing method is detecting the presence of the cloud, its effective altitude varies more than the lidar-observed cloud, and its altitude is less than the lidar-observed cloud top (Wylie and Menzel 1989). The CO_2 slicing method is a passive radiometric retrieval of cloud altitude and is dependent on the cloud optical depth and its vertical distribution as well as the surface emission. Thus, the radiation measured by the HIS is a combination of emission through the depth of the cloud, transmitted energy from below, and emission from above the cloud top. The CO_2 slicing, and other passive cloud altitude detection techniques, assume the cloud-layer emission results from some effective level within the cloud. The pressure of this effective level is dependent on the vertical distribution of the optical depth within the cloud.

b. Brightness temperature difference analysis

A method of detecting clouds using observations near 8.3, 11, and 12 μm was proposed by Ackerman et

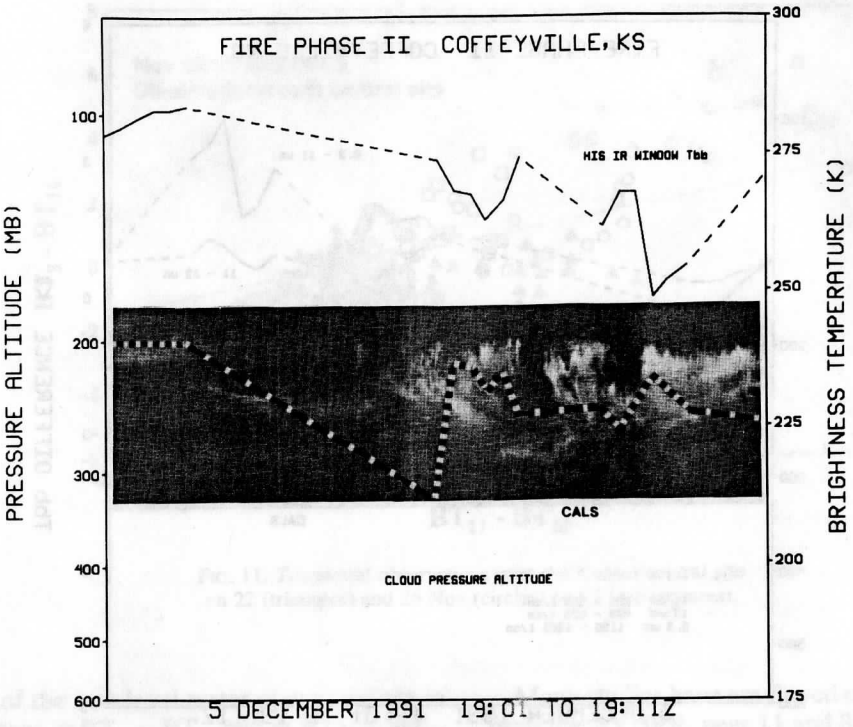

FIG. 8. Retrieved cloud pressure altitude using the CO_2 slicing method for the period 1901–1911 UTC 5 Dec. The black and white line is the retrieved cloud altitude in mb (left scale), and the dark line is the IR window equivalent blackbody temperature (right scale). Dashed lines indicate the HIS in its calibration mode or no cloud height retrieval. The HIS time series is overlaid on the CALS lidar image.

al. (1990) and extended by Strabala et al. (1994). Figure 9 depicts the trispectral approach to detecting cirrus cloud for the same periods as Fig. 8. The 8.3-μm bandpass (1190–1205 cm^{-1}) includes a water vapor absorption line, while the 11-μm (889–904 cm^{-1}) and 12-μm (829–838 cm^{-1}) bandpasses lie between water vapor absorption lines. For clear-sky conditions the 8.3–11.1 μm brightness temperature differences ($BT_{8.3} - BT_{11}$) are negative owing to differences in atmospheric water vapor absorption. Positive $BT_{8.3} - BT_{11}$ are indicative of cirrus cloud. Because of the narrow bandpasses chosen in the present study, the 11–12 μm differences ($BT_{11} - BT_{12}$) may be positive or negative depending on the surface emittance, atmospheric water vapor, and the existence of a cloud. For wider bandpasses, such as that of the AVHRR, the $BT_{11} - BT_{12}$ is generally positive. The presence of cirrus clouds drives the $BT_{11} - BT_{12}$ toward zero. The trispectral method, as well as other infrared window techniques, should account for the variation of surface emissivity with wavelength, particularly over bare soils (e.g., deserts).

To minimize the effects of surface emissivity, we have analyzed observations over the same geographic region: the central site. A time series of the 11-μm brightness temperature for these days in which the ER-2 was in the vicinity is shown in Fig. 10. Figure 11 depicts the trispectral analysis for observations made over the central site on 22 November (triangles), 26 November (circles), and 5 December (squares). Large temperature brightness differences indicate the presence of particles less than 30 μm (Takano et al. 1992). The greatest separation between clear and cloudy sky in the trispectral diagram is on 22 November, as expected from the satellite image in Fig. 1 and the time series of Fig. 10. The largest temperature differences, which are associated with the coldest cloud of the three days, are on 26 November. This cold cloud is also not a single-layered cloud but a two-layered system as observed by the CALS, and this may impact the temperature differences. The clouds observed on 5 December were optically thinner than the other two days, as seen in the time series. While the three cloud systems observed were different in their macrophysical structure, which resulted in different magnitudes in spectral temperatures differences, the points tend to fall along the same envelope in the trispectral diagram. Comparing these observations with theoretical simulations (Takano et al. 1992) suggests that the particle size and shape were similar on these three days, at least from a radiative perspective.

We next consider cirrus clouds observed over the Gulf of Mexico on 24 November and 4 December. Observations were limited to being over water. Further

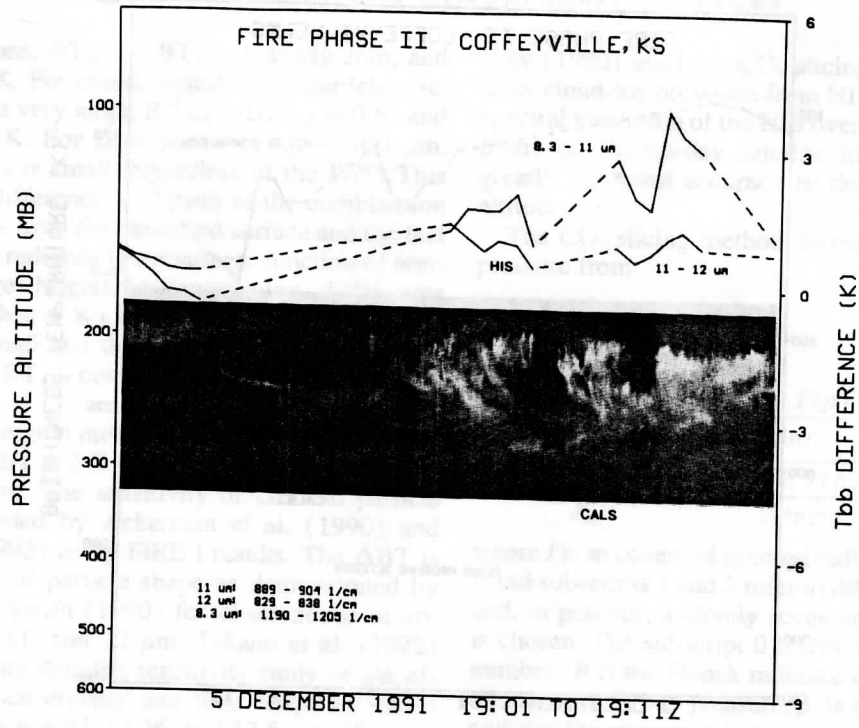

FIG. 9. Brightness temperature differences between 11 and 12 μm and 8.3 and 11 μm for the period 1901–1911 UTC 5 Dec. Cloud altitude is given on the left scale, and the brightness temperature difference on the right axis scale. The HIS-observed brightness temperature differences are overlaid on the CALS lidar image.

restrictions were placed on 24 November (1945–2000 UTC) so that a single-layered cloud, as indicated by lidar, could be examined. This cloud gave the appearance of an altocumulus cloud. Figure 12 is the trispectral diagram for these observations where 24 November observations are denoted by the asterisks and 4 December by the filled circles. Clear skies on 4 December have $BT_8 - BT_{11} < -3$ K and $BT_{11} - BT_{12}$ of ~ 0 K.

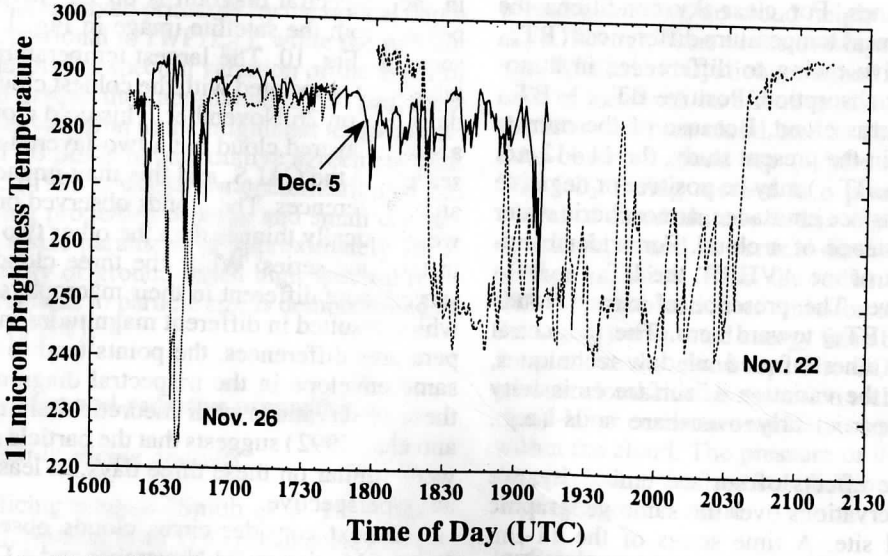

FIG. 10. The 11-μm brightness temperature time series for occasions when the ER-2 aircraft was in the vicinity of the central site: 22 (dashed line) and 26 Nov (dotted) and 5 Dec (solid line).

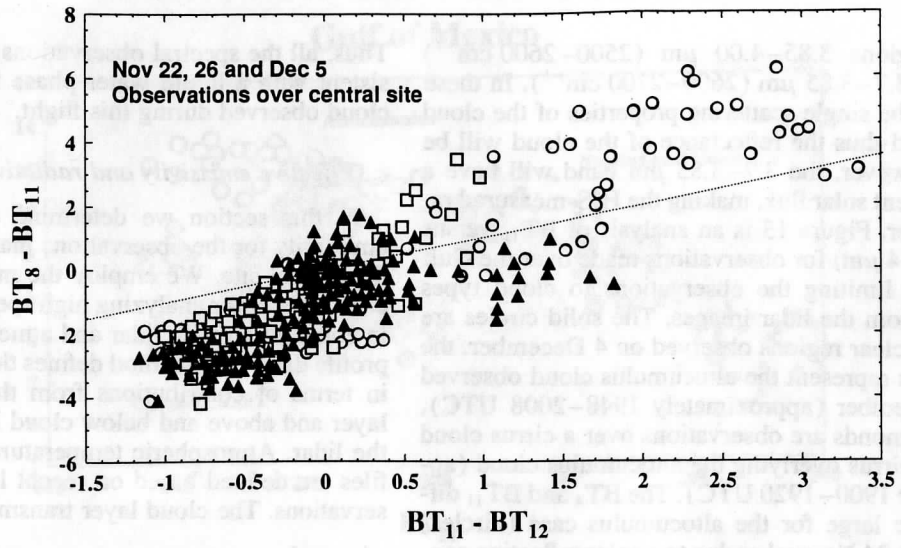

FIG. 11. Trispectral observations over the Kansas central site on 22 (triangles) and 26 Nov (circles) and 5 Dec (squares).

The presence of the low-level water cloud tends to increase differences in $BT_8 - BT_{11}$ and in $BT_{11} - BT_{12}$. Comparing the 24 November observations to the cirrus over the central site, the high cloud on 24 November has a different BT difference slope. The slope for the brightness temperature differences on 24 November tend to be in line with the envelope of the water cloud observations of 4 December, suggesting that the 24 November cloud is a water cloud. The spectral radiance differences in the 2500–2800 cm^{-1} (Fig. 6) region also suggests that the cloud observed on 24 November consists of liquid water.

Many studies have employed observations, primarily from the AVHRR, near 11 and 3.7 μm to detect clouds and infer their optical depth, effective radius, and phase (e.g., Hunt 1973; Arking and Childs 1985; Stone et al. 1990; d'Entremont 1986; Huang and Liou 1984; Ou et al. 1993; Baum et al. 1994). Measurement by these channels are affected relatively little by the presence of water vapor. Most of the techniques are applied during the night, to avoid contamination of the 3.7-μm radiance by reflection of solar radiation. We take advantage of this solar reflection with the high spectral measurements by splitting this atmospheric window into two

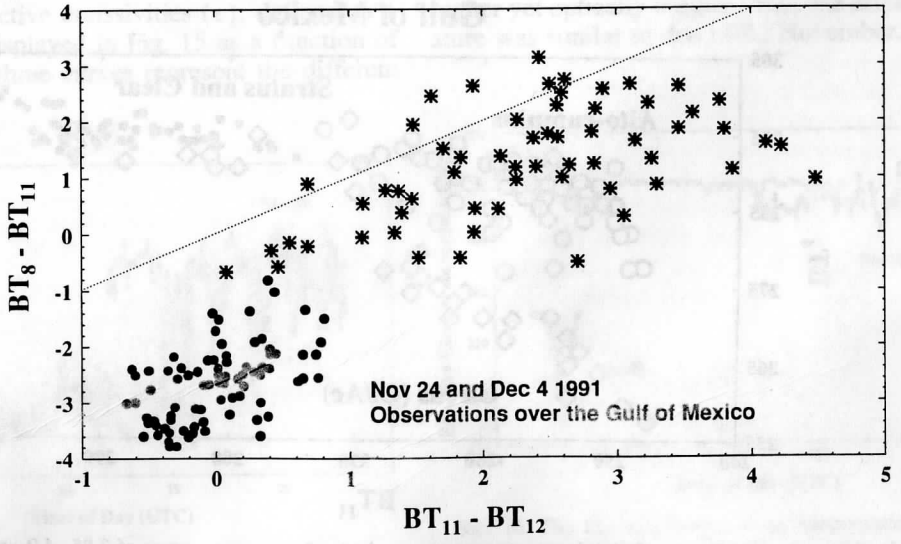

FIG. 12. Trispectral observations over the Gulf of Mexico on 24 Nov (asterisks) and 4 Dec (filled circles).

spectral regions 3.85–4.00 μm (2500–2600 cm^{-1}) (BT_4) and 3.7–3.85 μm (2600–2700 cm^{-1}). In these two bands the single scattering properties of the cloud particles and thus the reflectance of the cloud will be similar; however, the 3.7–3.85 μm band will have a larger incident solar flux, making the HIS-measured radiance larger. Figure 13 is an analysis of BT_{11} versus BT_4 (3.85–4 μm) for observations made over the Gulf of Mexico, limiting the observations to cloud types identified from the lidar images. The solid circles are stratus and clear regions observed on 4 December, the open circles represent the altocumulus cloud observed on 24 November (approximately 1948–2008 UTC), and the diamonds are observations over a cirrus cloud alone or a cirrus overlying the altocumulus cloud (approximately 1900–1920 UTC). The BT_4 and BT_{11} differences are large for the altocumulus case (circles) observed on 24 November due to a solar reflection contribution to BT_4. The BT_4 and BT_{11} relationship for cirrus cloud observations (diamonds) results from the nonlinear relation between radiance and temperature between the two wavelengths (i.e., Planck function), the temperature difference between the surface and cloud, and differences in cloud spectral emittance. Returning to the phase of the altocumulus cloud, we consider the 3.7–3.85 μm (2600–2700 cm^{-1}) interval where solar reflectance by the water cloud should increase the brightness temperature difference between $BT_{3.7}$ and BT_4. This is demonstrated in Fig. 14, which depicts BT_{11} versus $BT_{3.7} - BT_4$ during the same time periods as Fig. 13. The cirrus ice clouds separate from the water clouds on this diagram, except when the altocumulus is underlying the thin cirrus, because of the differences between ice and water refraction index. Thus, all the spectral observations are physically consistent with a liquid water phase for the altocumulus cloud observed during this flight.

c. *Effective emissivity and radiative temperature*

In this section we determine the effective cloud emissivity for the observations made in the vicinity of the central site. We employ the method of Ackerman et al. (1990) for analyzing high spectral resolution data in conjunction with lidar and atmospheric temperature profile data. This method defines the observed radiance in terms of contributions from three layers: a cloud layer and above and below cloud layers as defined by the lidar. Atmospheric temperature and moisture profiles are defined based on recent local radiosonde observations. The cloud layer transmittance is defined as

$$\tau(z_T, z_B) = \left[\frac{I(z_A) - \int_{z_T}^{z_A} B[T(z)] \frac{d\tau(z_T, z)}{dz} dz}{\tau(z_A, z_T)} - \bar{B}_c \right] \times [I(z_B) - \bar{B}_c]^{-1}, \quad (5)$$

where the subscripts T, B, and A represent altitudes at cloud top, cloud base, and the ER-2, respectively, and I is the radiance. Above-cloud radiances

$$\left(\int_{z_T}^{z_A} B[T(z)] \frac{d\tau(z_T, z)}{dz} dz \right)$$

and gaseous transmittances within and above the cloud, $\tau(z_A, z_T)$, are determined from FASCOD3 calculations.

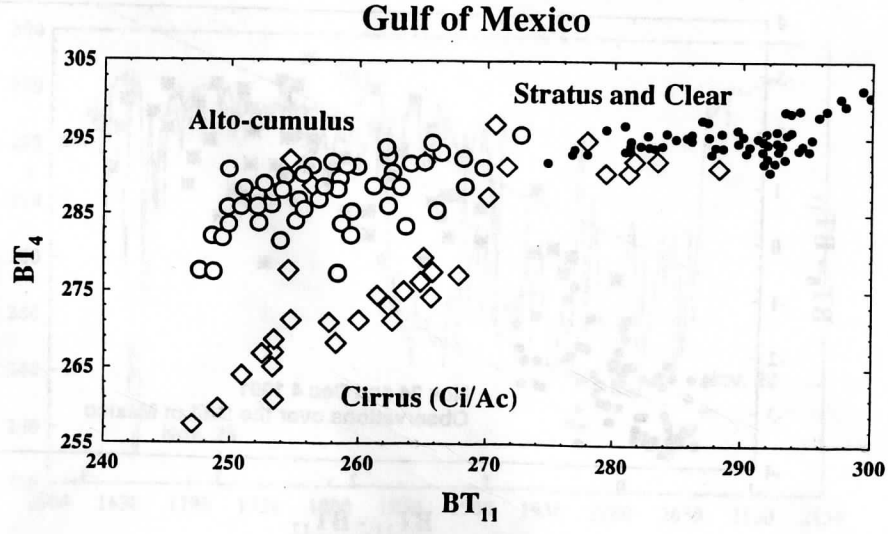

FIG. 13. The 11-μm brightness temperature vs the brightness temperature of 3.85–4.0 μm for observations made over the Gulf of Mexico. The solid circles are stratus and clear regions, the open circles represent the altocumulus cloud, and the diamonds are observations over a cirrus cloud alone or a cirrus overlying the altocumulus cloud.

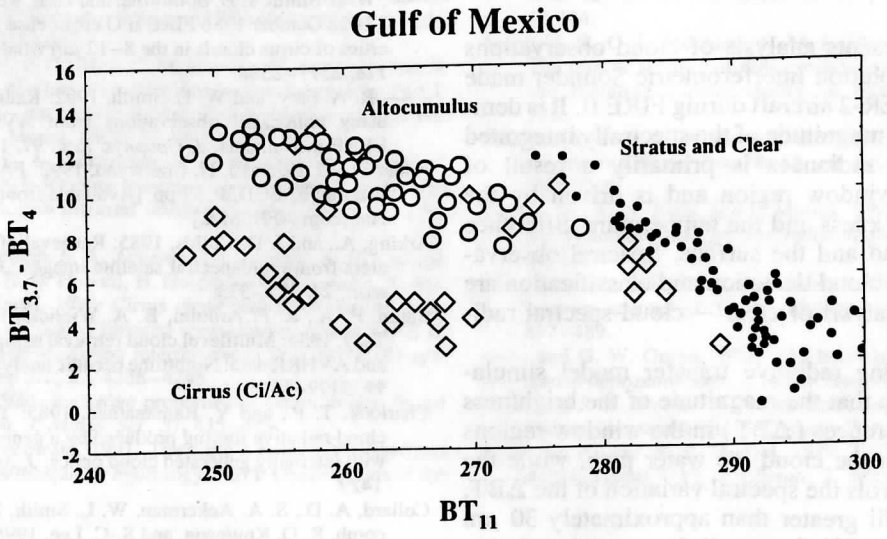

FIG. 14. Plot of BT_{11} versus $BT_{3.7} - BT_4$ for the same time periods as in Fig. 13.

Clear-sky HIS observations define the spectral radiance at the cloud base after subtracting the contribution from the above-cloud atmosphere. An initial spectral transmittance of the cloud is derived by first assuming a value of the cloud effective radiance ($\bar{B}_c$) corresponding to the Planck radiance evaluated with the midcloud temperature. The effective emissivities and effective cloud temperatures are solved using an iterative approach (Ackerman et al. 1990) to correct the effective emitting temperature of the cloud in accordance with the derived optical depth. For a cloud of constant geometric thickness, as the optical depth increases, the iterative method moves the effective temperature toward the cloud top and toward the cloud base as the cloud thins.

The 11-μm effective emissivities (ϵ), defined as $1 - \tau(z_T, z_B)$, are displayed in Fig. 15 as a function of time of day. The three curves represent the different days, with the points denoting time of the measurement. The solid line shows 5 December has very low emissivities, generally $\epsilon < 0.2$. The ϵ on 26 November (dotted line) reflect the passage of the ER-2 over the cirrus cloud overlying the altocumulus, which in the retrieval scheme is considered as one layer. November 22 (dashed line) has emissivities ranging between 0.2 and 0.85, with the most values greater than 0.5. None of the cloud emissivities are near unity; cirrus almost never radiate as a blackbody. The corresponding effective cloud temperatures are shown in Fig. 16. While the clouds observed on 5 December and 22 November had very different emissivities, the effective cloud temperature was similar, 226 K on the 5th and 225 K on the 22nd. The cirrus layer observed on 5 December was higher yet optically thinner; thus, the effective temperature was similar to that of 22 November.

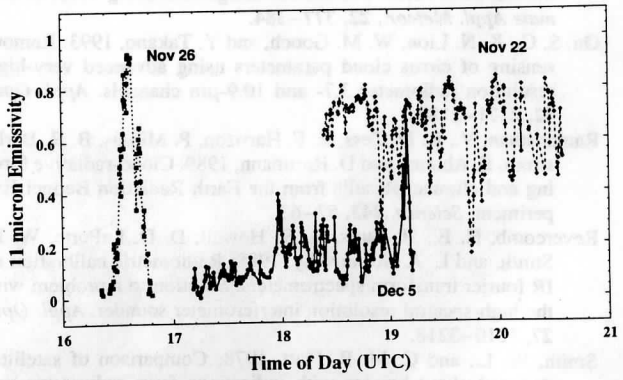

FIG. 15. The 11-μm emissivity time series for occasions when the ER-2 aircraft was overflying clouds and in the vicinity of the central site: 22 (dashed line) and 26 Nov (dotted) and 5 Dec (solid line).

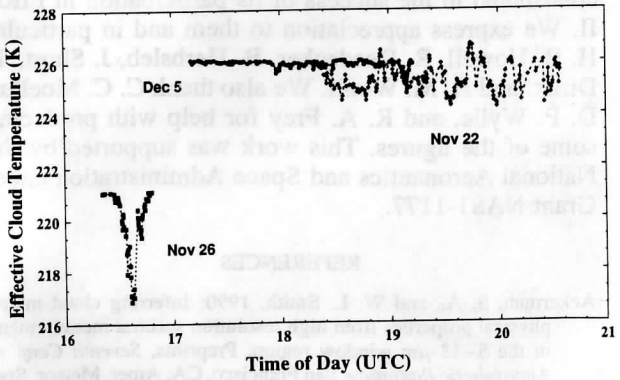

FIG. 16. The 11-μm effective cloud temperature time series for occasions when the ER-2 was overflying clouds and in the vicinity of the central site: 22 (dashed line) and 26 Nov (dotted) and 5 Dec (solid line).

7. Summary

This paper presents analysis of cloud observations by the High Resolution Interferometric Sounder made from the NASA ER-2 aircraft during FIRE II. It is demonstrated that the magnitude of the spectrally integrated clear and cloud radiances is primarily a result of changes in the window region and is driven by the cloud optical thickness and the temperature difference between the cloud and the surface. Spectral observations suitable for cloud detection and classification are evident in the analysis of clear − cloud spectral radiance differences.

Doubling/adding radiative transfer model simulations demonstrate that the magnitude of the brightness temperature differences (ΔBT) in the window regions are a function on the cloud ice water path, while the particle size controls the spectral variation of the ΔBT. For effective radii greater than approximately 30 μm (size parameter of 18) there is little spectral variation in the brightness temperature curve. An analysis of brightness temperature differences indicates that cirrus clouds over the central FIRE site were indicative of cloud with a small-particle mode. The cases analyzed had similar appearances in a plot of $BT_{11} - BT_{12}$ versus $BT_8 - BT_{11}$, suggesting similarity in the microphysical properties and demonstrating that the cirrus are not gray. Brightness temperature differences between 3.7, 4, 8, 11, and 12 were used to infer the phase of water of a high cloud over the Gulf of Mexico.

Cloud effective emissivities and effective radiative temperatures were derived for observations over the central site using complementary lidar and radiosonde data. Small variations in these effective properties were seen on 5 December and 22 November, and though they had similar effective temperatures, the emissivities were very different. None of the clouds observed had an emissivity close to one (i.e., radiated as a blackbody) nor could they be considered as greybodies.

Acknowledgments. There are many people who, at some point, assisted in the analysis of the HIS data or contributed to the success of its participation in FIRE II. We express appreciation to them and in particular H. B. Howell, R. Deedecker, B. Herbsleb, J. Short, T. Dirkx, and H. M. Woolf. We also thank C. C. Moeller, D. P. Wylie, and R. A. Frey for help with producing some of the figures. This work was supported by the National Aeronautics and Space Administration under Grant NAS1-1177.

REFERENCES

Ackerman, S. A., and W. L. Smith, 1990: Inferring cloud microphysical properties from high resolution spectral measurements in the 8–13 μm window region, Preprints, *Seventh Conf. on Atmospheric Radiation,* San Francisco, CA, Amer. Meteor. Soc., 6–8.

——, and T. Inoue, 1994: Radiation energy budget studies using collocated AVHRR and ERBE observations, *J. Appl. Meteor.,* **33,** 370–378.

——, W. L. Smith, J. D. Spinhirne, and H. E. Revercomb, 1990: The 27–28 October 1986 FIRE IFO cirrus case study: Spectral properties of cirrus clouds in the 8–12 μm window. *Mon. Wea. Rev.,* **118,** 2377–2388.

——, R. A. Frey, and W. L. Smith, 1992: Radiation budget studies using collocated observations from AVHRR, HIRS/2 and ERBE instruments. *J. Geophys. Res.,* **97,** 11 513–11 525.

Anderson, G. P., and J. H. Chetwynd, 1992: FASCOD3 preliminary version: FASCD3P, 57 pp. [Available from Phillips Laboratory, Hanscom AFB, MA.]

Arking, A., and J. D. Childs, 1985: Retrieval of cloud cover parameters from multispectral satellite images. *J. Climate Appl. Meteor.,* **24,** 322–333.

Baum, B. A., R. F. Arduini, B. A. Wielicki, P. Minnis, and S.-C. Tsay, 1994: Multilevel cloud retrieval using multispectral HIRS and AVHRR data: Nighttime oceanic analysis. *J. Geophys. Res.,* **99,** 5499–5514.

Charlock, T. P., and V. Ramanathan, 1985: The albedo field and cloud radiative forcing produced by a general circulation model with internally generated cloud optics. *J. Atmos. Sci.,* **42,** 1408–1429.

Collard, A. D., S. A. Ackerman, W. L. Smith, X. Ma, H. E. Revercomb, R. O. Knuteson, and S.-C. Lee, 1995: Cirrus cloud properties derived from high resolution infrared spectrometry at the FIRE II experiment. Part I: Ground-based HIS results. *J. Atmos. Sci.,* **52,** 4264–4275.

Cox, S. K., D. S. McDougal, D. A. Randall, and R. A. Schiffer, 1987: FIRE—The first ISCCP regional experiment. *Bull. Amer. Meteor. Soc.,* **68,** 114–118.

d'Entremont, R. P., 1986: Low- and midlevel cloud analysis using nighttime multispectral imagery. *J. Climate Appl. Meteor.,* **25,** 1853–1869.

Grant, I. P., and G. E. Hunt, 1969: Discrete space theory of radiative transfer. I. Fundamentals. *Proc. Roy. Soc. London, Ser. A.,* **313,** 183–197.

Harrison, E. F., P. Minnis, B. R. Barkstrom, V. Ramanathan, R. D. Cess, and G. G. Gibson, 1990: Seasonal variation of cloud radiative forcing derived from the Earth Radiation Budget Experiment. *J. Geophys. Res.,* **95,** 18 687–18 703.

Hartmann, D. L., and D. Doelling, 1991: On the net radiative effectiveness of clouds. *J. Geophys. Res.,* **96,** 869–891.

Huang, R., and K. N. Liou, 1984: Remote sounding of cirrus optical depth and temperature from 3.7 and 11 μm windows. *Adv. Atmos. Sci.,* **1,** 150–164.

Hunt, G. E., 1973: Radiative properties of terrestrial clouds at visible and infrared thermal window wavelengths. *Quart. J. Roy. Meteor. Soc.,* **99,** 346–369.

Li, Z., and H. G. Leighton, 1991: Scene identification and its effect on cloud radiative forcing in the Arctic. *J. Geophy. Res.,* **96,** 9175–9188.

Menzel, W. P., W. L. Smith, and T. R. Stewart, 1983: Improved cloud motion wind vector and altitude assignment using VAS. *J. Climate Appl. Meteor.,* **22,** 377–384.

Ou, S. C., K. N. Liou, W. M. Gooch, and Y. Takano, 1993: Remote sensing of cirrus cloud parameters using advanced very-high resolution radiometer 3.7- and 10.9-μm channels. *Appl. Opt.,* **12,** 2171–2180.

Ramanathan, V., R. D. Cess, E. F. Harrison, P. Minnis, B. R. Barkstrom, E. Ahmad, and D. Hartmann, 1989: Cloud-radiative forcing and climate: Results from the Earth Radiation Budget Experiment. *Science,* **243,** 57–63.

Revercomb, H. E., H. Buijs, H. B. Howell, D. D. LaPorte, W. L. Smith, and L. A. Sromovsky, 1988: Radiometric calibration of IR fourier transform spectrometers: Solution to a problem with the high-spectral resolution interferometer sounder. *Appl. Opt.,* **27,** 3210–3218.

Smith, W. L., and C. M. R. Platt, 1978: Comparison of satellite-deduced cloud heights with indications from radiosonde and ground-based laser measurements. *J. Appl. Meteor.,* **17,** 1796–1802.

——, and R. Frey, 1990: On cloud altitude determinations from High Resolution Interferometer Sounder (HIS) observations. *J. Appl. Meteor.*, **29,** 658–662.

——, H. M. Woolf, P. G. Abel, C. M. Hayden, M. Chalfant, and N. Grody, 1974: Nimbus-5 sounder data processing system. Part 1: Measurement characteristics and data reduction procedures. NOAA Tech. Memo. NESS 57, 99 pp.

——, X. L. Ma, S. A. Ackerman, H. E. Revercomb, and R. O. Knuteson, 1993: Remote sensing cloud properties from high spectral resolution infrared observations. *J. Atmos. Sci.*, **50,** 1708–1720.

——, H. E. Revercomb, S. A. Ackerman, F. A. Best, A. D. Collard, R. Dedecker, H. B. Howell, H. Huang, R. O. Knuteson, X. Ma, and H. M. Woolf, 1995: Cirrus cloud properties derived from high spectral resolution infrared spectrometry during FIRE II. Part I: The high-resolution interferometer sounder (HIS) systems. *J. Atmos. Sci.*, **52,** 4238–4245.

Stephens, G. L., 1980: Radiative properties of cirrus clouds in the infrared region. *J. Atmos. Sci.*, **37,** 435–445.

——, and T. J. Greenwald, 1991: The earth's radiation budget and its relation to atmospheric hydrology. Part I: Observations of the clear sky greenhouse effect. *J. Geophys. Res.*, **96,** 15 311–15 324.

Stone, R. S., G. L. Stephens, C. M. R. Platt, and S. Banks, 1990: The remote sensing of thin cirrus cloud using satellites, lidar and radiative transfer theory. *J. Appl. Meteor.*, **29,** 353–366.

Strabala, K. I., S. A. Ackerman, and W. P. Menzel, 1994: Cloud properties inferred from 8–12 μm data. *J. Appl. Meteor.*, **33,** 212–229.

Takano, Y., K. N. Kiou, and P. Minnis, 1992: The effects of small ice crystals on cirrus infrared radiative properties. *J. Atmos. Sci.*, **49,** 1487–1493.

Wiscombe, W., 1976: Extension of the doubling method to inhomogeneous sources. *J. Quant. Spectrosc. Radiat. Transfer.*, **16,** 477–489.

——, and G. W. Grams, 1976: The backscattered fraction in two-stream approximations. *J. Atmos. Sci.*, **33,** 2440–2451.

——, and J. W. Evans, 1977: Exponential-sum fitting of radiative transmission functions. *J. Comput. Phys.*, **24,** 416–444.

Wylie, D. P., and W. P. Menzel, 1989: Two years of cloud cover statistics using VAS. *J. Climate,* **2,** 380–392.

Reprinted from JOURNAL OF THE ATMOSPHERIC SCIENCES, Vol. 52, No. 23, 1 December 1995
American Meteorological Society

Cirrus Cloud Properties Derived from High Spectral Resolution Infrared Spectrometry during FIRE II. Part III: Ground-Based HIS Results

A. D. COLLARD, S. A. ACKERMAN, W. L. SMITH, X. MA, H. E. REVERCOMB, R. O. KNUTESON, AND S.-C. LEE

Cooperative Institute for Meteorological Satellite Studies, Space Science and Engineering Center, University of Wisconsin-Madison, Madison, Wisconsin

(Manuscript received 19 July 1994, in final form 8 December 1994)

ABSTRACT

During FIRE II, cirrus clouds were observed in the wavelength range 3–19 μm with two High Resolution Interferometer Sounders as described in the Part I companion paper. One, known as AC-HIS, was mounted on the NASA ER-2 aircraft in order to look down on the clouds; these results are described in the Part II companion paper. The other, GB-HIS, also known as the Atmospheric Emitted Radiance Interferometer (AERI), was ground based. The AERI observations have been simulated, assuming scattering from spherical ice particles, using a single-layer doubling model for the cloud, for two atmospheric windows at 700–1250 and 2650–3000 cm^{-1}. The second of these windows is affected by scattered sunlight, which has been included in the calculations. The sensitivity of the cloud signal to quantities such as the ice water path (IWP) and effective radius (r_{eff}) have been determined. Using the cloud model, best fits have been derived for IWP and r_{eff}, for both windows individually and together. Possible errors in these derivations have been investigated.

1. Introduction

The uplooking GB-HIS spectrometer (called the AERI—Atmospheric Emitted Radiance Interferometer) observes at an unapodised spectral resolution of approximately 0.5 cm^{-1} over two bands in the infrared. Band I covers the range 500–1800 cm^{-1}, while band II covers 1800–3000 cm^{-1}. For further details of the characteristics of this instrument and its role in the FIRE II experiment see Part I of this series [Smith et al. (1995) and Revercomb et al. (1993).]

Observations of thin cirrus clouds were made on various days throughout the First ISCCP Regional Experiment-Phase II (FIRE II) period. Specific periods for study were chosen based on having a homogeneous, single cirrus cloud layer and a close clear-sky observation.

The spectral region observed by the GB-HIS is shown in Fig. 1. Emission features due to CO_2, H_2O, and O_3 are apparent. Also, there are two window regions where the atmospheric transmission is greater than 90%. In these regions the effect of cloud is most obvious. The wavelength intervals from 760–1235 cm^{-1} (excluding the ozone band at 1000–1067 cm^{-1}), hereinafter referred to as "window 1," and from 2480–2950 cm^{-1} (window 2) are used for the retrieval of cloud properties.

Corresponding author address: Dr. William L. Smith, CIMSS, Space Science and Engineering Center, University of Wisconsin-Madison, 1225 West Dayton St., Madison, WI 53706.

As noted by Smith et al. (1993), the emissivities of cirrus clouds vary with wavenumber in the window 1 region. Smith et al. used this structure to infer microphysical properties of the clouds. This paper extends the Smith et al. analysis to the band II region. As will be explained later, observed radiances in window 2 arise from a physical process different than that associated with window 1. As a consequence, the cloud emissivity is not as useful a quantity, in this case, for the specification of cloud microphysical properties and as a result is not used in this paper. Here we attempt to derive cloud microphysical properties directly from the GB-HIS radiance observations, using a doubling radiative transfer model and a simple retrieval scheme. These are described below with an investigation of the effect of some of the unknowns and approximations that may affect the conclusions drawn.

2. The radiative transfer model

The analysis of these data uses a single-layer doubling model (Wiscombe 1976a,b) for the clouds with radiances and transmittances of the gaseous atmosphere calculated using FASCODE (Anderson and Chetwynd 1992). Emission from the surface can also affect the observed downwelling radiance through reflection by the clouds. This effect, which is generally more than an order of magnitude less than direct emission from the clouds, is included by assuming that the surface emits as a blackbody.

In this model the atmosphere is divided into three layers corresponding to the regions below, in, and

© 1995 American Meteorological Society

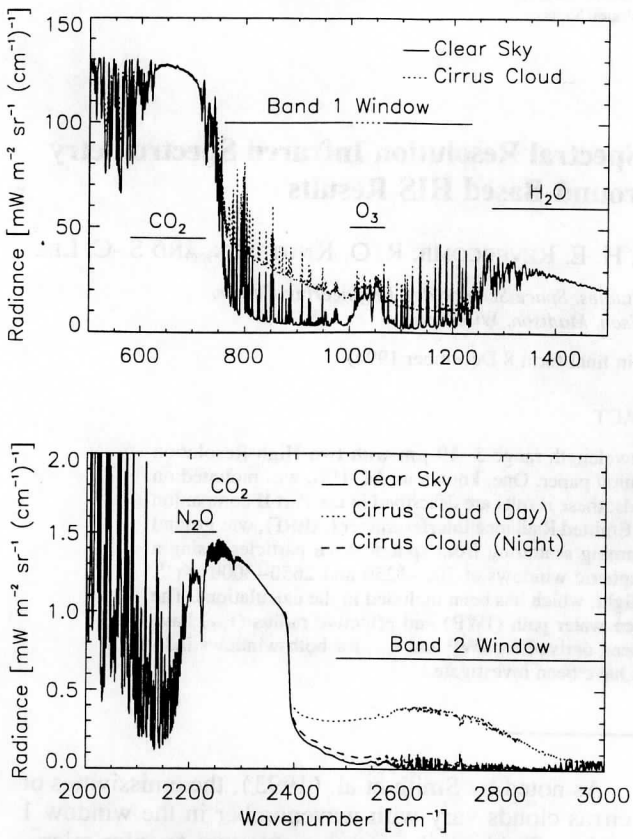

FIG. 1. Simulated GB-HIS observations for a clear-sky case and for the case of a high thin cirrus cloud in daylight. The effect of the cloud can be most readily seen in the window regions between 760 and 1250 cm^{-1} (window 1) and 2380 and 3000 cm^{-1} (window 2). Broad emission features due to H_2O, CO_2, and O_3 can be seen, and even in the band I window region spectral lines (mostly water) are apparent.

above the clouds (Ackerman and Knuteson 1993). FASCODE is used to calculate the transmissions and emergent intensities of each layer. The transmissions are assumed to obey the monochromatic product rule, although they are the average over the GB-HIS spectral response function. This approximation, while not generally valid, particularly in regions of significant gaseous line absorption, is satisfactory in the window regions where the transmissions do not vary greatly across a GB-HIS spectral element.

To allow for uncertainties in the assumed atmospheric state and in the spectroscopy employed in the radiative transfer model, use is made of the "gamma correction" as described by Smith et al. (1993). This correction is a multiplicitive factor applied equally to the optical depths of each layer in the atmosphere and for each observation channel. It is determined by comparing a model run and a clear-sky observation, usually close in time to the cloud observation. The effect of the gamma correction on the retrieved cloud parameters is shown in section 6.

The cloud particle optical properties are calculated using Mie theory for ice spheres in terms of the extinction, the single scattering albedo, and the asymmetry parameter. The latter is converted into a phase function via the Henyen–Greenstein function. A Hansen size distribution (Hansen 1971) is assumed, as given in Eq. (1),

$$n(r)dr = cr^{(1-3b)/b} \exp(-r/r_{\text{eff}}b)dr, \qquad (1)$$

where $n(r)$ is the number of particles of radius r, r_{eff} is the effective radius, b is a variance term, and c is a normalization constant. Reasonable variation in the value of b has a small effect on the cloud radiative properties and is assumed to be 0.25.

The approximation to ice spheres, instead of the multitude of possible particle shapes typical of a cirrus cloud, may cause the retrieved parameters to be inaccurate and/or inconsistent. The effects of particle shape and multimodal particle size distributions are investigated in sections 7 and 8.

For the shorter wavelength window the contribution from the solar radiation is significant. Therefore, the solar source term is included in the model to simulate zenith (as with GB-HIS) or nadir (as with AC-HIS) observations. The solar irradiance used is that of Smith and Gottlieb (1974).

3. Retrieval procedures

A simple retrieval routine is used to find the ice water path and effective radius of the cirrus cloud particles that best fit the downwelling spectral radiance observations. The radiative transfer equations are put into a linear form in order to facilitate the cloud retrieval process.

Fitting parameters are chosen by considering the simplified situation of a thin cloud entirely above the gaseous absorption. In this case the radiance, I_{obs}, observed by an uplooking instrument is given by

$$I_{\text{obs}} = I_{\text{clear}} + I_{\text{cloud}} e^{-\tau}, \qquad (2)$$

where I_{clear} is the emission from the atmosphere below cloud level (assumed to be the same as that of the clear atmosphere) and τ is the optical depth of the atmosphere below the cloud base. Therefore,

$$\log_e I_{\text{cloud}} = \log_e(I_{\text{obs}} - I_{\text{clear}}) + \tau. \qquad (3)$$

For the case of a thin cloud the radiance from the cloud will be proportional to the quotient of the ice water path (IWP) and the effective radius (r_{eff}) so that $I_{\text{cloud}} \propto \text{IWP}/r_{\text{eff}}$. Here, this relationship is generalized to $I_{\text{cloud}} = C_1(\text{IWP})^{\alpha}(r_{\text{eff}})^{\beta}$, where α and β are, for a given wavelength, unknown constants and C_1 is a function of cloud temperature and solar irradiance. Equation (3) becomes

$$\log_e(I_{\text{obs}} - I_{\text{clear}}) = \alpha \log_e(\text{IWP}) + \beta \log_e(r_{\text{eff}}) + C_2, \qquad (4)$$

where $C_2 = C_1 - \tau$ and is constant at a given wavelength.

The constant C_2 can be removed by determining IWP and r_{eff} relative to a known reference model calculation, which produces a radiance I_{ref}. This gives

$$\log_e[(I_{\text{obs}} - I_{\text{clear}})/(I_{\text{ref}} - I_{\text{clear}})] = \alpha \log_e(\text{IWP}') + \beta \log_e(r'_{\text{eff}}), \quad (5)$$

where $\text{IWP}' = \text{IWP}/\text{IWP}_{\text{ref}}$ and $r'_{\text{eff}} = r_{\text{eff}}/(r_{\text{eff}})_{\text{ref}}$. Equation (4) is thus a linear equation in α and β of the form $\mathbf{y} = \mathbf{Kx}$. The values of α and β are determined by running the forward model for a reference case and cases with IWP or r_{eff} slightly perturbed. The problem is now solved using the standard retrieval method of Rodgers (1976) where the retrieved state vector $\hat{\mathbf{x}}$ (in this case, the ice water path and the effective radius) is determined by

$$\hat{\mathbf{x}} = \mathbf{x}_0 + \mathbf{S}_0\mathbf{K}^{\mathrm{T}}(\mathbf{K}\mathbf{S}_0\mathbf{K}^{\mathrm{T}} + \mathbf{S}_\epsilon)^{-1}(\mathbf{y} - \mathbf{K}\mathbf{x}_0), \quad (6)$$

where $\mathbf{y}$ is the vector of observations, $\mathbf{K}$ is the "weighting function" matrix (consisting of the α and β for each wavenumber), $\mathbf{S}_\epsilon$ is the observational error covariance matrix, and $\mathbf{x}_0$ and $\mathbf{S}_0$ are the a priori state vector and its associated error covariance matrix.

To allow for the nonlinearities due to the various approximations employed in this method, Eq. (6) is iterated to convergence.

The functions $\log_e[(I_{\text{obs}} - I_{\text{clear}})/(I_{\text{ref}} - I_{\text{clear}})]$ and $(I_{\text{obs}} - I_{\text{clear}})$ can also be used to quantitatively display the effect of varying cloud microphysical properties. The latter of these is also referred to here as the "cloud forcing," although note the multiplicitive factor due to transmission of the subcloud atmosphere and that this refers to a directional radiance rather than a flux.

4. Sensitivity studies for ice water path and effective radius

Figure 2 shows the scattering properties for ice spheres as calculated using Mie theory for various effective radii. Structure is apparent in the shapes of these functions. It would thus appear that effective radii may be retrievable from the shapes of the cloud forcing functions, $I_{\text{obs}} - I_{\text{clear}}$.

Figure 3 illustrates this further by indicating how $I_{\text{cloud}} - I_{\text{clear}}$ is changed by varying r_{eff} for the case of a high cloud with the parameters described for 26 November 1991 in Table 1a. It is apparent that the spectroscopic variation of $(I_{\text{obs}} - I_{\text{clear}})$ is significant both across window 1 and between windows 1 and 2. For thin clouds the effect of changing the ice water path while keeping r_{eff} fixed is seen to change only the magnitude rather than the shape of $(I_{\text{obs}} - I_{\text{clear}})$. For thick clouds the shape of $(I_{\text{obs}} - I_{\text{clear}})$ changes in both windows, consistent with the increased importance of scattering in window 1 and absorption in window 2 (see below), although for window 1 this effect is no larger than about 10%.

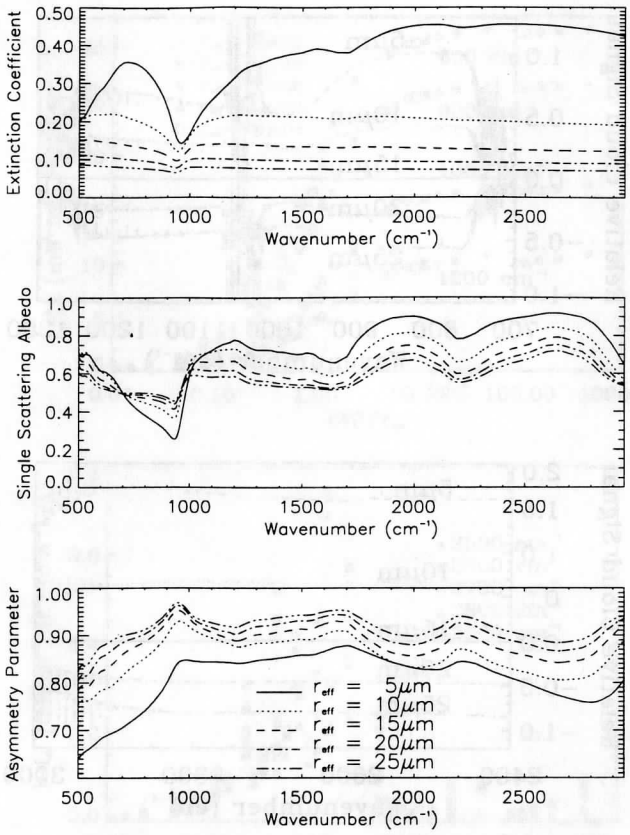

FIG. 2. Spectral properties of ice spheres for the GB-HIS wavenumber interval for five different size distributions. Note the increasing structure with decreasing effective particle size and the relatively flat functions in the window 2 region compared to window 1.

Figures 4a and 4b illustrate the effect of changing IWP and r_{eff} at typical wavelengths in each window. The different radiative properties of the clouds in the two windows are apparent. In window 1 the clouds' signal is due almost entirely to thermal emission. Therefore, the cloud forcing increases with IWP until it reaches an asymptote where the cloud is totally opaque and the signal is a maximum. Window 2, as mentioned above, is dominated by solar scattering, and the cloud forcing thus increases with IWP as the number of particles scattering solar radiation toward the instrument rises. Eventually, the opacity of the cloud increases to the extent that sunlight is prevented from reaching the instrument, and the signal is reduced until only the small contribution of thermal emission remains at high IWP.

Simple geometric considerations indicate that the quotient $\text{IWP}/r_{\text{eff}}$ is proportional to the optical depth of the clouds. Figure 5 indicates how the cloud forcing is related to this quantity for various effective radii. The correlation of $I - I_{\text{clear}}$ with $\text{IWP}/r_{\text{eff}}$ in window 1 is

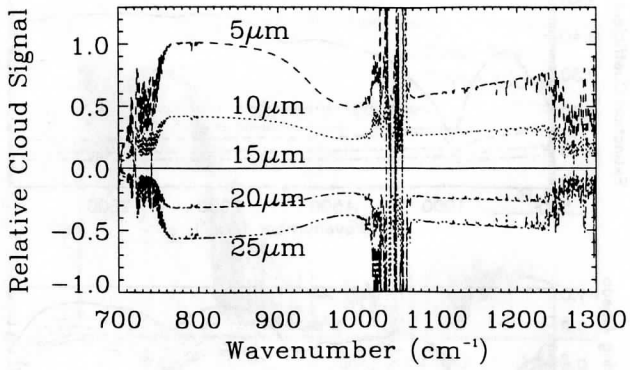

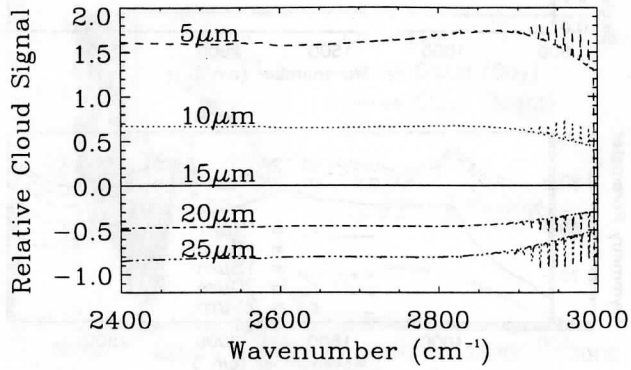

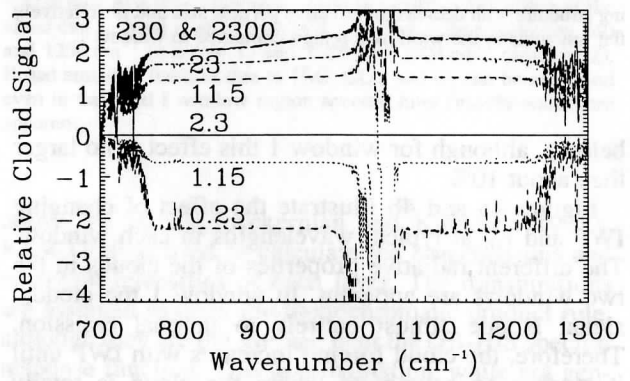

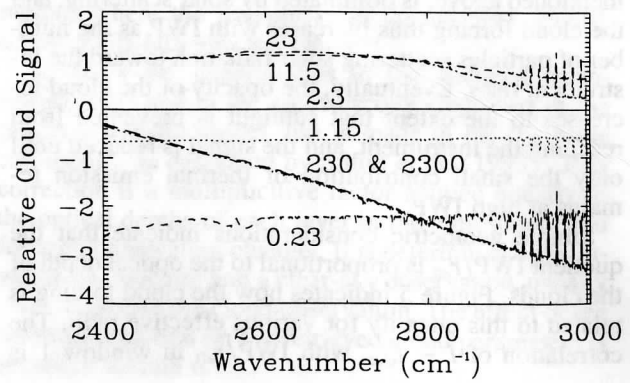

good (to first order, information on particle size can be derived from second-order variations affecting the shape of the cloud spectrum), while for window 2 this parameter does not appear to be useful, which is consistent with the greater importance of particle scattering properties in this window.

5. Observations

The primary observations employed were made with the GB-HIS (i.e., the AERI) instrument from the FIRE II site at Coffeyville, Kansas, in November and December 1991. Use was also made of NCAR Cross-chain linked Atmospheric Sounding System (CLASS) radiosondes for derivation of the temperature and H_2O volume mixing ratio profiles used in the model. Cloud base and top heights are obtained with a CO_2 Doppler lidar operated by NOAA (Intrieri et al. 1993; Uttal et al. 1995). The lidar operates at 10 μm (i.e., in the middle of the GB-HIS band 1), and thus the cloud heights derived are particularly consistent with GB-HIS use.

The observations to be studied in detail are chosen on the basis of a number of criteria. First, to simplify the analysis, observations of a single layer of cirrus cloud with an apparently homogeneous structure are chosen. Second, a radiosonde observation and an observation of a clear-sky radiance both close in time to the AERI observation are desirable.

The determination of a "clear sky" is somewhat ambiguous as very thin clouds may be detected by the CO_2 lidar, which have a totally negligible effect on the observed radiances.[1] The clear-sky observations are thus

[1] Simple calculations show that for a cloud with a temperature of 230 K its emission becomes significant relative to the instrumental and spectroscopic noise when its optical depth is above 0.02. This corresponds to a value of IWP/r_{eff} of around 0.02 g m^{-2} μm^{-1}.

FIG. 3a. The effect on the radiance from a high thin cirrus of changing the effective radius of the cloud particles, keeping the ice water path fixed (2.3 g m^{-2}). The ordinate, $\log_e[(I - I_{\text{clear}})/(I - I_{\text{clear}})_{15\,\mu\text{m}}]$, is the logarithm of the cloud forcing divided by a base model. This essentially removes the effect of transmission of the lower atmosphere. At the edges of the window regions and in the ozone absorption feature around 1040 cm^{-1} there is contamination due to absorption being significant in the cloud layer and above. It may be seen that the magnitude of the cloud forcing varies with wavenumber across the band I window and between the two windows. From this we may conclude that there is size information to be gained from the spectral variation in the cloud response in these regions.

FIG. 3b. As in Fig. 3a except the curves are for different ice water paths (in g m^{-2}) and are plotted relative to the signal for a cloud with IWP = 23 g m^{-2}. The effective radius is kept fixed at 15 μm. For thin clouds the curves are spectrally flat, from which we may conclude that only the magnitude and not the shape of the cloud forcing is dependent on the ice water path in this case. In both windows thicker clouds introduce some extra spectral structure. For the band I window this is small (~10%) and is probably due to the increased influence of scattering. In the band II window the effect is larger and probably a direct result of the transmission of the cloud becoming more important (see text).

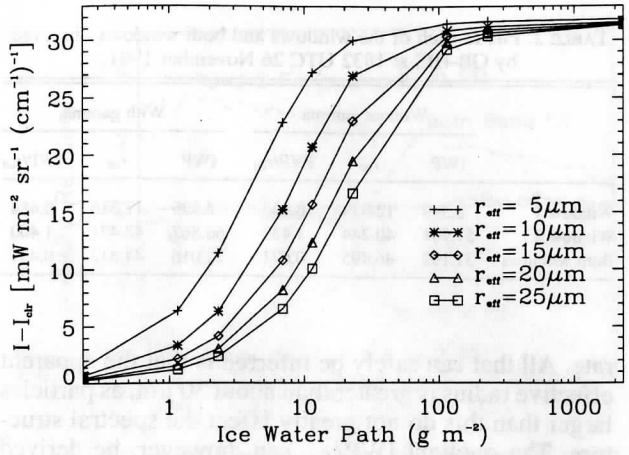

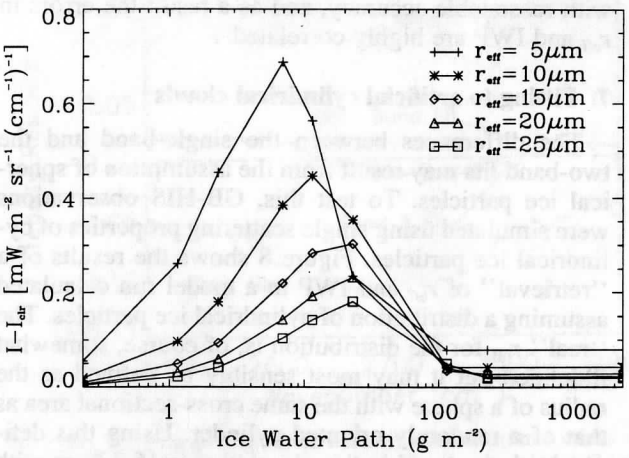

FIG. 4a. Variation of the cloud forcing (multiplied by the transmission of the lower atmosphere, about 0.9) with ice water path and effective radius for a typical model high thin cirrus cloud at 800 cm^{-1}, i.e., in the thermal emission dominated band I window. The cloud forcing increases monotonically with ice water path until the cloud is essentially opaque and the signal is a maximum.

FIG. 4b. As in Fig. 4a except for 2600 cm^{-1} (window 2). The calculations assume incident sunlight, and the result is that for small ice water paths the cloud signal increases with IWP as more sunlight is scattered toward the instrument. At larger IWP the opacity of the cloud reduces the scattered sunlight reaching the GB-HIS until only the small thermal emission term remains as the cloud becomes opaque.

chosen on the basis of a combination of lidar observations, visual logs made by GB-HIS operators, and variations of the observed radiances with time. It shall be seen that the gamma-corrected radiances and transmittances produced here appear to be adequate for the cloud parameter retrieval process.

One time period was thus chosen for study, between 1800 and 1900 UTC 26 November 1991. This is also useful as r_{eff} and IWP have independently been derived by Intrieri et al. (1993) using a combination of microwave and infrared radar/lidar. Further information on the observation period chosen is given in Table 1a. The clear-sky observation was made at 1722 UTC.

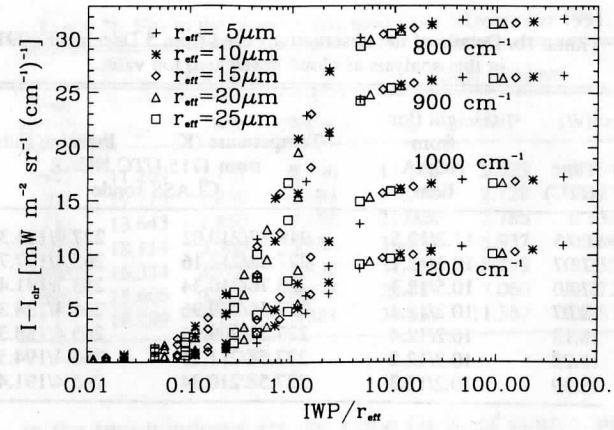

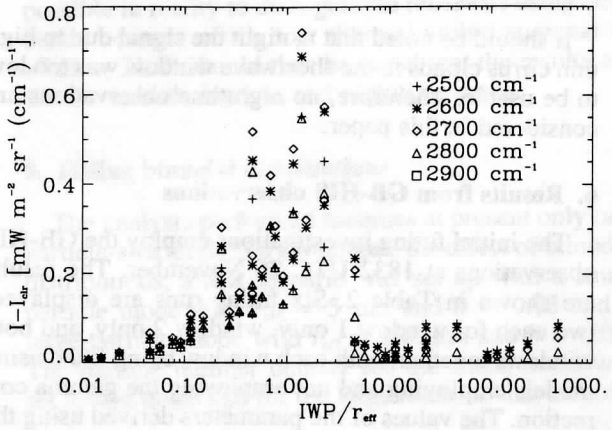

FIG. 5a. As in Fig. 4a except the cloud forcing is now plotted vs IWP/r_{eff}. This quotient is proportional to the optical depth of the cloud. Four wavenumbers are plotted: (top to bottom) 800, 900, 1000, and 1100 cm^{-1}. It can be seen that correlation between IWP/r_{eff} and $I - I_{clear}$ is good in all cases.

FIG. 5b. As in Fig. 5a except for five window 2 wavenumbers. The correlation is not good, indicating the more complicated radiative processes in this window. Note that, unlike Fig. 5a, the symbols refer to different frequencies, not different particle sizes.

A second, though less satisfactory, period is also analyzed. This is 1645–1839 UTC 5 December 1991; details are given in Table 1b.

TABLE 1a. Details of the observations used from 26 November 1991 in this analysis as cloud base/cloud top value.

Time (UTC)	Height (km) from NOAA lidar	Temperature (K) from 1716 UTC NCAR CLASS sonde	Pressure (mb)
18.01	8.7/10.5	228.68/213.99	324.2/245.3
18.12	8.5/10.4	230.47/213.83	334.0/249.3
18.22	8.5/10.4	230.47/213.83	334.0/249.3
18.32	8.7/10.5	228.68/213.99	324.2/245.3
18.43	8.3/10.7	231.93/215.55	344.0/237.6
18.53	8.3/10.5	231.93/213.99	344.0/245.3

TABLE 1b. Details of the observations used from 5 December 1991 in this analysis as cloud base/cloud top value.

Time (UTC)	Height (km) from NOAA lidar	Temperature (K) from 1715 UTC NCAR CLASS sonde	Pressure (mb)
16.45	11.2/12.5	219.87/210.02	227.9/185.3
17.07	10.2/12.1	227.58/212.16	265.4/197.7
17.40	10.5/12.3	225.76/210.34	253.7/191.4
18.07	10.2/12.4	227.58/209.96	265.4/188.3
18.18	10.2/12.4	227.58/209.96	265.4/188.3
18.28	10.2/12.2	227.58/211.25	265.4/194.5
18.39	10.2/12.3	227.58/210.34	265.4/191.4

It should be noted that at night the signal due to high thin cirrus clouds in the shortwave window was too low to be usable. Therefore, no nighttime observations are considered in this paper.

6. Results from GB-HIS observations

The initial fitting investigations employ the GB-HIS observations at 1832 UTC 26 November. The results are shown in Table 2. Six fitting runs are displayed: two each for window 1 only, window 2 only, and both windows together, with each window being fitted using models employing and not employing the gamma correction. The values of the parameters derived using the gamma correction are very similar to those derived without, but a large difference is found between the values of r_{eff} and IWP using the different windows.

The significance of (a) the gamma functions and (b) the use of the different windows for fitting can be appreciated in Figs. 6 and 7. Figure 6 compares a window 1 fit with and without the gamma function. It is obvious that, while both fits return similar parameter values, the fit without the correction is far less convincing.

Figure 7 shows a large error in the radiances of the other window when fits are made in one window only. The both-window fit is almost as good as the window 2 fit in band II, but in band I, the spectral variation of the cloud signal is not well matched, and the window 1 fit is clearly superior.

A comparison between the values of IWP/r_{eff} for each case investigated reveals that this value is approximately the same for the "both windows" and "window 1 only" fit, but is markedly different when window 2 is used. This inconsistency between the two regions may, of course, be a phenomenon peculiar to the time of the observation. Hence, the same analysis is now carried out for other times in the periods discussed above. The results of these (for the both windows and window 1 only cases) are presented in Tables 3a and 3b. The differences between the two fits and the absolute effective radii derived are consistent for all observations.

It should be noted that the values for IWP and r_{eff} obtained from both window fits are somewhat inaccurate. All that can safely be inferred is that the apparent effective radius is greater than about 30 μm, as particles larger than this do not greatly affect the spectral structure. The quotient IWP/r_{eff} can, however, be derived with reasonable accuracy, and as a result the errors in r_{eff} and IWP are highly correlated.

TABLE 2. Fits to each of the windows and both windows observed by GB-HIS at 1832 UTC 26 November 1991.

	Without gamma			With gamma		
	IWP	r_{eff}	IWP/r_{eff}	IWP	r_{eff}	IWP/r_{eff}
Window 1	8.599	12.934	0.665	8.375	17.316	0.484
Window 2	57.901	40.244	1.439	60.867	43.471	1.400
Both windows	31.192	46.495	0.671	22.016	44.812	0.491

7. Fitting to artificial cylindrical clouds

The differences between the single-band and the two-band fits may result from the assumption of spherical ice particles. To test this, GB-HIS observations were simulated using single scattering properties of cylindrical ice particles. Figure 8 shows the results of a "retrieval" of r_{eff} and IWP to a model run calculated assuming a distribution of cylindrical ice particles. The "real" r_{eff} for the distribution is, of course, somewhat illdefined but it may most sensibly be defined as the radius of a sphere with the same cross-sectional area as that of a randomly oriented cylinder. Using this definition, the r_{eff} used in this simulation is 16.33 μm with an ice water path of 2.3 gm^{-2} (which gives a value for IWP/r_{eff} of 0.141). The results of attempting to fit these "observations" using the ice sphere model are given in Tables 4a (for daytime) and 4b (for night).

These fits show a similar quantitative behavior to those obtained above using the real observations in that

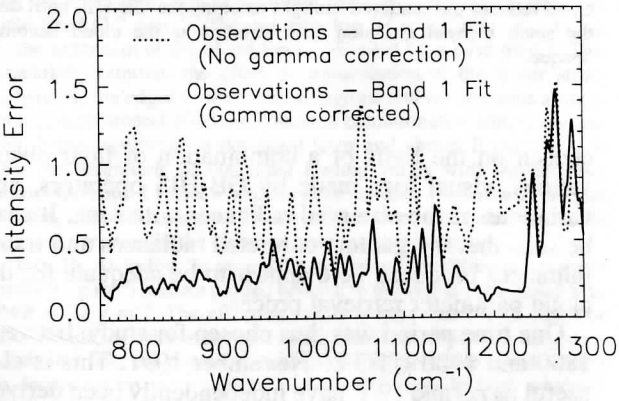

FIG. 6. The fitting error (observed minus fitted intensity) in window 1 for the case of 1832 UTC 26 November 1991. For clarity, the function shown is the square root of the result of smoothing the square of the true fitting error. As can be seen, the use of the gamma correction significantly reduces the observation–fit discrepancy.

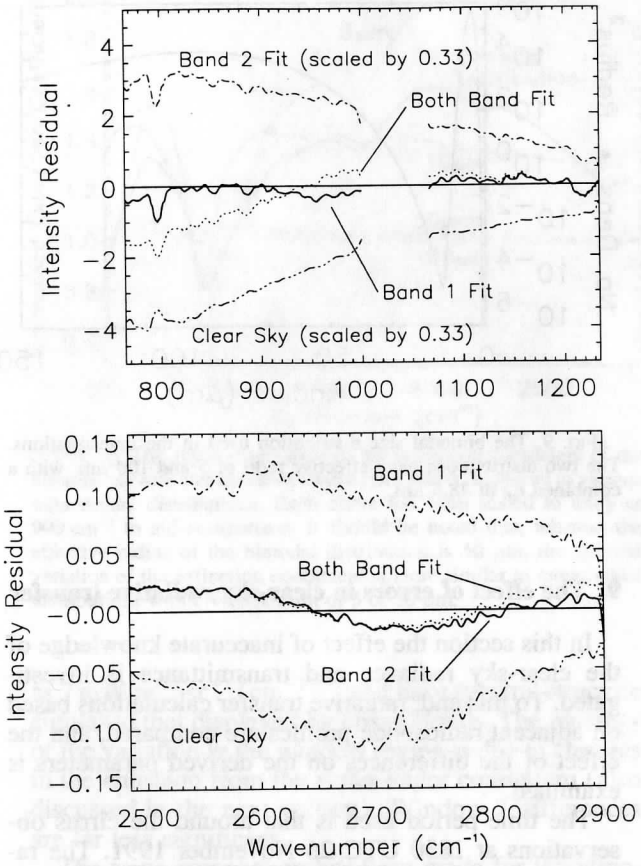

FIG. 7. A comparison of the intensity residuals (fitted minus observed intensity) for retrievals using window 1 only, window 2 only, and both windows together. Also shown is the clear sky − observed difference. The curves are smoothed to 5 cm^{-1} resolution for clarity.

markedly different values of the parameters are required to fit window 1 and both windows together. One may thus conclude that the discrepancies between the two fits in the observations may be related to the crude representation of the shapes used. While large differences exist in the retrievals of IWP and r_{eff}, the spherical particle assumption does a reasonable job of retrieving the ratio (IWP/r_{eff}), which is proportional to cloud optical depth.

The simulated nighttime investigations are important, as they provide a test where the radiative processes

TABLE 3a. Fits to the observations used from 26 November 1991.

Time (UTC)	Window 1			Both windows		
	r_{eff}	IWP	IWP/r_{eff}	r_{eff}	IWP	IWP/r_{eff}
1801	21.275	11.311	0.532	55.704	29.952	0.538
1812	14.430	2.176	0.151	73.773	11.172	0.151
1822	15.799	2.451	0.155	127.272	20.072	0.158
1843	13.544	7.706	0.569	33.944	18.787	0.553
1853	17.176	6.974	0.406	73.372	31.365	0.427

TABLE 3b. Fits to the observations used from 5 December 1991.

Time (UTC)	Window 1			Both windows		
	r_{eff}	IWP	IWP/r_{eff}	r_{eff}	IWP	IWP/r_{eff}
1645	11.269	2.137	0.190	13.748	2.523	0.184
1707	19.713	1.830	0.093	29.213	2.728	0.093
1740	13.645	1.850	0.136	21.004	2.785	0.133
1807	18.114	3.366	0.186	36.933	6.937	0.188
1818	16.334	3.788	0.232	37.406	8.793	0.235
1828	15.605	4.292	0.275	25.787	7.060	0.273
1839	18.289	5.137	0.281	39.657	11.367	0.287

in the two windows are the same (it is, of course, not possible in reality to do nighttime retrievals using both bands because of the low thermal emission signal in window 2). It should thus be noted that the results are similar in both daytime and nighttime cases.

8. Fitting bimodal distributions

The analysis performed assumes at present only one particle-size mode. To investigate the effect of bimodal distributions, a test scenario was set up with a small particle mode with r_{eff} = 5 μm and b = 0.03 and a large-particle mode with r_{eff} = 100 μm and b = 0.05. The particle number density for the small mode was set to 444 times that for the large mode so that the total

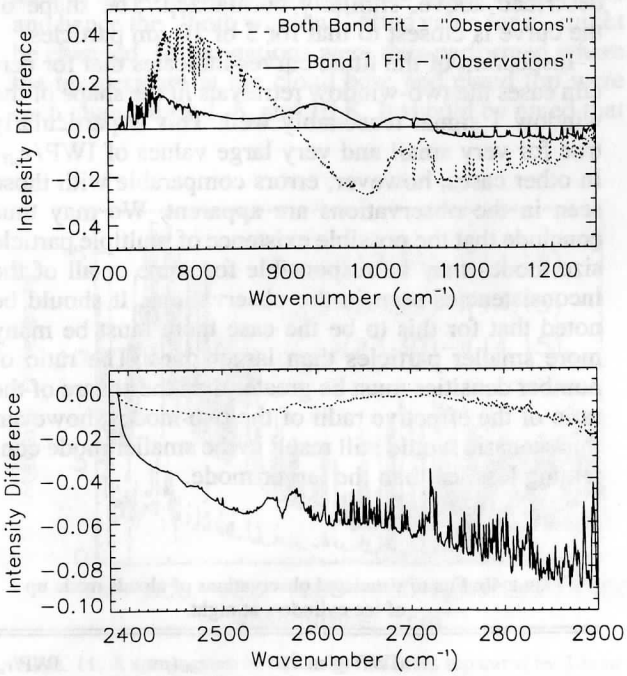

FIG. 8. A comparison of fits to an artificial observation produced assuming a distribution of cylindrical particles with effective radius 16.33 μm and an IWP of 2.3 g m^{-2}. As with the real observations, a consistent fit for window 1 and both windows is not possible.

TABLE 4a. Fits to simulated observations of clouds made up of ice cylinders in the daytime.

	IWP (g m^{-2})	r_{eff} (μm)	IWP/r_{eff}
Window 1	1.1983	9.37	0.128
Window 2	0.5957	4.45	0.134
Both windows	0.6486	4.68	0.134

cross-sectional areas of the two modes are approximately equal and the combined effective radius is 48.50 μm. This distribution is shown in Fig. 9.

Artificial observations are then produced using the cloud characteristics described with varying ice water paths. Results are summarized in Table 5.

It can be seen immediately that the derived effective radii are significantly smaller than truth. The optical depths (approximately proportional to IWP/r_{eff}) are generally quite close, resulting in the IWPs being significantly smaller also. This is not surprising when one considers that, at these wavelengths, the optical properties of smaller ice spheres vary most with size (as is apparent from Fig. 2), and as a result the average properties of a 5-μm and a 100-μm particle are going to resemble a 10-μm particle rather than one with a radius of 50 μm.

To illustrate this further, in Fig. 10 the extinction coefficients of various monomodal distributions are plotted, normalized to unity at 900 cm^{-1}. Also plotted is the extinction coefficient for the bimodal distribution described above, similarly normalized. The shape of the curve is closest to that for 5 or 10 μm particles.

Inspection of the fitted curves indicates that for certain cases the two-window retrievals fit the shape of the window 1 signal reasonably well. This is particularly true for very small and very large values of IWP/r_{eff}. In other cases, however, errors comparable with those seen in the observations are apparent. We may thus conclude that the possible existence of multiple particle size modes may be responsible for some or all of the inconsistencies seen in the observations. It should be noted that for this to be the case there must be many more smaller particles than larger ones. The ratio of number densities must be greater than the square of the ratio of the effective radii of the two modes; however, this scenario would still result in the smaller mode containing less ice than the larger mode.

TABLE 4b. Fits to simulated observations of clouds made up of ice cylinders at night.

	IWP (g m^{-2})	r_{eff} (μm)	IWP/r_{eff}
Window 1	1.1937	9.35	0.128
Window 2	0.6670	4.52	0.148
Both windows	0.8349	5.75	0.145

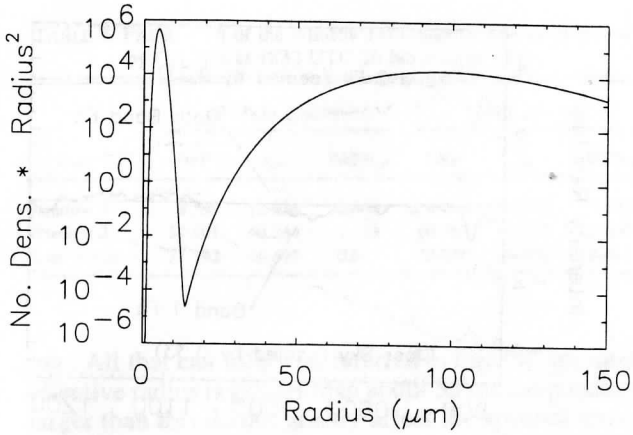

FIG. 9. The bimodal size distribution used in the investigations. The two distributions have effective radii of 5 and 100 μm, with a combined r_{eff} of 48.5 μm.

9. The effect of errors in clear-sky radiative transfer

In this section the effect of inaccurate knowledge of the clear-sky radiance and transmittance is investigated. To this end, radiative transfer calculations based on adjacent radiosonde profiles are compared, and the effect of the differences on the derived parameters is examined.

The time period used is that around the cirrus observations at 1830 UTC 26 November 1991. The radiosonde times are 1412, 1725, and 2330 UTC, which are from 0812 until 1730 local time. The skies were clear at the time of the first two observations, while at 2025 there were cirrus clouds overhead, and there was a mixed cloud layer at 2330.

Figure 11 shows the differences in the clear-sky radiances relative to the 2330 case for window 1. Differences in radiances between adjacent sondes are as large

TABLE 5. Fits to artificial clouds with the bimodal particle-size distribution described in the text with the fitting routine assuming a monomodal distribution.

	IWP	r_{eff}	IWP/r_{eff}
Actual IWP = 2.3 (g m^{-2}) (IWP/r_{eff} = 0.0474)			
Window 1	0.460	10.533	0.0436
Window 2	0.276	7.351	0.0375
Both windows	0.391	9.091	0.0430
Actual IWP = 23.0 (g m^{-2}) (IWP/r_{eff} = 0.474)			
Window 1	4.250	9.346	0.455
Window 2	1.840	6.620	0.278
Both windows	3.452	8.995	0.384
Actual IWP = 230 (g m^{-2}) (IWP/r_{eff} = 4.74)			
Window 1	44.30	10.497	4.22
Window 2[a]	—	—	—
Both windows	92.63	22.027	4.21

[a] Does not converge after ten iterations.

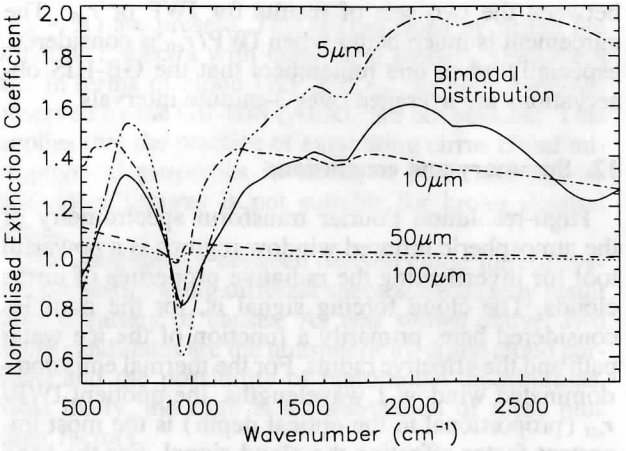

FIG. 10. The spectral variation of the extinction coefficient of the bimodal particle size distribution used in the text compared to various monomodal distributions. Each curve has been scaled to unity at 900 cm^{-1} to aid comparison. It should be noted that, whereas the effective radius of the bimodal distribution is 50 μm, the spectral variation of the extinction coefficient is more similar to monomodal distributions with effective radii of 5 or 10 μm.

as 7 mW m^{-2} sr^{-1} $(cm^{-1})^{-1}$ and have spectral structure similar to that displayed by cirrus clouds. The majority of the variation in the window region is due to changes in the emission from the water vapor continuum (also discussed in the next section). Window 2 differences are far less significant.

The same comparison has been made for the atmospheric transmission. The effect here is relatively small (only about 5% at maximum) and can be ignored relative to the error in the radiances.

Detailed investigation of the effect of radiance errors on retrieval of the microphysical properties of thin cirrus indicates that it is difficult to accurately derive an effective radius or ice water path from window 1 alone, unless an adjacent (i.e., within about 1 hour) clear-sky observation is available; however, it is still possible to retrieve IWP/r_{eff} to within 10% typically. When both windows are used, the situation improves slightly, but still inaccuracies in the window 1 radiances would only allow accurate microphysical retrievals in limited cases unless an adjacent clear-sky observation is used.

10. Investigation of other possible sources of error

A number of other quantities may conceivably affect the above results. Here we investigate the effect on the retrieval of

(i) uncertainties in the H_2O self- and foreign-broadened continuum,
(ii) the cloud top, base, and, mean temperature, and
(iii) cloud thickness.

Investigations of cases where the H_2O self-broadened continuum is changed by 20% for a typical FIRE II atmosphere reveal a difference in the downward radiance at the surface of 1 mW m^{-2} sr^{-1} $(cm^{-1})^{-1}$ at 750 cm^{-1} dropping to near zero at 1400 cm^{-1}, a behavior that mimics the differences seen between the window 1 and both-window fits for thin clouds. It should be noted that for humid atmospheres this radiance error can be as large as 10 mW m^{-2} sr^{-1} $(cm^{-1})^{-1}$. The water continuum should theoretically have only a minor effect on the retrieved values as long as the clear-sky radiances are accurately reproduced. This can still leave an error in lower-level transmittances, which in turn can affect the results. This error is an effect of the nature of the gamma correction, which, as stated above, scales the optical depths equally throughout the atmosphere. In the case of the water continuum, or indeed any far-wing or pressure-induced opacity, the absorption is proportional to the square of the density, and therefore any errors may be expected to be concentrated in the lower layers of the atmosphere. If the clouds are sufficiently high, as in the case of the cirrus clouds being investigated here, this source of error should also be negligible.

Therefore, while the effect of the water continuum in affecting these conclusions is almost certainly small, greater confidence can be placed in these results if an accurate representation of this effect can be included.

Errors in the temperature of the clouds may be more significant. Observed radiances from window 1 are almost entirely thermal, while window 2 observations are dominated by scattered solar radiation. One might therefore expect that the ratio of the two windows' signals to be affected by changing the cloud temperature and hence the "both window" fitted value for r_{eff} might be changed. Investigations were thus performed where the temperature at the cloud base and cloud top were each changed by 1, 5, and 10 K. It should be noted that

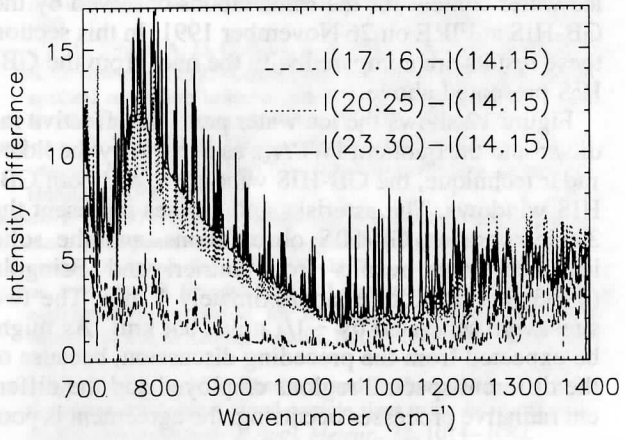

FIG. 11. A comparison of clear-sky radiances separated by 3-hour intervals as calculated from radiosonde data on 26 November 1991. The skies were clear for the 1415 and 1716 sondes, there were cirrus clouds at 2025, and there were mixed cloud layers at 2330. All times are UTC.

TABLE 6. Sensitivities of derived IWP and effective radii to cloud temperatures (percentage change per Kelvin).

Parameter being varied	Percent change in IWP (K)	Percent change in r_{eff} (K)
Cloud-top temperature: window 1 only	−2.0	−0.6
Cloud-top temperature: both windows	−2.3	−0.8
Cloud-base temperature: window 1 only	−4.0	−1.5
Cloud-base temperature: both windows	−4.0	−1.0

the cloud model assumes a linear variation in the temperature across the layer, and so changing the top or base temperature will have an affect throughout the cloud. The sensitivities to these changes are given in Table 6 in terms of percent change in IWP (or r_{eff}) per degree Kelvin.

These errors can thus be large if the temperature of the clouds is not known to within about 10 K. The larger errors are in the ice water path, however, and the above discrepancies in the effective radius derived from the two windows are not explainable with any reasonable temperature profile errors.

Experiments changing the cloud thickness have been found to result, as expected, in simply changing the ice water content by a similar factor, keeping the total ice water path the same. The effect on the effective radius was found to be at most 0.02%.

11. Comparison of results with lidar/radar measurements

Using combined lidar and radar observations, Intrieri and Feingold (1993) derived an effective radius and ice water content for the same clouds observed by the GB-HIS at FIRE on 26 November 1991. In this section these results are compared with the ones from the GB-HIS presented above.

Figure 12 shows the ice water path, the effective radius,[2] and the quotient IWP/r_{eff} as derived by the lidar/radar technique, the GB-HIS window 1, and both GB-HIS windows. The asterisks and crosses represent the 3-min-averaged GB-HIS observations, and the solid line represents results from Intrieri and Feingold (1993) averaged over approximately 1 min. The two sites were separated by ~1/4 mile (0.4 km). As might be expected from the preceding discussion, because of the different spectral regions employed and the different radiative processes occurring, the agreement is poor between the two sets of results for IWP or r_{eff}. The agreement is much better when IWP/r_{eff} is considered, especially when one remembers that the GB-HIS observations are averaged over 3-minute intervals.

[2] The effective radius used here for the lidar/radar observations is the average over the entire cloud weighted according to the particles' total cross-sectional area at each height.

12. Summary and conclusions

High-resolution Fourier transform spectrometry of the atmospheric infrared window regions is a powerful tool for investigating the radiative properties of cirrus clouds. The cloud forcing signal is, for the particles considered here, primarily a function of the ice water path and the effective radius. For the thermal emission–dominated window 1 wavelengths, the quotient IWP/r_{eff} (proportional to the optical depth) is the most important factor affecting the cloud signal. For the band II window scattering of solar radiation results in IWP/r_{eff} not being as useful a parameter.

The observed structure in the cloud spectrum in the band I window region indicates that small particles

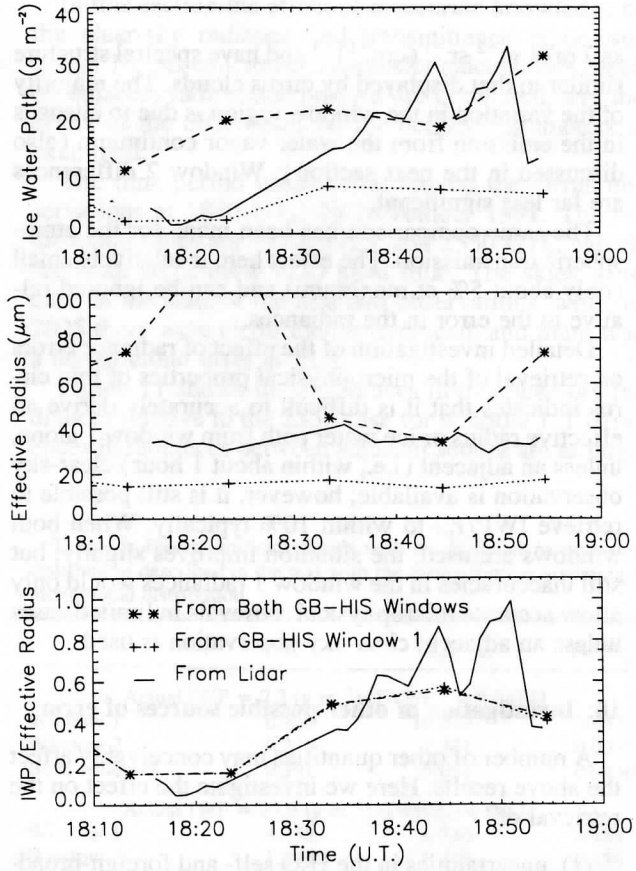

FIG. 12. A comparison between the results (effective radius, ice water path, and IWP/r_{eff}) obtained from the AERI analysis and those obtained by Intrieri and Feingold (1993) for 26 November 1991 between 1800 and 1900 UTC. The asterisks and crosses represent the 3-min averaged AERI observations for both windows and window 1, respectively, while the solid line is 1-minute averages of the lidar/radar results.

($r_{eff} \sim \lambda$) are present. This is confirmed by fitting the window 1 spectra with theoretical models. Consistent fits, in terms of cloud IWP and r_{eff}, in both windows observed by the GB-HIS (AERI) are not possible. This implies that the practice of expressing cirrus cloud microphysical properties in terms of IWP and r_{eff} for equivalent spheres is not suitable for broad spectral bands.

The discrepancy between derived cloud microphysical properties using different spectral bands may result from a variety of causes. As was shown above, two likely candidates are the nonsphericity of the cloud particles and the possibility of multimodal distributions. Most likely, the truth is a combination of these plus other factors.

The investigations into bimodality above also illustrated that the results are liable to be biased by the sensitivity of the radiance spectrum to different particle sizes. Specifically, it is apparent that the technique presented here is much more accurate in deriving the size of small particles (less than about 30 μm); larger particles tend not to affect the spectral signal as much. This insensitivity to larger particles results in large uncertainties in the derived IWP. Similarly, the lidar/radar technique of Intrieri et al. (1993) can measure particle sizes only above 30 μm, and while the IWP probably can be derived satisfactorily, the detailed spectral structure in the infrared radiances cannot be reproduced with the effective radii determined via this method. Good agreement between the GB-HIS measurements and Intrieri and Fiengold (1993) was found for the ratio of IWP/r_{eff}. Possibly the combination of lidar, radar, and spectral infrared measurements may enable a more accurate estimate of the cloud particle-size distribution.

Probably the most important effects not investigated here concern the spatial structure of cirrus clouds. The effect of vertical structure and possible separation of different particle sizes with height should be investigated soon. The effect of horizontal structure is possibly more significant; in the present work the radiative transfer problem is assumed to be essentially one dimensional. Cirrus clouds are, of course, often in the form of complex wisps of cloud, and the radiative transfer scenario is unlikely to be as simple as assumed. Furthermore, the GB-HIS integration time (about 3 min) gives time for the scene in the field of view to vary as the clouds move across the sky, complicating the situation even more. The nearly continuous dataset available from the AERI at the DOE Atmospheric Radiance Measurement (ARM) program Cloud and Radiation Testbed (CART) site near Lamont, Oklahoma, especially the cloud intensive operation periods, provide the observations needed for these future studies.

A method must thus be found to adequately describe the radiative effect of cirrus clouds with as few parameters as possible without the use of a single effective radius. In window 1 the determination of emissivities alone may suffice, but in the presence of sunlight something more is required to model the observed radiances in window 2. A compilation of inferred optical depths and asymmetry parameters may be the answer. Alternatively, it may prove to be the case that clouds can be modeled adequately by assuming the particles to be Mie scatterers but with differing (but possibly correlated) effective radii in the two windows. These possibilities will be the subject of future investigations.

It is demonstrated that consistent retrievals of the ratio IWP/r_{eff} are possible, which is proportional to cloud optical depth. An effective radius for a given spectral bandpass may thus be inferred given independent measurements of the IWP. In addition, the presence of small ice particles within the cloud is detectable using the high spectral resolution measurements.

Finally, it should be noted that, in terms of brightness temperature, the daytime signal from clouds in the band II window is much larger than that from band I, as the former is mostly due to scattered sunlight. Furthermore, the effect of the water continuum in band II is far less significant. Therefore, when the sun is above the horizon, observing in the band II window can be a very useful means of cloud detection.

Acknowledgments. The authors thank everyone who assisted in the AERI project and in particular R. G. Dedecker, H. B. Howell, and H. M. Woolf. Thanks must also go to J. M. Intrieri for supplying the data from the NOAA lidar/radar experiment. This research was supported by the NASA Grant NAG1-1177 and by the DOE Grant DE-FG-02-92ER61365.

REFERENCES

Ackerman, S. A., and R. O. Knuteson, 1993: Multiple scattering algorithm for use with line-by-line RTE models. *SPIE,* **1934,** 373–380.

——, W. L. Smith, A. D. Collard, X. L. Ma, H. E. Revercomb, and R. O. Knuteson, 1995: Cirrus cloud properties derived from high spectral resolution infrared spectrometry during FIRE II. Part II: Aircraft HIS results. *J. Atmos. Sci.,* **52,** 4246–4263.

Anderson, G. P., and J. H. Chetwynd, 1992: FASCOD3 preliminary version: FASCD3P, 57 pp. [Available from Phillips Laboratory, Hanscom AFB, MA.]

Hansen, J. E., 1971: Multiple scattering of polarized light in a planetary atmosphere. Part II: Sunlight reflected by terrestrial water clouds. *J. Atmos. Sci.,* **28,** 1400–1426.

Intrieri, J. M., and G. Feingold, 1993: Lidar and radar derived cirrus microphysical properties for the 26th November 1991 case study. Fire Cirrus Science Results, NASA Conf. Publ. 3238, 48–51.

——, G. L. Stephens, W. L. Eberhard, and T. Uttal, 1993: A method for determining cirrus cloud particle sizes using lidar and radar backscatter technique. *J. Appl. Meteor.,* **32,** 1074–1082.

Revercomb, H. E., W. L. Smith, R. O. Knuteson, F. A. Best, R. G. Dedecker, T. P. Dirkx, R. A. Herbsleb, J. F. Short, and H. B. Howell, 1993: A ground-based system for measuring atmospheric emitted radiance at high spectral resolution. *Optical Remote Sensing of the Atmosphere Technical Digest, 1993,* **5,** 82–85.

Rodgers, C. D., 1976: Retrieval of atmospheric temperature and composition from remote measurements of thermal radiation. *Rev. Geophys. Space Phys.*, **14,** 609–624.

Smith, E. V. P., and D. M. Gottlieb, 1974: Solar flux and its variations. *Space Sci. Rev.*, **16,** 771–802.

Smith, W. L., X. L. Ma, S. A. Ackerman, H. E. Revercomb, and R. O. Knuteson, 1993: Remote sensing cloud properties from high spectral resolution infrared observations. *J. Atmos. Sci.*, **50,** 1708–1720.

——, H. E. Revercomb, S. A. Ackerman, F. A. Best, A. D. Collard, R. G. Dedecker, H. B. Howell, H. Huang, R. O. Knuteson, X. Ma, and H. M. Woolf, 1995: Cirrus cloud properties derived from high spectral resolution infrared spectroscopy during FIRE II. Part I: The high resolution interferometer sounder (HIS) systems. *J. Atmos. Sci.*, **52,** 4238–4245.

Uttal, T., J. M. Intrieri, T. P. Ackerman, W. L. Eberhard, and E. Clothiaux, 1995: Cloud boundary statistics during FIRE II. *J. Atmos. Sci.*, **52,** 4276–4284.

Wiscombe, W., 1976a: Extension of the doubling model to inhomogeneous sources. *J. Quant. Spectrosc. Radiat. Transfer,* **16,** 477–489.

——, 1976b: On initialization, error and flux conservation in the doubling method. *J. Quant. Spectrosc. Radiat. Transfer,* **16,** 637–658.

Reprinted from JOURNAL OF THE ATMOSPHERIC SCIENCES, Vol. 52, No. 23, 1 December 1995
American Meteorological Society

Cirrus Cloud Properties Derived from High Spectral Resolution Infrared Spectrometry during FIRE II. Part I: The High Resolution Interferometer Sounder (HIS) Systems

W. L. SMITH, H. E. REVERCOMB, R. O. KNUTESON, F. A. BEST,
R. DEDECKER, H. B. HOWELL, AND H. M. WOOLF

Cooperative Institute for Meteorological Satellite Studies, Space Science and Engineering Center, University of Wisconsin-Madison, Madison, Wisconsin

(Manuscript received 19 July 1994, in final form 8 December 1994)

ABSTRACT

The characteristics of the ER-2 aircraft and ground-based High Resolution Interferometer Sounder (HIS) instruments deployed during FIRE II are described. A few example spectra are given to illustrate the HIS cloud and molecular atmosphere remote sensing capabilities.

1. Introduction

During the First ISCCP Regional Experiment Phase II (FIRE II), the University of Wisconsin Cooperative Institute for Meteorological Satellite Studies operated two different Michelson interferometers for measuring the upwelling and downwelling radiation from the atmosphere. One of the instruments flew abroad the (NASA) ER-2 aircraft, based in Houston, Texas, during the experiment, and observed the upwelling infrared radiance spectrum, 3.5–17 μm, with a spectral resolution ($\lambda/\Delta\lambda$) of approximately 3000. The other interferometer was ground based at Coffeyville, Kansas, and observed the downwelling infrared radiance spectrum, 3.0-20 μm, with a spectral resolution ($\lambda/\Delta\lambda$) of 1000–6000. As shown in the companion papers of Ackerman et al. (1995) and Collard et al. (1995), these spectra are used to diagnose the optical properties of clouds as needed to evaluate the utility of satellite measurements for defining clouds and radiation budgets essential to climate and global change studies, such as those obtained by the International Satellite Cloud Climatology Program (ISCCP). The purpose of this paper is to describe the characteristics of the High Resolution Interferometer Sounder (HIS) systems used during FIRE II and to illustrate their capabilities with a few examples of the measurements obtained during the experiment.

2. The aircraft HIS instrument

The ER-2 aircraft HIS instrument (Fig. 1) was developed in the early 1980s to demonstrate improved vertical sounding capabilities with high spectral resolution measurements of infrared radiance to space (Smith et al. 1979, 1983). Since 1985, the HIS has flown successfully in nearly 100 measurement missions of the NASA ER-2, including the FIRE campaigns of 1986 (FIRE I) and 1991 (FIRE II). The data from the aircraft HIS instrument are used to analyze the radiative transfer properties of the clear and clouded atmosphere and to retrieve profiles of atmospheric temperature and the mixing ratio of gases, which are optically active in the 3.5–17 μm region of the infrared spectrum. A few references to the application of these data are Smith et al. (1988a,b, 1989, 1990), Revercomb et al. (1989, 1990), and Clough et al. (1989). For the FIRE experiments, the focus of research with ER-2 HIS measurements has been on the determination of the optical properties and altitude specification of cirrus clouds (Smith et al. 1988b, 1993; Ackerman et al. 1990, 1993; Smith and Frey 1990, 1991).

Detailed descriptions of the ER-2 HIS instruments are contained in publications by Revercomb et al. (1988) and Smith et al. (1990) and will be briefly summarized here. Table 1 defines the measurement characteristics of the instrument. As shown in the optical diagram, Fig. 2, the HIS employs three detectors: two blackbody calibration references and a scan mirror for viewing the earth scene or the calibration reference sources. The system uses the Bomem, Inc. laser servo-controlled dynamic Michelson mirror alignment system, which is crucial for the proper operation of the instrument in a vibration-prone aircraft environment. The optical bench is shock mounted to dampen high-frequency vibration, and the interferometer is evacuated to protect the beamsplitter from condensation during descent of the aircraft. The HIS views the earth directly downward from inside a pod

Corresponding author address: Dr. William L. Smith, CIMSS, Space Science and Engineering Center, University of Wisconsin-Madison, 1225 W. Dayton St., Madison, WI 53706.

© 1995 American Meteorological Society

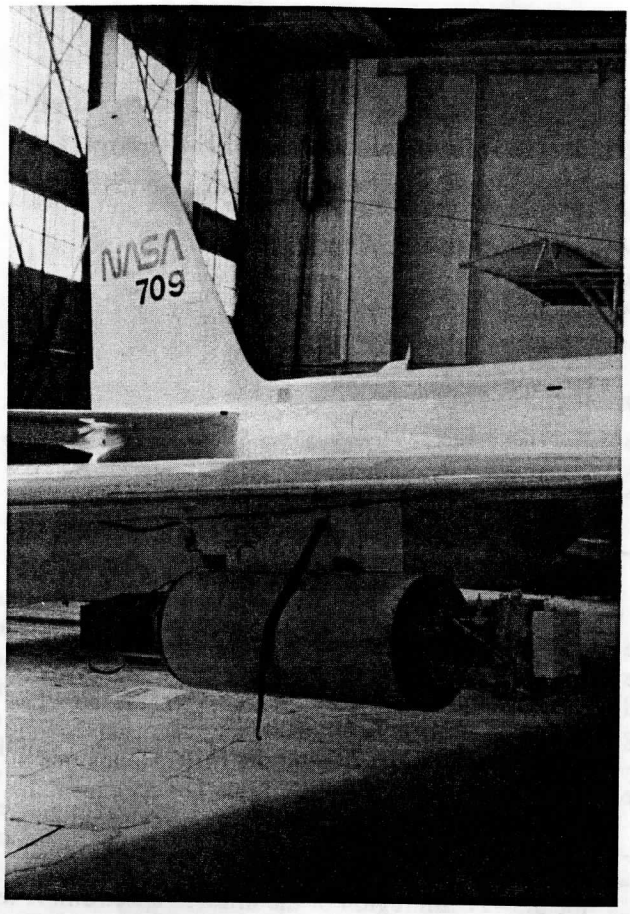

FIG. 1. The HIS instrument mounted in a wing pod used for early U-2 flights. The nose and rear sections of the pod, not shown here, are attached prior to flight. For FIRE the pod is mounted along the centerline of the fuselage of the ER-2, directly beneath the aircraft engine.

(about 3 m long and 0.5 m in diameter) mounted under the centerline of the fuselage. Calibration is accomplished by viewing two blackbodies servo controlled to 300 and 240 K. Normally the instrument is operated in a sequence of 20 interferogram (i.e., spectral) scans; 12 scans of the earth followed by 4 scans of each of the two blackbody reference sources. The instantaneous spatial resolution of the interferometer at the ER-2 altitude of 20 km is 2 km. Each earth spectrum is derived from a double-sided interferogram scan, each direction of which takes about 6 seconds, corresponding to a ground track smear of about 1 km. The data is stored aboard the aircraft on magnetic tape using a dual 3M recording system, each recorder capable of storing 67 megabytes of HIS data, providing 9 hours of continuous recording time.

Radiometric calibration and accuracy of the HIS measurements has been described by Revercomb et al. (1988). Simply stated, the absolute accuracy and noise equivalent temperature (NEΔT) of the spectral measurements are about 0.5 and 0.25 K, respectively, over most of the spectrum, the primary exception being the spectral band edges where the NEΔT is considerably higher. Figure 3 shows typical radiance noise associated with a double-sided (i.e., 12 s) interferogram during the FIRE II experiment as defined from the standard deviation of the noise on calibrated radiance measurements on 5 December 1991. The random measurement error can be reduced by co-adding consecutive spectra, and this is usually performed over the 12 earth scans of the nominal 20 scan sequence.

3. The ground-based HIS

The ground-based HIS, called the Atmospheric Emission Radiance Interferometer (AERI), was operated during FIRE II as part of the Department of Energy Spectral Radiance Experiment (SPECTRE) conducted in Coffeyville, Kansas, in conjunction with the FIRE. The objective of the AERI is to obtain very accurate measurements of the downwelling spectrum of infrared radiance from the atmosphere, which can be analyzed in terms of cloud optical properties and the radiative properties of the molecular atmosphere, the temperature profile of the planetary boundary layer, and the optically active gas distribution of the atmosphere (Smith et al. 1988b; Revercomb et al. 1993). The AERI, like the aircraft HIS, is a Fourier Transform Spectrometer composed of a switchable scan mirror and external cavity blackbodies. Table 1 defines the characteristics of the AERI. Figure 4 shows the configuration with the electro–optical module located on the top of the electronics cabinet. The AERI system also employs a commercially available interferometer from Bomem, Inc. (Michelson Series MB100) with corner cube Michelson mirrors mounted on a common rocking arm supported by flex pivots. The interferometer data is digitized, transferred to an IBM personal computer where it is Fourier transformed and stored for access for data analysis.

A pair of detectors (i.e., one HqCdTe and one InSb detector) in a ''sandwich'' configuration are used to give the broad 3.3–19 μm spectral coverage. The detectors are cooled in a dewar of LN_2. The AERI radiometric calibration subsystem consists of two high emissivity reference blackbodies: one hotter than ambient by 30°–40°C and one at ambient temperature. Another blackbody, a tub of LN_2, is used periodically to check the linearity of the two-point calibration. It was found that there was a slight nonlinearity in the calibration of the longwave HqCdTe, which could be characterized using three-point calibration data. The nonlinearity correction is then used routinely with the two-point blackbody calibration to achieve accurate radiances from sky view data. The system is operated in a 10 minute cycle, during which each of the two blackbodies is viewed for 2 minutes and the sky is viewed for $3\frac{1}{2}$ minutes. Spectra are coadded during each view.

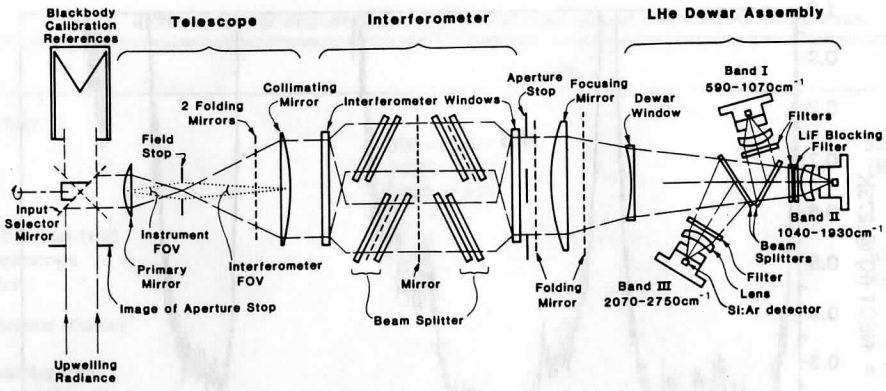

FIG. 2. HIS optical configuration. The primary, collimating, and focusing mirrors are shown as lenses to simplify the illustration.

Figure 5 shows the noise, NEΔT, of the sky spectra achieved on 5 December 1994. As can be seen, the noise level for the 10-minute sequence of data (i.e., about $31/2$ min of sky view) is close to 0.1 K over most of the spectral range of the AERI with the principal exceptions being at the largest wavenumbers and in the regions where strong atmospheric absorption restricts the responsivity. Strong absorption occurs from 1500–1800 cm^{-1} due to water vapor and from 2300–2400 cm^{-1} due to the carbon dioxide in the calibration path inside the instrument. Additional noise reduction can be accomplished by averaging the sky spectra over multiples of the 10-minute-interval records.

4. Inventory of the FIRE II data

The data available from the aircraft HIS and the AERI instruments during FIRE II are summarized in Table 2.

It can be seen that a variety of atmospheric conditions were observed. Simultaneous ER-2 HIS spectra and ground-based AERI spectra were obtained over

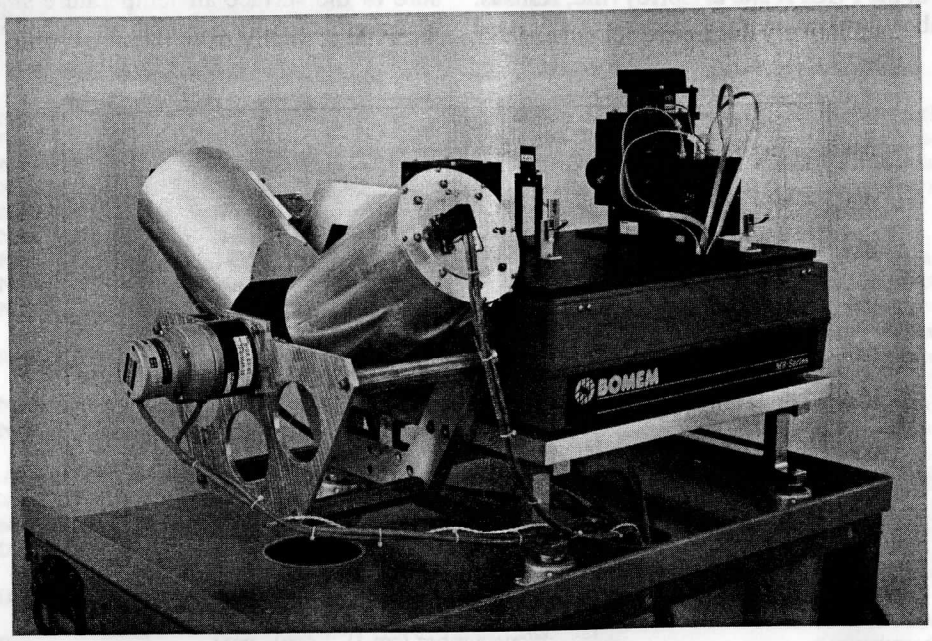

FIG. 3. The ground-based HIS, called the Atmospheric Emitted Radiance Interferometer (AERI), on top of its mobile cart. The two high emissivity blackbodies and hole for viewing a tub of liquid nitrogen placed under the cart's lid is clearly visible.

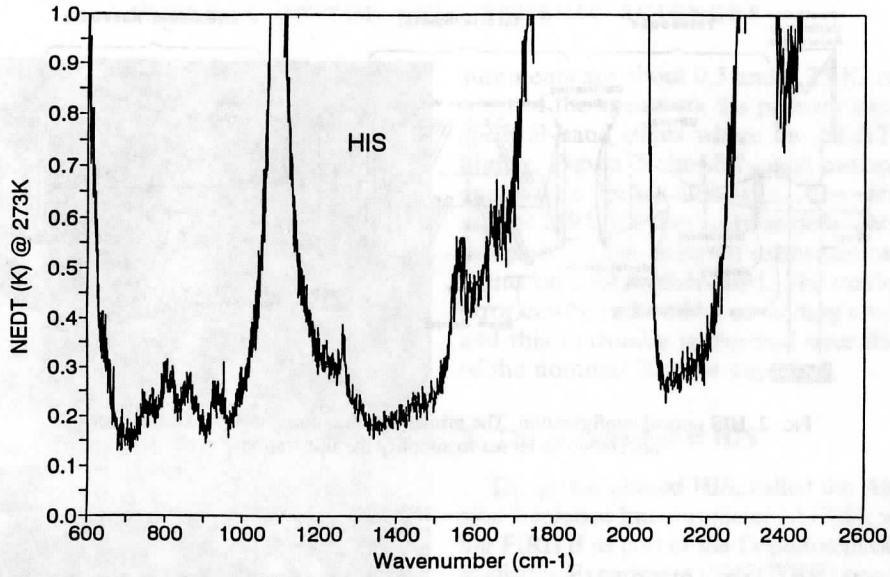

FIG. 4. Noise equivalent temperature difference associated with a double-sided 12-second interferogram taken by the aircraft HIS instrument for a scene temperature of 0°C.

Coffeyville on three separate occasions: 22 November, 26 November, and 5 December.

5. Example radiance observations obtained during Fire II

Figures 6 and 7 show example spectra of radiant brightness temperature observed simultaneously by the aircraft- and ground-based HIS instruments on 22 and 26 November at the FIRE II site at Coffeyville, Kansas. On 22 November, a relatively thick cirrus cloud existed at the time of the measurements with its top at 292 mb with a temperature of 220 K and its base at 640 mb with a temperature of 265 K. On 26 November, the sky appeared to be clear although lidar observations indicated a very thin cirrus layer at 10 Km, at the time of the HIS observations. It is useful to point out a number of atmospheric, cloud, and surface-induced features seen in these spectra. For example, the opaque region of the AERI spectra, 640–700 cm^{-1}, provides a measure of the surface air temperature since the radiance observed is totally from the air surrounding the instru-

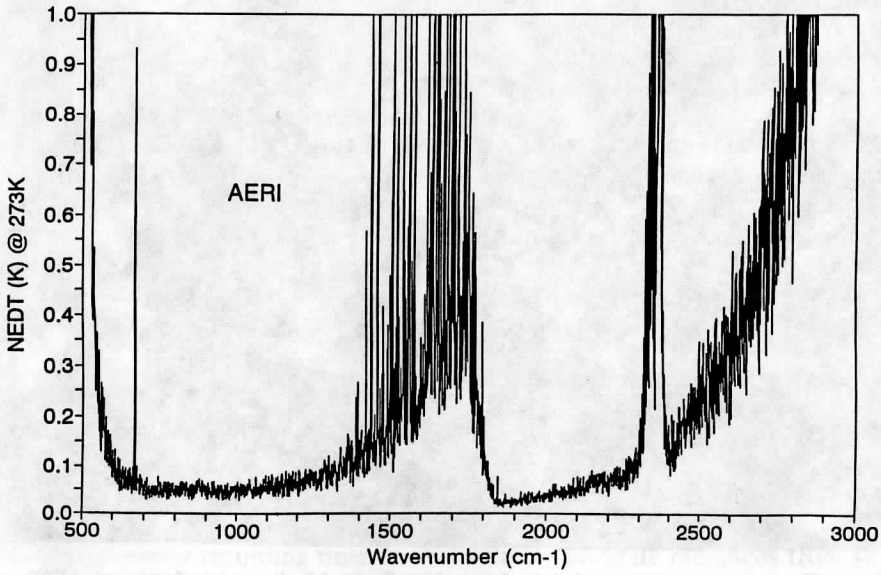

FIG. 5. Noise equivalent temperature difference (NEΔT) associated with a 3-minute interferogram (normal sky view) taken by the ground-based AERI instrument for a scene temperature of 0°C.

TABLE 1. Characteristics of the HIS aircraft- and ground-based AERI instruments.

	HIS	AERI
Spectral range (cm^{-1})		
Band I	590–1080	520–1850
Band II	1080–1850	1850–3020
Band III	2000–2700	
Field of view diameter (mr)		
Instrument/telescope	100	30
Interferometer	30	30
Blackbody reference sources		
Emissivity	>0.998	>0.993
Aperture diameter (cm)	1.5	6.9
Temperature stability (K)	±0.1	< ±0.1
Interferometer	Modified Bomem BBDA Auto aligned	Bomem MB100 Corner cube
Beam splitter		
Substrate	KCl	KBr
Coatings ($^1/_4$ at 3.3 mm)	Ge + Sb_2S_3	Ge + Sb_2S_3
Maximum delay (double sided) current configuration (cm)		
Band I (hardware limit is ±2.0)	±1.8	±1.0
Bands II and III (limited by data system)	±1.2, −0.8	±1.0
Michelson mirror optical scan rate (cm/s)		
Band I (hardware limit ±2.0)	±1.8	±1.0
Band II and III (limited by data system)	±1.2, −0.8	±1.0
Detectors		
Type	Ar doped Si	PC MCT/InSb Sandwich
Diameter (cm)	0.16	0.1
Temperature (K)	6	77

TABLE 2. Summary of HIS and AERI data achieved during FIRE II.

Date (1991)	HIS period (UTC)	AERI periods (UTC)	Coffeyville clouds (ER-2 target)
11 Nov	None	1730	Stratus
12 Nov	None	2326–0229	Cirrus
13 Nov	None	0253–0428	Cirrus/clear
		1818–2400	Cirrus
14 Nov	1401–1800	0000–0341	Thin cirrus (Kansas)
17 Nov	None	1758–2112	Mixed cirrus to clear
18 Nov	2056–2330	0129–2400	Clear (Kansas)[a]
19 Nov	None	0000–0557	Clear/cirrus/stratus
20 Nov	None	1720–2330	Clear
21 Nov	None	0012–2400	Clear
22 Nov	1830–2030	0000–1907	Cirrus (Kansas)[a]
23 Nov	None	1628–2400	Clear/mixed/ovc
24 Nov	1700–2110	0000–2329	Stratus/clear (Gulf of Mexico cirrus)
25 Nov	1600–2000	0037–0548	Altostratus/cumulus/cirrus
		1619–2400	(Oklahoma cirrus)
26 Nov	1500–1750	0029–2400	Clear/cirrus (Kansas)[a]
27 Nov	None	0000–0200	Cirrus
		1401–1721	Stratus
28 Nov	None	1440–2235	Cirrus/stratus
29 Nov	None	1500–2400	Stratus/clear
30 Nov	None	0000–1734	Clear/stratus
3 Dec	1530–1800	0025–2308	Stratus/clear (Gulf of Mexico cirrus)
4 Dec	1830–2030	0000–0641	Clear
		1716–2436	(Gulf of Mexico)
5 Dec	1500–1900	0123–2400	Clear/cirrus (Kansas)[a]
6 Dec	None	0000–0531	Thin cirrus
		1452–2033	Mixed cirrus/altocumulus
7 Dec	None	0054–0552	Clear/stratus
		1449–2123	Stratus/cumulus

[a] Simultaneous HIS/AERI.

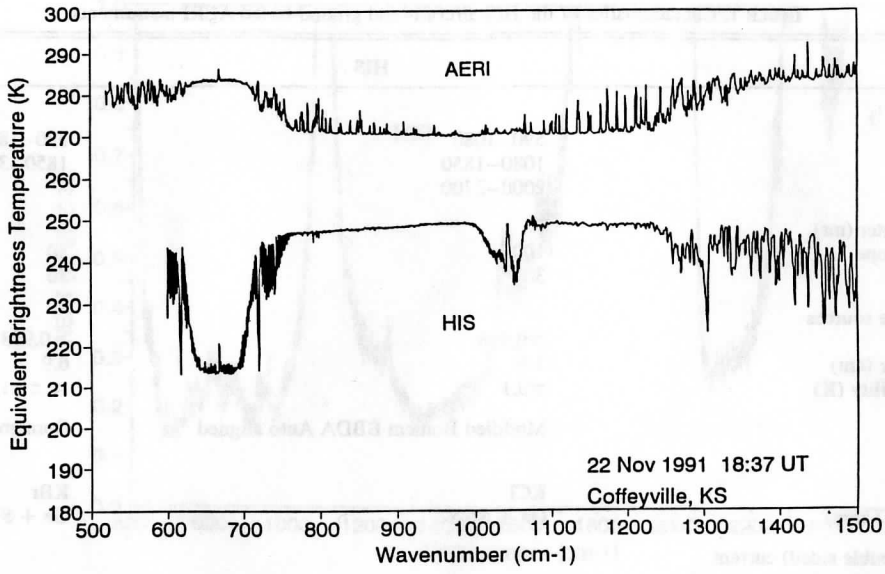

FIG. 6a. Simultaneous brightness temperature spectra observed by the ground-based AERI (up looking) and the aircraft HIS (down looking) in the 500–1500 cm^{-1} region during FIRE II on 22 November 1991.

ment. It can be seen by comparing the brightness temperatures observed that 22 November was slightly warmer than 26 November (283.5 K compared to 282.0 K). Notice that the transparent portion of the "window" region of the aircraft HIS spectrum for 26 November (i.e., 800–1200 cm^{-1}) is also 282 K, indicating that the ground temperature is very close to the surface air temperature at the time of the HIS measurements on that day. Similarly, the opaque region of the aircraft HIS spectra (640–700 cm^{-1}) provides a measure of the air temperature at the aircraft altitude, which was 214 K on 22 November and 212 K on 26 November.

With regard to the cloud observed on 22 November, radiosonde observations near the time of the HIS measurements indicate that the cloud base is about 640 mb with a temperature of 265 K. This is slightly lower than the brightness temperature observed by the AERI in the window region (270 K) indicating that the base of the cloud is relatively opaque, the discrepancy between the brightness temperature and the cloud-base temperature

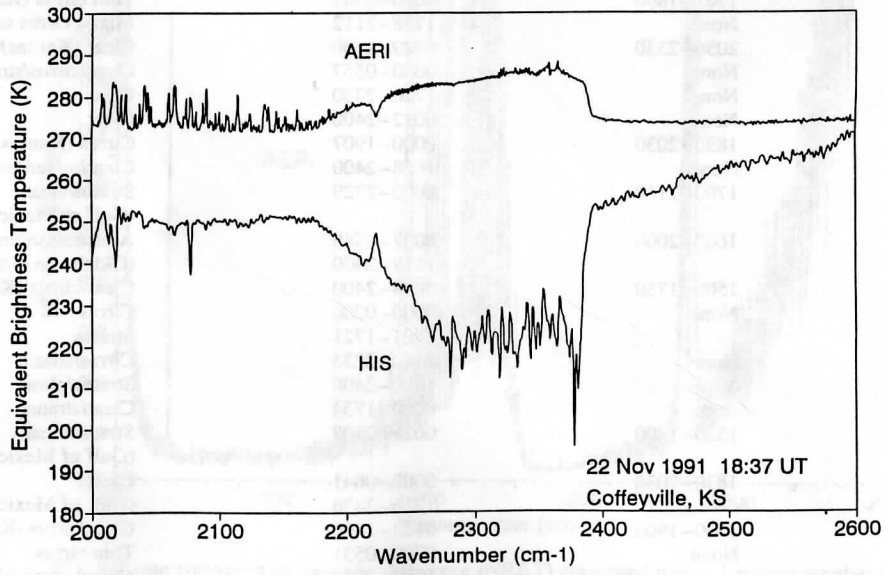

FIG. 6b. As in Fig. 6a except for the 2000–2600 cm^{-1} region.

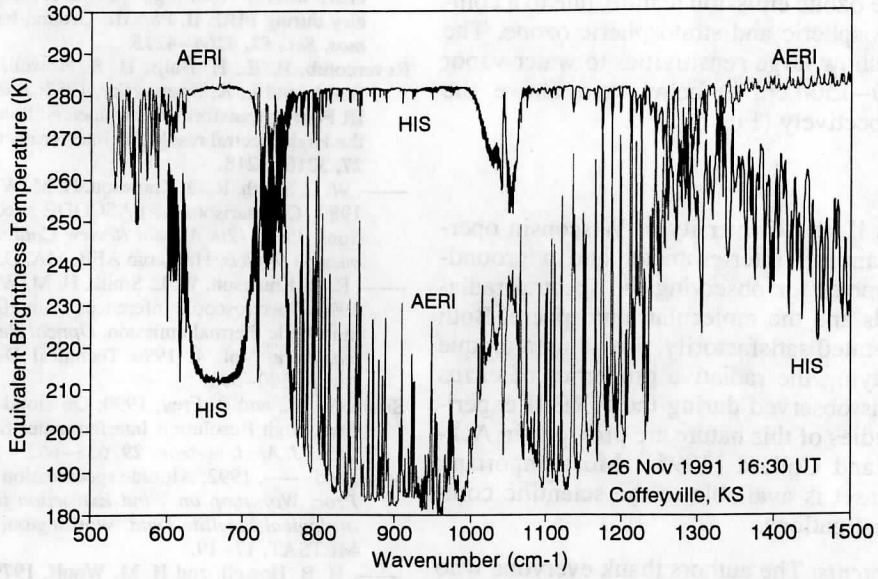

FIG. 7. a. As in Fig. 6a except for 26 November 1991.

being due to the emission by water vapor below the cloud. The cloud top, on the other hand, was observed by the radiosonde to be at 292 mb with a temperature of 227 K. The window brightness temperature observed by the downward looking aircraft HIS instrument is about 249 K (i.e., the temperature at a pressure altitude of 450 mb), indicating that the top most layers of this thick cirrus cloud are semitransparent (i.e., radiation from deep within the cloud is penetrating upward to the ER-2 altitude of 20 km). Another indication of the "nonblackness" of the cloud top is given by the slope of the brightness temperature within the 800–1100 cm^{-1} window region of the HIS spectrum. If the cloud were completely opaque, the brightness temperature of the cloud would be constant with respect to wavenumber.

Finally, it is interesting to note that for the cloudy case, 22 November, the AERI spectrum does not show an ozone emission feature at 1050 cm^{-1}, indicating a relatively low level of tropospheric ozone below the cloud level of 640 mb. This is quite different than the clear case on 26 November where the AERI spectrum

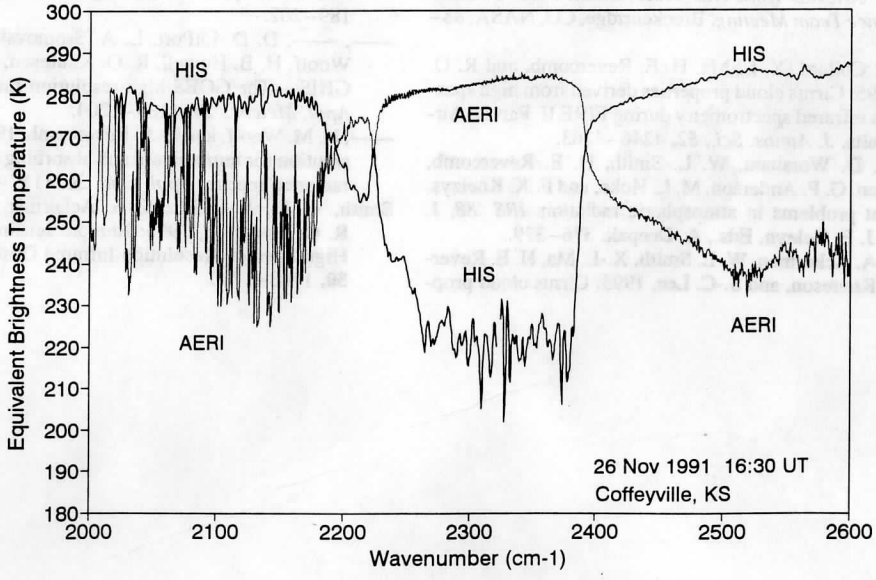

FIG. 7. b. As in Fig. 6b except for 26 November 1991.

possesses a large ozone emission feature, due to a combination of tropospheric and stratospheric ozone. The AERI and HIS show large sensitivities to water vapor emission (1300–1500 cm^{-1}) below and above the cloud level, respectively (Fig. 6).

6. Summary

During FIRE II, the University of Wisconsin operated an ER-2 aircraft interferometer and a ground-based interferometer for observing the spectral radiation from clouds and the molecular atmosphere. Both instruments operated satisfactorily, providing a unique dataset for studying the radiative properties of cirrus and other clouds observed during the FIRE II experiment. Initial studies of this nature are provided in Ackerman (1995) and Collard (1995). Most important, this unique dataset is available to the scientific community for investigations.

Acknowledgments. The authors thank everyone who assisted in the implementation of the HIS and AERI instruments for the FIRE II/SPECTRE experiment. In particular, Bob Herbsleb, Tim Dirks, and John Short were extremely helpful in the preparation and maintenance of the instrumentation at both Houston, Texas, where the ER-2 aircraft was based, and Coffeyville, Kansas, where the AERI was based. The research associated with the FIRE II/SPECTRE experiment was supported by NASA Grant NAG1-1177 and DOE Grant DE-FG-02-92ER61365.

REFERENCES

Ackerman, S. A., W. L. Smith, J. D. Spinherne, and H. E. Revercomb, 1990: The 27–28 October 1986 FIRE IFO Cirrus case study: Spectral properties of cirrus clouds in the 8–12 μm window. *Mon. Wea. Rev.*, **118,** 2377–2388.

——, ——, X.-L. Ma, R. O. Knuteson, and H. E. Revercomb, 1993: Cirrus cloud retrievals from HIS observations. *Proc. FIRE II CIRRUS Science Team Meeting,* Breckenridge, CO, NASA, 88–92.

——, ——, A. D. Collard, X.-L. Ma, H. E. Revercomb, and R. O. Knuteson, 1995: Cirrus cloud properties derived from high spectral resolution infrared spectrometry during FIRE II. Part II: Aircraft HIS results. *J. Atmos. Sci.,* **52,** 4246–4263.

Clough, S. A., R. D. Worsham, W. L. Smith, H. E. Revercomb, R. O. Knuteson, G. P. Anderson, M. L. Hoke, and F. X. Kneizys, 1989: Current problems in atmospheric radiation. *IRS '88,* J. Lenoble and J. F. Geleyn, Eds., A. Deepak, 376–379.

Collard, A. D., S. A. Ackerman, W. L. Smith, X.-L. Ma, H. E. Revercomb, R. O. Knuteson, and S.-C. Lee, 1995: Cirrus cloud properties derived from high spectral resolution infrared spectrometry during FIRE II. Part III: Ground-based HIS results. *J. Atmos. Sci.,* **52,** 4264–4275.

Revercomb, H. E., H. Buijs, H. B. Howell, D. D. LaPorte, W. L. Smith, and L. A. Sromovsky, 1988: Radiometric calibration of IR Fourier transform spectrometers: Solution to a problem with the High spectral resolution Interferometer Sounder. *Appl. Opt.,* **27,** 3210–3218.

——, W. L. Smith, R. O. Knuteson, H. M. Woolf, and H. B. Howell, 1989: Comparisons of FASCODE spectra with HIS observations. *Proc. 12th Annual Review Conf. on Atmospheric Transmission Models,* Hanscom AFB, MA, U.S. Air Force, 537–573.

——, R. O. Knuteson, W. L. Smith, H. M. Woolf, and H. B. Howell, 1990: Spectroscopic inferences from HIS measurements of atmospheric thermal emission. *Optical Remote Sensing of the Atmosphere,* Vol. 4, 1990 Technical Digest Series, Opt. Soc. Amer., 590–593.

Smith, W. L., and R. Frey, 1990: On cloud altitude determinations from High Resolution Interferometer Sounder (HIS) observations. *J. Appl. Meteor.,* **29,** 658–662.

——, and ——, 1992: Altitude specification of cloud motion winds. *Proc. Workshop on Wind Extraction from Operational Meteorological Satellite Data,* Washington, D.C., NOAA and EUMETSAT, 17–19.

——, H. B. Howell, and H. M. Woolf, 1979: The use of interferometric radiance measurements for sounding the atmosphere. *J. Atmos. Sci.,* **36,** 566–575.

——, H. E. Revercomb, H. B. Howell, and H. M. Woolf, 1983: HIS—A satellite instrument to observe temperature and moisture profiles with high vertical resolution. *Proc. Fifth Conf. on Atmospheric Radiation,* Baltimore, MD, Amer. Meteor. Soc., 1–9.

——, ——, ——, ——, and D. D. LaPorte, 1986: The High Resolution Interferometer Sounder (HIS). *CIMSS View,* Vol. 2, No. 3, Cooperative Institute for Meteorological Satellite Studies, University of Wisconsin—Madison, 1–5 pp.

——, ——, ——, and X.-L. Ma, 1988a: Multi-spectral window radiance observations of cirrus from satellite and aircraft—November 2, 1986. *Proc. Project FIRE: FIRE Science Experiment Team Meeting,* Vail, CO, NASA, 91–95.

——, H. M. Woolf, H. B. Howell, H.-L. Huang, and H. E. Revercomb, 1988b: The simultaneous retrieval of atmospheric temperature and water vapor profiles—Application to measurements with the High spectral resolution Interferometer Sounder (HIS). *RSRM 87: Advances in Remote Sensing Retrieval Methods,* A. Deepak, H. Fleming, and J. Theon, Eds., A. Deepak, 189–202.

——, ——, D. D. LaPort, L. A. Sromovsky, S. Silverman, H. M. Woolf, H. B. Howell, R. O. Knuteson, and H.-L. Huang, 1990: GHIS—The GOES high-resolution Interferometer Sounder. *J. Appl. Meteor.,* **29,** 1189–1204.

——, H. M. Woolf, and H. E. Revercomb, 1991: Linear simultaneous solution for temperature and absorbing constituent profiles from radiance spectra. *Appl. Opt.,* **30,** 1117–1123.

Smith, W. L., X.-L. Ma, S. A. Ackerman, H. E. Revercomb, and R. O. Knuteson, 1993: Remote sensing cloud properties from High Spectral Resolution Infrared Observations. *J. Atmos. Sci.,* **50,** 1708–1720.

8909181096O

b89091810960a